

AUS Repository

Near-Field FMCW Radar for Mapping of Multilayer Structures

Item Type	Thesis
Authors	Jundi, Ayman Jalal
Download date	2026-04-16 12:18:22
Link to Item	http://hdl.handle.net/11073/142

NEAR-FIELD FMCW RADAR FOR MAPPING OF MULTILAYER
STRUCTURES

A THESIS IN ELECTRICAL ENGINEERING
Master of Science in Electrical Engineering

Presented to the faculty of the American University of Sharjah
College of Engineering
in partial fulfillment of
the requirements for the degree

MASTER OF SCIENCE

by
AYMAN JALAL JUNDI
B.S. 2008

Sharjah, UAE
May 2010

©2010

AYMAN JALAL JUNDI

ALL RIGHTS RESERVED

NEAR-FIELD FMCW RADAR FOR MAPPING OF MULTILAYER STRUCTURES

Ayman Jalal Jundi, Candidate for the Master of Science Degree

American University of Sharjah, 2010

ABSTRACT

Near-field microwave non-destructive evaluation and inspection (NDE&I) of structures and materials is widely used in many applications. Single frequency measurements were found to be effective in detecting defects and abrupt changes, such as cracks and air voids, within homogenous structures. However, in some complex structures with many variables, multiple-frequency measurements were implemented to solve problems associated with more unknown parameters. These problems involved layered structures with more diversity in terms of number of factors that define the structure, namely, the layers thicknesses and relative permittivities (ϵ_r). Later on, more systematic broadband techniques, such as Frequency Modulated Continuous Wave (FMCW) proved to be effective in measuring thicknesses of layers in a multilayered structure. However, obtaining permittivity information was still a big challenge.

Generally, from microwave's point of view, the interaction of the radiation from open-ended rectangular waveguides (RWGs) with any object can be modeled as radiations passing through multiple flat layers –The validity of the model is

conditioned on the severity of planar variations of the modeled layers relative to the wavelength. If such a model is developed, it might enable us to measure the dielectric properties and thicknesses of the existing layers. A long term speculation of such application could be a microwave device that is capable of taking cross sectional images of the human body as a cheaper and more accurate replacement for the Magnetic Resonance Imaging (MRI) machine.

In this thesis a novel technique on modeling the forward problem of near-field FMCW is presented. The technique is based on modeling the near-field frequency response of a multilayered structure illuminated by an open-ended RWG. The main objective of this research is to predict the return of an applied FMCW signal from a multilayered structure within the near-field of an open-ended RWG. The modeled forward problem opens new doors to develop a new microwave NDE&I approach for inspecting the integrity of layered structures with potentially high resolution.

CONTENTS

ABSTRACT	iii
LIST OF ILLUSTRATIONS.....	vii
LIST OF TABLES.....	x
ACKNOWLEDGEMENTS	xi
1. INTRODUCTION.....	1
1.1 NEAR-FIELD FMCW	1
1.2 MOTIVATION AND PROBLEM STATEMENT.....	2
1.3 METHODOLOGY	3
1.4 THESIS CONTRIBUTION AND OUTLINE	4
2. BACKGROUND AND LITERATURE REVIEW.....	6
2.1 FMCW RADARS	6
2.1.1 FMCW Under Ideal Operating Conditions.....	7
2.1.2 FMCW Under Practical Operating Conditions	9
2.2 MICROWAVES	10
2.2.1 Microwave Frequency Bands	11
2.2.2 Dielectric Media	12
2.3 WAVEGUIDE WAVE PROPAGATION	12
2.3.1 Modes Propagation Conditions.....	15
2.4 NEAR-FIELD WAVEGUIDE-BASED IMAGERS	16
2.4.1 Types of Captured Images.....	17
2.5 NEAR-FIELD SINGLE FREQUENCY MATHEMATICAL MODELLING	19
2.5.1 General N-Layer Composite Terminated with IHS	24
2.6 MULTIMODE SOLUTIONS	25
3. MATHEMATICAL DERIVATIONS	26
3.1 THE REFLECTION COEFFICIENT'S DERIVATIONS.....	26
3.1.1 The Spatial Distribution of the Reflection Coefficient $\Gamma(x, y)$	29
3.1.2 The Effective Value of the Reflection Coefficient Γ	30
3.2 MULTIMODE GENERAL SOLUTION.....	32
4. RESULTS ANALYSIS AND SIMULATION	40
4.1 THE REFLECTION COEFFICIENT'S Γ COMPUTATIONS	40
4.1.1 The Spatial Distribution of Γ	40
4.1.2 The Effective Value of the Reflection Coefficient Γ	49
4.2 FREQUENCY RESPONSE OF A MULTILAYERED STRUCTURE	62
4.2.1 LTI System Analogy.....	62

4.2.2	<i>Frequency Response</i>	63
4.2.3	<i>Impulse Response</i>	67
4.3	FMCW RADAR SIMULATION	68
4.4	EVALUATION TIME.....	75
5.	CONCLUSIONS AND FUTURE WORK	77
5.1	CONCLUSIONS	77
5.2	RECOMMENDATIONS FOR FUTURE WORK.....	79
	REFERENCE LIST	81
	Appendix A	83
	Matlab Codes.....	83
	VITA	89

LIST OF ILLUSTRATIONS

FIGURE 2.1: TRIANGULAR FMCW TIME-FREQUENCY RELATIONSHIP.....	7
FIGURE 2.2: TRIANGULAR FMCW TIME DOMAIN REPRESENTATION.....	7
FIGURE 2.3: FMCW RADAR SWEEP.....	8
FIGURE 2.4: FMCW BEAT FREQUENCY.....	8
FIGURE 2.5: THE ELECTROMAGNETIC SPECTRUM SHOWING THE LOCATION OF THE MICROWAVE SPECTRUM.....	10
FIGURE 2.6. AN ILLUSTRATION OF THE RELATIONSHIP BETWEEN ATTENUATION CONSTANT α AND PROPAGATION CONSTANT β AS A FUNCTION OF FREQUENCY FOR TE_{10} MODE IN AN X-BAND WAVEGUIDE.....	16
FIGURE 2.7: PHASE IMAGER SCATTEROMETER DIAGRAM, THE WAVEGUIDE IS SCANNED IN THE xy -PLANE.....	18
FIGURE 2.8: MAGNITUDE IMAGER SCATTEROMETER CIRCUIT DIAGRAM, THE WAVEGUIDE SCANS IN THE xy -PLANE.....	19
FIGURE 2.9: PROBLEM SETUP VIEWED IN THE yz -PLANE.....	20
FIGURE 4.1. RECTANGULAR WAVEGUIDE'S APERTURE SYMMETRY AROUND THE MIDPOINT.....	41
FIGURE 4.2. THE MAGNITUDE OF THE REFLECTION COEFFICIENT OVER THE APERTURE FOR IHS OF FREE SPACE $\epsilon_r = 1$	41
FIGURE 4.3. THE MAGNITUDE OF THE REFLECTION COEFFICIENT OVER THE APERTURE FOR IHS OF $\epsilon_r = 3$	42
FIGURE 4.4. THE MAGNITUDE OF THE REFLECTION COEFFICIENT OVER THE APERTURE FOR IHS OF A) $\epsilon_r = 10$ B) $\epsilon_r \approx$ ∞	42
FIGURE 4.5. THE RIPPLING EFFECT IN BOTH DIMENSIONS ALONG x AND ALONG y	43
FIGURE 4.6. THE DISTRIBUTION OF THE ELECTRIC FIELD OVER THE APERTURE.....	43
FIGURE 4.7. ONE DIMENSIONAL DISCRETE RECTANGULAR SIGNAL.....	44
FIGURE 4.8. THE DFT OF THE DISCRETE RECTANGULAR SIGNAL (SHIFTED SPECTRUM USING FFTSHIFT).....	44
FIGURE 4.9. RECONSTRUCTED RECTANGULAR SIGNAL WITH THE TRUNCATED SPECTRUM.....	45
FIGURE 4.10. THE FLAT RESPONSE OF THE REFLECTION COEFFICIENT OVER THE APERTURE.....	47
FIGURE 4.11. THE MAGNITUDE OF THE REFLECTION COEFFICIENT OVER THE APERTURE FOR IHS USING THE IMPROVED ALGORITHM OF A) $\epsilon_r = 3$ B) $\epsilon_r = 10$	47
FIGURE 4.12. THE MAGNITUDE OF THE REFLECTION COEFFICIENT OVER THE APERTURE FOR IHS USING THE IMPROVED ALGORITHM OF A) $\epsilon_r = 3$ B) $\epsilon_r = 5$	48
FIGURE 4.13. THE MAGNITUDE OF THE REFLECTION COEFFICIENT OVER THE APERTURE FOR IHS USING THE IMPROVED ALGORITHM OF A) $\epsilon_r = 7$ B) $\epsilon_r = 10$	48
FIGURE 4.14 THE MAGNITUDE OF THE REFLECTION COEFFICIENT OVER THE APERTURE FOR IHS USING THE IMPROVED ALGORITHM OF A) $\epsilon_r = 15$ B) $\epsilon_r = 30$	49
FIGURE 4.15. REFLECTION COEFFICIENT MAGNITUDE AND PHASE COMPARISON WITH [13] A) THE RESULTS OF [13] B) THE VALUES COMPUTED USING EQUATION (3.12).....	50
FIGURE 4.16. THE OVERLAID RESULT COMPARISON OF THIS THESIS IN BLUE CIRCLES WITH [13] IN BLACK SOLID AND DASHED LINES.....	51
FIGURE 4.17. WAVEGUIDE NORMALIZED ADMITTANCE COMPARISON BETWEEN [13] AND [15].....	52
FIGURE 4.18. OVERLAID WAVEGUIDE NORMALIZED ADMITTANCE COMPARISON BETWEEN THE RESULTS OF THIS THESIS AND THE RESULTS OBTAINED BY [13]AND [15] I.E. WRITTEN AS [18] ON THE GRAPH.....	52
FIGURE 4.19. MAGNITUDE OF Γ AS PRESENTED IN [13] AS A FUNCTION OF PERMITTIVITY USING 6 MODES.....	53
FIGURE 4.20. MAGNITUDE OF Γ USING EQUATION (3.12) IN COLOR OVERLAID OVER THE RESULTS FOUND IN [13] USING 6 MODES ONLY.....	53
FIGURE 4.21. THE ABSOLUTE DIFFERENCE IN THE COMPLEX VALUE OF Γ FOR THREE DIFFERENT FREQUENCIES AS A FUNCTION OF THE RELATIVE PERMITTIVITY ϵ_r	54

FIGURE 4.22. THE DIFFERENCE IN THE MAGNITUDE OF Γ FOR THREE DIFFERENT FREQUENCIES AS A FUNCTION OF THE RELATIVE PERMITTIVITY ϵ_r	55
FIGURE 4.23. THE DIFFERENCE IN THE PHASE OF Γ FOR THREE DIFFERENT FREQUENCIES AS A FUNCTION OF THE RELATIVE PERMITTIVITY ϵ_r	55
FIGURE 4.24. MAGNITUDE OF THE DIFFERENCE BETWEEN EQUATIONS (3.12) AND (3.14) AS A FUNCTION OF THICKNESS OF FIRST LAYER AND FREQUENCY FOR $\epsilon_r = 4$	56
FIGURE 4.25. THE DIFFERENCE IN MAGNITUDE BETWEEN THE EQUATIONS (3.12) AND (3.14) AS A FUNCTION OF THICKNESS OF FIRST LAYER AND FREQUENCY FOR $\epsilon_r = 4$	56
FIGURE 4.26. MAGNITUDE OF THE DIFFERENCE BETWEEN EQUATIONS (3.12) AND (3.14) AS A FUNCTION OF THICKNESS OF FIRST LAYER AND FREQUENCY FOR $\epsilon_r = 13$	57
FIGURE 4.27. THE DIFFERENCE IN MAGNITUDE BETWEEN THE EQUATIONS (3.12) AND (3.14) AS A FUNCTION OF THICKNESS OF FIRST LAYER AND FREQUENCY FOR $\epsilon_r = 13$	57
FIGURE 4.28. THE DISTRIBUTION OF Γ OVER THE APERTURE FOR A SINGLE LAYER WITH $\epsilon_r = 12$ AND 1.5CM THICKNESS.	58
FIGURE 4.29. Γ AS COMPUTED BY EQUATION (3.12) AS A FUNCTION OF VARYING THICKNESS OF FIRST LAYER $\epsilon_r = 4$	59
FIGURE 4.30 Γ AS COMPUTED BY EQUATION (3.14) AS A FUNCTION OF VARYING THICKNESS OF FIRST LAYER $\epsilon_r = 4$	59
FIGURE 4.31. THE DIFFERENCE IN MAGNITUDE BETWEEN THE EQUATIONS (3.12) AND (3.14) AS A FUNCTION OF THICKNESS OF FIRST LAYER AND FREQUENCY FOR $\epsilon_r = 4$	60
FIGURE 4.32. THE DIFFERENCE IN MAGNITUDE BETWEEN THE EQUATIONS (3.12) AND (3.14) AS A FUNCTION OF THICKNESS OF FIRST LAYER AND FREQUENCY FOR $\epsilon_r = 8$	60
FIGURE 4.33. THE DIFFERENCE IN MAGNITUDE BETWEEN THE EQUATIONS (3.12) AND (3.14) AS A FUNCTION OF THICKNESS OF FIRST LAYER AND FREQUENCY FOR $\epsilon_r = 13$	60
FIGURE 4.34. Γ AS COMPUTED BY EQUATION (3.12) AS A FUNCTION OF VARYING THICKNESS OF FIRST LAYER OVER THE X-BAND RANGE AND $\epsilon_r = 8$, STARTING FROM 8.2 GHz (BLUE INNER MOST) UP TO 12.4GHz.....	61
FIGURE 4.35. Γ AS COMPUTED BY EQUATION (3.14) AS A FUNCTION OF VARYING THICKNESS OF FIRST LAYER OVER THE X-BAND RANGE AND $\epsilon_r = 8$, STARTING FROM 8.2 GHz (BLUE INNER MOST) UP TO 12.4GHz.....	61
FIGURE 4.36. THE FREQUENCY RESPONSE OF A SIMPLE STRUCTURE CONSISTING OF TWO LAYERS OVER THE X-BAND.	64
FIGURE 4.37. THE CHANGE IN THE FREQUENCY RESPONSE OF THE STRUCTURE AS A FUNCTION OF VARYING THICKNESS OVER THE X-BAND FREQUENCY RANGE.	64
FIGURE 4.38. SCHEMATIC OF THE TRUNCATED SANDWICH COMPOSITE [1].....	65
FIGURE 4.39. THE FREQUENCY RESPONSE OF A COMPLEX STRUCTURE CONSISTING OF SIX LAYERS OVER THE X-BAND.....	66
FIGURE 4.40. THE CHANGE IN THE FREQUENCY RESPONSE OF THE STRUCTURE AS A FUNCTION OF VARYING THICKNESS OVER THE X-BAND FREQUENCY RANGE.	66
FIGURE 4.41. THE CHANGE IN THE PHASE RESPONSE OF THE STRUCTURE AS A FUNCTION OF VARYING THICKNESS OVER THE X-BAND FREQUENCY RANGE (UNWRAPPED PHASE RESPONSE).....	67
FIGURE 4.42. APPROXIMATED IMPULSE RESPONSE USING A BAND LIMITED FREQUENCY RESPONSE OF 300GHz BANDWIDTH.	68
FIGURE 4.43. THE FREQUENCY RESPONSE OF THE STRUCTURE WHEN THE FIRST LAYER THICKNESS IS 0.1CM.	70
FIGURE 4.44. THE FREQUENCY RESPONSE OF THE STRUCTURE WHEN THE FIRST LAYER THICKNESS IS 10CM.	70
FIGURE 4.45. THE FREQUENCY RESPONSE OF THE STRUCTURE AS A FUNCTION OF FIRST LAYER THICKNESS.....	71
FIGURE 4.46. THE MAGNITUDE SPECTRUM OF THE FMCW SIGNAL.....	71
FIGURE 4.47. THE RETURN FMCW SIGNAL OBTAINED USING THE STRUCTURE'S FREQUENCY RESPONSE.....	72
FIGURE 4.48. THE BEAT FREQUENCY SPECTRUM FOR TWO THICKNESSES 0.1CM AND 10CM USING RECTANGULAR WINDOW.	72
FIGURE 4.49. THE BEAT FREQUENCY SPECTRUM FOR TWO THICKNESSES 0.1CM AND 10CM USING HAMMING WINDOW IN LINEAR SCALE.	73

FIGURE 4.50. THE BEAT FREQUENCY SPECTRUM FOR TWO THICKNESSES 0.1CM AND 10CM USING HAMMING WINDOW IN LOG SCALE.	73
FIGURE 4.51. THE CHANGE IN THE BEAT FREQUENCY MAGNITUDE SPECTRUM IN LOG SCALE AS A FUNCTION OF VARYING THICKNESS.	74
FIGURE 4.52. THE CHANGE IN THE BEAT FREQUENCY PHASE SPECTRUM AS A FUNCTION OF VARYING THICKNESS.	74
FIGURE 4.53. COMPUTATION TIME FOR A SINGLE VALUE OF Γ AS A FUNCTION OF NUMBER OF LAYERS.	76
FIGURE 4.54. THE TIME REQUIRED TO EVALUATE A SINGLE VALUE OF Γ AS A FUNCTION OF NUMBER OF LAYERS (N).	76

LIST OF TABLES

TABLE 2.1: MICROWAVES FREQUENCY BANDS.....	11
TABLE 2.2: VARIABLE DEFINITIONS IN MAXWELL'S EQUATIONS (ARROW DENOTES A VECTOR QUANTITY).....	11
TABLE 2.3: TE AND TM MODES' EQUATIONS FOR RECTANGULAR WAVEGUIDES.....	14
TABLE 4.1. FMCW RADAR PARAMETERS.	69
TABLE 4.2. COMPUTATION SPEED AS A FUNCTION OF NUMBER OF LAYERS.	75

ACKNOWLEDGEMENTS

بِسْمِ اللَّهِ الرَّحْمَنِ الرَّحِيمِ

I would like to thank God for all I am and all I have. I would like to offer my sincere appreciation to those who supported me during this endeavor. I am very grateful for the patient guidance and the endless support and encouragement given by my advisor and mentor Dr. Naser Qaddoumi. I would also like to express my gratitude to Dr. K. Assaleh, Dr. M. Hassan, Dr. G. Hussein, Dr. L. Albasha, Dr. A. El-Hag, Dr. M. El-Tarhuni for the knowledge they have given me unconditionally during my master years. I would like to thank in particular Eng. I. Abu Seif and all of my colleagues in the Communications and Signal Processing Lab and Microwave Lab for their help and priceless encouragement during this work. I would also like to express my gratitude to the staff of the Electrical Engineering Department for they are the ones who shaped my understanding with countless hours of work and dedication.

Finally, saving the best for the last, I thank my parents, sisters, grandmothers, and relatives for their acceptance of who I am. My parents, Jalal and my mother, thank you for being loving and caring and showing that by fattening me with delicious meals.

*In loving memory of my Grandfathers. If memories were a lane, I would walk
right up to you, to see you again.*

CHAPTER 1

INTRODUCTION

This chapter will give a brief introduction about the title of this thesis. It starts by explaining near-field in microwave terminology in addition to the meaning of FMCW and its advantages over other types of radar signals. Then, it will provide a rough idea about how can a system based on FMCW be used to scan and map multilayer structures. Finally the objective and contribution of this thesis will be clarified and the general outline of the thesis will be provided.

1.1 Near-Field FMCW

Microwave imaging and non-destructive evaluation and inspection (NDE&I) is a way by which a structure can be interrogated. Microwave imaging is based on transmitting a microwave signal into a structure and using the return signal information i.e. the reflected signal to create a two or three dimensional image of the object or structure under test [1]. This is usually done in either in the near-field or the far-field regions of the antenna or any radiating source. As the naming implies, the near-field and far-field are defined based on distance, operating frequency and antenna or probe type. In typical near-field imaging schemes, probes such as open-ended waveguides and coaxial lines are used, whereas in far-field imaging an antenna with high gain is required for transmitting and receiving the microwave energy so it will not be dispersed into undesired regions. One of the obvious disadvantages of far-field imaging is that it does not offer good spatial resolution. Since the footprint i.e. the area seen by the antenna is relatively large compared to near-field imaging, lenses are sometimes used to focus the antenna and remedy this problem [2]. In the case of near-field imaging, no lenses are required to improve the spatial resolution since the probe is usually in contact or few millimetres away from the structure.

FMCW stands for Frequency Modulated Continuous Wave. It is a type of signals used in high resolution radar systems. The signal itself is usually a linear frequency chirp swept over a certain bandwidth depending on the required resolution and used equipment. FMCW signals are often used to measure time delays between multiple reflections hence measuring ranges of a single or multiple targets. This can also be achieved by using pulsed radars. In pulsed radars the narrower the pulse the less the reflected pulses overlap and the higher the resolution i.e. decomposable pulses each refer to the presence of a target. Unlike pulsed radar signals, FMCW signal can measure time delays between consecutive reflections even when these reflections overlap in time. Instead of focusing high bandwidth signal into very short pulse duration with high peak power, FMCW signal could provide the same resolution with much lower peak power [3]. Theoretically, there is no upper limit on the FMCW signal length in time which means the peak power can be controlled without sacrificing the resolution. FMCW radars are often used to measure thicknesses of layers. Measuring other properties such as the relative permittivity as well as thicknesses is an ongoing research. This thesis can be used as a basis to develop such techniques.

1.2 Motivation and Problem Statement

The properties of newly developed materials added a challenge to the existing NDE&I techniques. Multilayered Dielectric structures such as composite materials of plastics, ceramics, and carbon fibers replaced their metal counterparts in many applications due to their attractive features. Insuring the reliability and integrity of these composites is vital prior to using them in order to avoid possible disastrous failures. Therefore, it deemed necessary to develop techniques that can measure and map the thickness and dielectric profile of these structures. Among the existing NDE&I techniques that were used in the past in detecting defects are: eddy currents, ultrasound, and Radiography using X-ray or Gamma-ray. Each of these techniques suffered from drawbacks. For example, Eddy currents cannot be used in many applications since it is dedicated to testing metallic structures. Further, ultrasound's performance is highly degraded for inhomogeneous materials and requires specific material surface conditions. Radiography using X-ray or Gamma radiation can effectively detect defects in the range of few micrometers. However, it is not the best

choice in many industrial applications due to its high cost, the need to access the material from both sides, the high absorption that limits the distance where these rays can penetrate in addition to safety concerns [4]. Additionally, FMCW was successfully utilized in mapping relatively thick layers of dielectric structures. Researchers reported that microwave NDE&I using open-ended waveguides can be used efficiently to detect defects in composite structures [1][4][5][6][7][8][9]. The testing is done by illuminating the inspected material with electromagnetic waves. Both magnitude and phase of the reflected waves carry information about the properties of the structure. The trend in the past was to utilize open-ended waveguides with single frequency or at least one frequency at a time. An intensive study was performed to explain the interaction of the electromagnetic waves radiated out of a rectangular waveguide onto a stratified dielectric material [5].

In this thesis FMCW signal will be used in the near-field region of a RWG. This signal will illuminate N-layers stratified simple dielectric and non-magnetic structure. The ultimate goal is to successfully identify the layers of the structure and map their thicknesses and relative permittivities. In order to reach that goal we need to establish the forward problem on how an FMCW signal interacts with the multilayered structure. Then the inverse problem tries to obtain the structure's parameters based on the reflected FMCW signal. This thesis concentrates on modeling the forward problem of the interaction of FMCW waves with a multilayered structure. The developed mathematical forward problem model will facilitate solving the inverse problem in the future.

1.3 Methodology

The relationship between the structure layers and the aperture's complex reflection coefficient (Γ) will be derived for all frequencies of operation. The derivations will be tested by simulation and compared to the results from other publications. The varying behavior of the reflection coefficient as a function of frequency will be defined as the frequency response of the structure. The computed frequency response will make it possible to predict the return of any applied broadband signal and mainly FMCW signals. By computing the return of an applied FMCW signal and performing some additional processing the forward problem is considered complete.

1.4 Thesis Contribution and Outline

The contributions of this research can be summarized in the following points:

- 1) A novel formula was derived to characterize the distribution of the reflection coefficient over the aperture of an open-ended rectangular waveguide.
- 2) We were able to compute the effective complex value of the reflection coefficient of an incident TE_{10} mode for an open ended waveguide illuminating a multilayer dielectric structure.
- 3) A multimode general solution is introduced in details and results from other sources were used as reference values and compared to the results derived in this thesis.
- 4) A novel simple analogy was made which treats multilayer structures as linear time invariant (LTI) systems. This analogy allowed us to define a structure by its frequency response.
- 5) The forward problem of near-field FMCW was established and simulated.
- 6) From the observations made during simulation, ways to solve the inverse problems were suggested as recommended approaches for future work

The chapters to follow are outlined as shown:

Chapter 2: The second chapter contains the required background information required to understand the analysis done in later chapters. It starts with information about the FMCW radar techniques followed by a detailed description of microwave and wave propagation. It also contains the summary of the literature review which sets the base of the work done in this thesis.

Chapter 3: this chapter includes all the mathematical derivations which were developed over the course of this work. Mainly, it contains the derivations of the reflection coefficient for a multilayer structure as well as the multimode solution for a single layer structure.

Chapter 4: It includes all the simulation results and a detailed analysis for each result. It starts with the distribution of the reflection coefficient over the aperture. Then, it shows the comparisons between the results of this thesis with other results from the literature review. It also includes the frequency response simulation along with the FMCW radar simulation results.

Chapter 5: chapter five is the final chapter which summarizes the findings of this thesis and presents recommendations for future work.

CHAPTER 2

BACKGROUND AND LITERATURE REVIEW

This chapter introduces the necessary literature review required to understand the principles of the work done. It starts with some basic information about FMCW radars and how they are expected to operate under ideal working conditions. In addition to some remarks about the major difficulty that might arise in practical implementation. Since electromagnetic waves are used as a medium for the FMCW signal, the second section will be dedicated for electromagnetic waves in general and microwaves in specific. Consequently, dielectrics and their properties —i.e. storage and loss of electric field power mechanisms, are presented.

The rest of the literature review will discuss waveguides, and near- field related topics. Within this category is the near-field waveguide imagers, which will introduce the different types of imaging systems and the convenience they provide relative to other existing techniques. Near the end of this chapter, heavy mathematical derivations describing the near- field interaction of a single frequency and single polarization excitation will be given. The derivations were originally done by [1] and then expanded to cover N-layers general model by [5]. The math was slightly edited for clarification purposes and mathematical consistency.

2.1 FMCW Radars

The term “Radar” stands for Radio Detection and Ranging which is self explanatory. FMCW stands for (Frequency Modulated Continuous Wave). The distinction made between FMCW radars and other basic types of radars (Pulse and Doppler radars) is due to the type of the signal transmitted. The word “Frequency Modulated” means that the frequency of the transmitted signal is modulated or being varied as a function of time. The physical nature of the signal used in radars in general is usually acoustic or electromagnetic. The signal type considered in this thesis is

electromagnetic which is what's usually associated with FMCW radars. The relation between the frequency of the transmitted wave and time is usually represented by a saw-tooth function or a triangle function Figure 2.2.

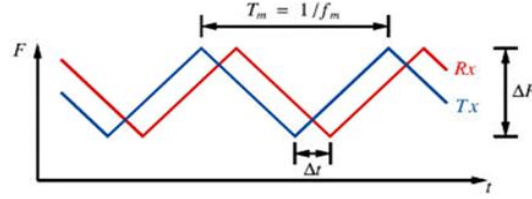


Figure 2.1: Triangular FMCW Time-Frequency Relationship.

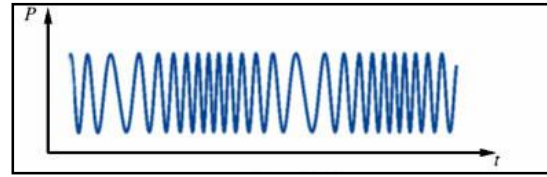


Figure 2.2: Triangular FMCW Time Domain Representation.

2.1.1 FMCW Under Ideal Operating Conditions

The basic principle of FMCW radar is in transmitting a frequency sweep, usually called a chirp. In the presence of a static target, the transmitted signal experiences a time delay due to the distance of the target from the radar, denoted as (R) for range. Assuming the following scenario, FMCW radar generates a chirp starting with frequency (f_0) to (f_1) over a period of time (T_{sw}), known as the sweep period. The frequency range (B) is the difference between f_1 and f_0 which also refers to the approximate bandwidth of the FMCW signal. The linear relationship between the instantaneous frequency of the transmitted signal ($f_T(t)$) and time (t) is shown in Figure 2.3 and can be expressed as:

$$f_T(t) = f_0 + \alpha t \quad 0 < t < T_{sw} \quad (2.1)$$

where (α) is the rate of change in frequency. Hence, the frequency rate of change can be found to be:

$$\alpha = \frac{B}{T_{sw}} \quad (2.2)$$

When the transmitted wave travels a distance R and returns back to the radar, it experiences a time delay (τ) given by:

$$\tau = \frac{2R}{C} \quad (2.3)$$

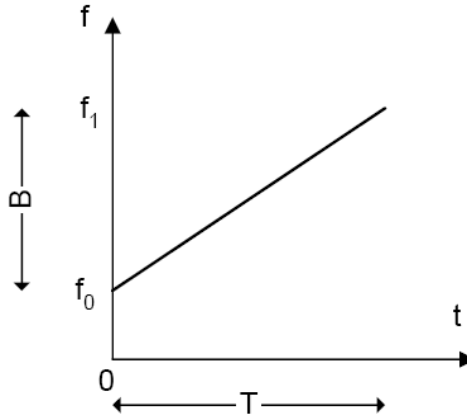


Figure 2.3: FMCW Radar Sweep.

where (C) is the speed of the wave in the medium of propagation.

Therefore, the received return signal ($f_R(t)$) will have the following frequency-time relationship:

$$f_R(t) = f_0 + \alpha \cdot (t - \tau) \quad (2.4)$$

The difference in frequency between the return signal and the transmitted signal is called the beat frequency and is shown in Figure 2.4.

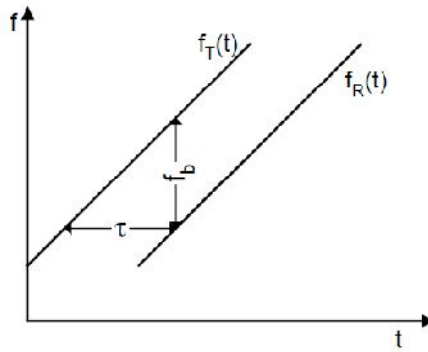


Figure 2.4: FMCW Beat Frequency.

The beat frequency which is the difference between f_T and f_R is constant in case of reflecting from a static target when the delay is fixed:

$$\begin{aligned}
 f_b &= f_T - f_R = \alpha \tau \\
 &= \frac{B}{T_{sw}} \frac{2R}{C} \\
 \text{yields} \rightarrow f_b &= \frac{2BR}{T_{sw}C} \quad (2.5)
 \end{aligned}$$

Having a direct relation between the range and the beat frequency enables us to calculate the range of the target directly from the beat frequency as shown in Equation (2.6) [10].

$$R = \frac{f_b T_{sw} C}{2B} \quad (2.6)$$

2.1.2 FMCW Under Practical Operating Conditions

Under practical conditions FMCW radars suffer mainly from the resolution in the frequency domain when operated on layered structures with thin layers. The resolution of the radar is related to the window size in the frequency domain. In the case of multiple reflections each reflected FMCW signal will produce its own beat frequency in the frequency domain. Since FMCW has a defined sweeping time then the mixed down beat frequency has an infinite bandwidth. The problem in resolution occurs when the beat frequencies overlap and become hard to be decomposed. We will define the minimum detectable electrical length as the maximum reliable resolution using a certain window type. A simple formula can be derived to relate the minimum electrical length for far field FMCW radars. The resolution is a function of the window type (such as Rectangular, Hamming, Blackman, etc...), FMCW bandwidth, and the dielectric constant of the measured layer.

$$\Delta f_{min} = K_{win} \frac{f_s}{L} = K_{win} \frac{f_s}{f_s T_{sw}} = K_{win} \frac{1}{T_{sw}} \quad (2.7)$$

$$\Delta f_{min} = f_{beat2} - f_{beat1} = \frac{BW}{T_{sw}} \times (t_2 - t_1) = \frac{BW}{T_{sw}} \times \tau = \frac{BW}{T_{sw}} \times \frac{2D_{th}}{v} \quad (2.8)$$

By equating Equations (2.7) and (2.8):

$$\frac{BW}{T_{sw}} \times \frac{2D_{th}}{v} = K_{win} \frac{1}{T_{sw}}$$

$$BW \times \frac{2D_{th}}{v} = K_{win}$$

$$D_{th} = \frac{K_{win}}{2BW} \cdot v$$

$$D_{th} = \left[\frac{K_{win}}{2BW} \cdot \frac{c}{real(\sqrt{\epsilon_r})} \right] \quad (2.9)$$

where f_s is the sampling frequency, L is the number of samples, D_{th} is the minimum detectable thickness, K_{win} is a constant related to the window type, $K_{win} = 1$

(rectangular window), $K_{win} = 2$ (Hamming window), c is the speed of light in free space in m/s , BW is the FMCW signal bandwidth in Hertz, ϵ_r is the relative permittivity of the material with the thickness D_{th} and T_{sw} is the Sweep Time of the FMCW signal.

Equation (2.9) does not provide a hard limit on the resolution but conventional frequency transformation fails to separate the components if the limit was exceeded. Other researchers employed other techniques to improve the resolution of FMCW radars by means of signal processing such as the Multiple Signal Classification (MUSIC) algorithm which provides a significant resolution improvement for high signal to noise ratio (SNR) [11].

2.2 Microwaves

Microwaves are referred to alternating electromagnetic waves with frequencies varying between $300MHz$ (corresponding to $\lambda = 1m$) and $300GHz$ ($\lambda = 1mm$) with reference to the speed of light in free space ($c = 3 \times 10^8 m/s$). The microwave spectrum includes ultra-high frequency (UHF) (0.3-3 GHz), super high frequency (SHF) (3-30 GHz), and extremely high frequency (EHF) (30-300 GHz) signals. The microwave spectrum is bounded by the infrared and Radio frequencies Figure 2.5.

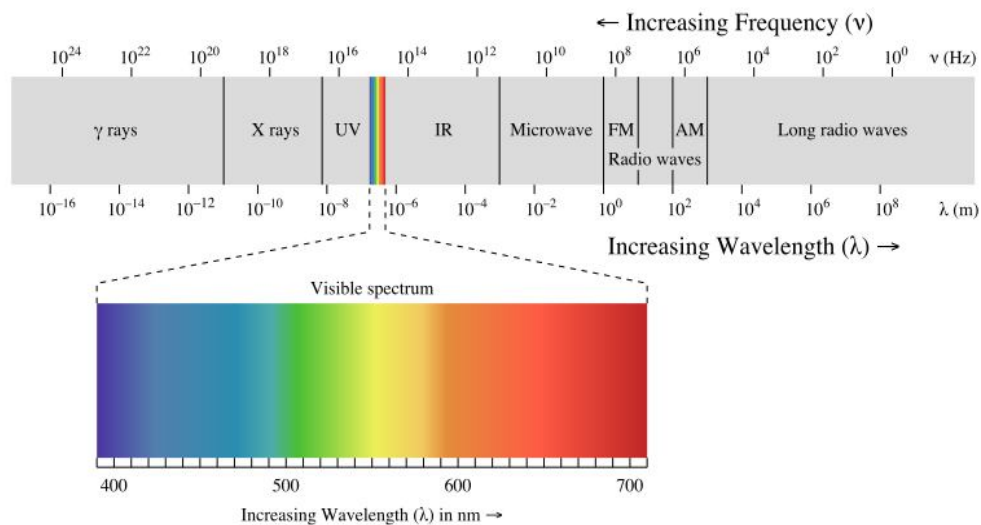


Figure 2.5: The electromagnetic spectrum showing the location of the microwave spectrum.

2.2.1 Microwave Frequency Bands

Most of the common applications using microwaves are within the frequency range between 1 and 40 GHz. This range is classified in Table 2.1:

Table 2.1: Microwaves Frequency bands.

Designation	Frequency range	Designation	Frequency range
L band	1.12 to 1.7 GHz	W band	7.05 to 10 GHz
R band	1.7 to 2.6 GHz	X band	8.2 to 12.4 GHz
S band	2.6 to 3.95 GHz	Ku band	12.4 to 18 GHz
H band	3.95 to 5.85 GHz	K band	18 to 26.5 GHz
C band	5.85 to 8.2 GHz	Ka band	26.5 to 40 GHz

To put microwaves in a mathematical context, it is conventional to start off with Maxwell's equations. James Clerk Maxwell had summarized the mathematical model of electromagnetic waves in a neat set of four equations consisting of two curls and two divergences Equations (2.10) to (2.13):

From Faraday's law of induction:

$$\nabla \times \vec{E} = -\frac{d\vec{B}}{dt} \quad (2.10)$$

From Ampère's Circuital Law (with Maxwell's extension):

$$\nabla \times \vec{H} = \vec{J} + \frac{d\vec{D}}{dt} \quad (2.11)$$

From Gauss's law:

$$\nabla \cdot \vec{D} = \rho \quad (2.12)$$

From Gauss' law for magnetism (absence of magnetic monopoles):

$$\nabla \cdot \vec{B} = 0 \quad (2.13)$$

These four equations are the building block of all electromagnetic derivations [12]. The variables are defined in Table 2.2.

Table 2.2: Variable definitions in Maxwell's equations (Arrow denotes a vector quantity).

Symbol	Meaning	SI units of measure
\vec{E}	electric field Intensity	V/m or, equivalently, Newton per coulomb $N/Coul$
\vec{H}	magnetic field also called the auxiliary field	Ampere per meter A/m
\vec{D}	The electric flux density	$Coul/m^2$
\vec{B}	Magnetic flux density	Wb/m^2
ρ	Electric charge density	$Coul/m^3$
\vec{J}	Electric current density	A/m^2

2.2.2 Dielectric Media

A dielectric medium is any medium that has a dielectric property different than free space and is not considered a conductor. A constant with symbol ϵ_r is given to denote the relative permittivity from that of free space (ϵ_o). In theory, the relative permittivity of a material constitutes of two parts real and imaginary. The real part corresponds to the ability of the material to store the electric field energy relative to free space while the imaginary part corresponds to the loss factor or the tendency of the material to dissipate electric field energy. The permittivity constant is used to relate the electric flux density to the electric field intensity according to the relation $\vec{D} = \epsilon\vec{E}$. If the medium has finite conductivity then according to Maxwell equations when we assume harmonic electric field with angular frequency (ω) :

$$\nabla \times \vec{H} = j\omega\epsilon\vec{E} + \sigma\vec{E} \quad (2.14)$$

$$\xrightarrow{\text{yields}} \nabla \times \vec{H} = j\omega\vec{E}\epsilon\left(1 - j\frac{\sigma}{\omega\epsilon}\right) \quad (2.15)$$

From Equation (2.15) we refer to the term $\left[\epsilon\left(1 - j\frac{\sigma}{\omega\epsilon}\right)\right]$ as the complex permittivity constant of a material which can be written as

$$\epsilon\left(1 - j\frac{\sigma}{\omega\epsilon}\right) = \epsilon_o\epsilon_r = \epsilon_o(\epsilon_r - j\epsilon_r') = \epsilon_o(\epsilon_r - j\sigma/\omega\epsilon_o) \quad (2.16)$$

$$\epsilon_r = \epsilon_r - j\epsilon_r' = \epsilon_r\left(1 - j\frac{\epsilon_r'}{\epsilon_r}\right) = \epsilon_r(1 - j\tan(\delta)) \quad (2.17)$$

We can notice that the imaginary part which is related to the ability of the material to dissipate electric energy is related to frequency and conductivity. However, the relation between the loss and frequency is not directly derived from this equation.

2.3 Waveguide Wave Propagation

Maxwell's Equations (2.10) through (2.13) can be rewritten for a source free region and harmonic time dependence as shown in Equations (2.18) to (2.21).

$$\nabla \times \vec{H} = j\omega\epsilon\vec{E} \quad (2.18)$$

$$\nabla \times \vec{E} = -j\omega\mu\vec{H} \quad (2.19)$$

$$\nabla \cdot \vec{D} = 0 \quad (2.20)$$

$$\nabla \cdot \vec{B} = 0 \quad (2.21)$$

In general, the vectors \vec{E} and \vec{H} have three components, one for each spatial coordinate. The notation used for these components is a subscript denoting a vector in the direction of (x , y or z).

$$\vec{E} = E_x\hat{x} + E_y\hat{y} + E_z\hat{z}$$

$$\vec{H} = H_x\hat{x} + H_y\hat{y} + H_z\hat{z}$$

The general solution for the previous scenario is known to be of sinusoidal nature and will be derived later under the near- field derivations subsection. The solution can be written as shown in Equations (2.22) and (2.23) assuming wave propagation in the direction of the positive z axis.

$$\vec{E}(x, y, z) = (E_x(x, y)\hat{x} + E_y(x, y)\hat{y} + E_z(x, y)\hat{z})e^{-j\beta z} \quad (2.22)$$

$$\vec{H}(x, y, z) = (H_x(x, y)\hat{x} + H_y(x, y)\hat{y} + H_z(x, y)\hat{z})e^{-j\beta z} \quad (2.23)$$

With an $e^{-j\beta z}$ dependence, we can expand (2.18) and (2.19) to obtain the reduced form of the three components for the previous vector equations.

$$\frac{\partial E_z}{\partial y} + j\beta E_y = -j\omega\mu H_x \quad (2.24)$$

$$-\frac{\partial E_z}{\partial x} - j\beta E_x = -j\omega\mu H_y \quad (2.25)$$

$$\frac{\partial E_y}{\partial x} - \frac{\partial E_x}{\partial y} = -j\omega\mu H_z \quad (2.26)$$

$$\frac{\partial H_z}{\partial y} + j\beta H_y = j\omega\varepsilon E_x \quad (2.27)$$

$$-\frac{\partial H_z}{\partial x} - j\beta H_x = j\omega\varepsilon E_y \quad (2.28)$$

$$\frac{\partial H_y}{\partial x} - \frac{\partial H_x}{\partial y} = j\omega\varepsilon E_z \quad (2.29)$$

The previous six equations can be rewritten in terms of the transverse fields E_x, E_y, H_x and H_y and written in terms of E_z and H_z Equations (2.30) to (2.33)

$$H_x = \frac{j}{k_c^2} \left(\omega \varepsilon \frac{\partial E_z}{\partial y} - \beta \frac{\partial H_z}{\partial x} \right) \quad (2.30)$$

$$H_y = \frac{-j}{k_c^2} \left(\omega \varepsilon \frac{\partial E_z}{\partial x} + \beta \frac{\partial H_z}{\partial y} \right) \quad (2.31)$$

$$E_x = \frac{-j}{k_c^2} \left(\beta \frac{\partial E_z}{\partial x} + \omega \mu \frac{\partial H_z}{\partial y} \right) \quad (2.32)$$

$$E_y = \frac{j}{k_c^2} \left(-\beta \frac{\partial E_z}{\partial y} + \omega \mu \frac{\partial H_z}{\partial x} \right) \quad (2.33)$$

Where $k_c^2 = K^2 - \beta^2$ and $K = \omega \sqrt{\mu \varepsilon} = 2\pi/\lambda$ and λ is the wavelength of the electromagnetic wave inside the medium of propagation.

Equations (2.30) through (2.33) are the basis of wave propagation in any source free medium. In waveguides made of a single conductor, it was proven that both hertzian fields E_z and H_z cannot be zero. Hence, the allowed modes of wave propagation inside a rectangular waveguide are either Transverse electric TE ($E_z = 0$) or transverse magnetic TM ($H_z = 0$). The general formulas for TE and TM modes are shown in Table 2.3.

Table 2.3: TE and TM Modes' Equations for Rectangular Waveguides.

TE_{mn}	TM_{mn}
$H_z^i(x, y, z) = A_{mn} \cos\left(\frac{m\pi}{a}x\right) \cos\left(\frac{n\pi}{b}y\right) e^{-j\beta z}$	$E_z^i(x, y, z) = A_{mn} \sin\left(\frac{m\pi}{a}x\right) \sin\left(\frac{n\pi}{b}y\right) e^{-j\beta z}$
$E_{x_{mn}}^i(x, y, z) = \frac{j\omega\mu n\pi}{k_{mn}^2 b} A_{mn} \cos\left(\frac{m\pi}{a}x\right) \sin\left(\frac{n\pi}{b}y\right) e^{-j\beta z}$	$E_{x_{mn}}^i(x, y, z) = \frac{-j\beta m\pi}{k_{mn}^2 a} A_{mn} \cos\left(\frac{m\pi}{a}x\right) \sin\left(\frac{n\pi}{b}y\right) e^{-j\beta z}$
$E_{y_{mn}}^i(x, y, z) = \frac{-j\omega\mu m\pi}{k_{mn}^2 a} A_{mn} \sin\left(\frac{m\pi}{a}x\right) \cos\left(\frac{n\pi}{b}y\right) e^{-j\beta z}$	$E_{y_{mn}}^i(x, y, z) = \frac{-j\beta n\pi}{k_{mn}^2 b} A_{mn} \sin\left(\frac{m\pi}{a}x\right) \cos\left(\frac{n\pi}{b}y\right) e^{-j\beta z}$
$H_{x_{mn}}^i(x, y, z) = \frac{j\beta m\pi}{k_{mn}^2 a} A_{mn} \sin\left(\frac{m\pi}{a}x\right) \cos\left(\frac{n\pi}{b}y\right) e^{-j\beta z}$	$H_{x_{mn}}^i(x, y, z) = \frac{j\omega\varepsilon n\pi}{k_{mn}^2 b} A_{mn} \sin\left(\frac{m\pi}{a}x\right) \cos\left(\frac{n\pi}{b}y\right) e^{-j\beta z}$
$H_{y_{mn}}^i(x, y, z) = \frac{j\beta n\pi}{k_{mn}^2 b} A_{mn} \cos\left(\frac{m\pi}{a}x\right) \sin\left(\frac{n\pi}{b}y\right) e^{-j\beta z}$	$H_{y_{mn}}^i(x, y, z) = \frac{-j\omega\varepsilon m\pi}{k_{mn}^2 a} A_{mn} \cos\left(\frac{m\pi}{a}x\right) \sin\left(\frac{n\pi}{b}y\right) e^{-j\beta z}$
Where: $k_{mn}^2 = \left(\frac{m\pi}{a}\right)^2 + \left(\frac{n\pi}{b}\right)^2$, $\beta = \sqrt{k^2 - k_{mn}^2}$, $k = \omega\sqrt{\mu\varepsilon} = 2\pi/\lambda$	

2.3.1 Modes Propagation Conditions

Each mode has a cutoff frequency under which it does not propagate within the waveguide. The cutoff frequency for any (m,n) mode ($f_{c_{mn}}$) is given by Equation (2.34).

$$f_{c_{mn}} = \frac{\sqrt{\left(\frac{m\pi}{a}\right)^2 + \left(\frac{n\pi}{b}\right)^2}}{2\pi\sqrt{\mu\varepsilon}} \quad (2.34)$$

Any mode that is forced into the waveguide below its cutoff frequency will start to decay exponentially as a function of distance since $j\beta$ for that mode becomes a pure real number α . That happens when $k < k_{mn}$ as shown in Equation (2.35).

$$\alpha = j\beta = \sqrt{k_{mn}^2 - k^2} \quad (2.35)$$

When such a mode is generated it is known as an Evanescent mode. Evanescent modes carry reactive energy and are usually generated at discontinuities such as coaxial to waveguide adapters, interconnects and transmission lines that are partially loaded with a dielectric material etc. In general any discontinuity or transition could generate higher order modes which in turn cannot propagate if the operating frequency is below its cutoff frequency. It is important to note that some discontinuities such as moving from an empty waveguide region to a fully loaded waveguide region will not generate any higher order modes if the change is uniform in the xy -plane.

To illustrate why evanescent modes do not propagate much within a waveguide observe Figure 2.6 which shows the attenuation constant and propagation constant before and after the cutoff frequency, respectively. α is the attenuation constant when operating below the cutoff frequency of a certain mode. It is measured in *Nepers/meter* (Np/m). The Neper uses the natural logarithm $\ln(x)$ instead of the logarithm to base ten $\log_{10}(x)$ which is the logarithm in the more commonly used decibel (dB) unit. Each Np/m is equivalent to:

$$1Np/m = 20 / \ln(10) \text{ dB}/m \cong 8.68588 \text{ dB}/m \quad (2.36)$$

By observing the values of α before the cutoff frequency it is evident that evanescent modes die extremely quickly in a waveguide.

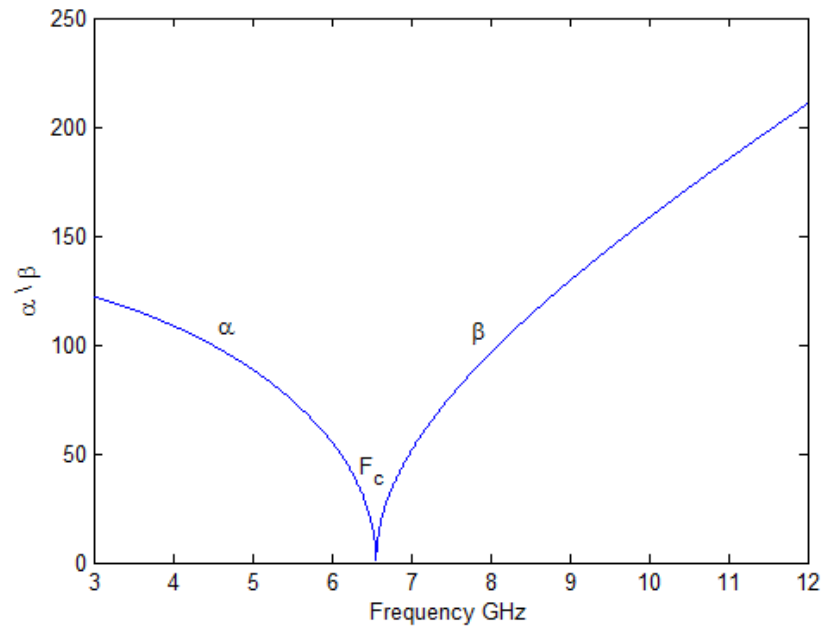


Figure 2.6. An illustration of the relationship between attenuation constant α and propagation constant β as a function of frequency for TE_{10} mode in an X-band waveguide.

2.4 Near-Field Waveguide-Based Imagers

Near-field microwave waveguide-based imaging systems proved to be useful in different applications due to the following factors:

- **Economic:** Microwave imaging systems are simple, cost effective, battery operated and do not require operator expertise sometimes.
- **Environment, Health and Safety:** The low power radiated by the probes makes them environmentally friendly, safe for human beings and an attractive tool in medical applications. Actually, it is considered much safer than most of the existing non-destructive techniques.
- **Manufacturability:** It is relatively simple to manufacture a near-field microwave imaging system. The main components are a waveguide, a gun oscillator, a diode detector and a simple electronic circuit for amplification if needed.
- **Social:** Having a reliable detection systems for many applications can help in avoiding great losses due to the imperfection of some materials, —i.e. early detection of disbonds in composites, corrosion in metals or tumor in breast

can save a lot of money as well as human's lives. This in turn improves the quality of life.

- **Sustainability:** Usually, the waveguide and the diode detector last for long time. The most sensitive part is the gun-diode, which can last for long time as long as it is well maintained.

Imaging is based on the fact that electromagnetic waves experience different reflections when they penetrate different media. Basically, an open-ended waveguide is used to launch electromagnetic waves into the inspected material. From a microwave point of view, an inclusion is characterized by a change in the dielectric properties of the material and hence the magnitude and the phase of the reflected wave will change as well. By monitoring the reflected signal, the complex reflection coefficient, or signal proportional to it, information about defects may be obtained. A change in the magnitude and/or the phase of the reflection coefficient will not only inform the inspector about the existence of the inclusion, but also it conveys valuable information about the size, location, type and the orientation of the inclusion.

In general, microwave nondestructive testing techniques are classified into two main categories: near-field and far-field systems. As the name implies, the material is placed in the near-field region of the microwave sensor in the former case while it is placed in the far field region in the latter one. Each category has its own applications, advantages, and disadvantages. In this project, the focus will be on near-field systems. Specifically, the imaging probe to be used is an open-ended waveguide to illuminate the material under inspection with electromagnetic waves and the return signal will be monitored and analyzed.

2.4.1 Types of Captured Images

As we mentioned above, the reflection coefficient is a complex parameter that depends directly on the properties of the material discontinuities. Using special microwave circuitry, Scatterometer, we can measure the phase and the magnitude of the reflection coefficient. According to measured parameters, there are three types of images, and hence three realizations of the near-field waveguide-based imagers.

2.4.1.1. Phase Images

In a phase imaging system, the intensity of each point in the captured image is proportionally related to the phase difference between the transmitted and the reflected waves. A Scatterometer microwave circuit can be used for this purpose. A basic block diagram is shown in Figure 2.7 [5].

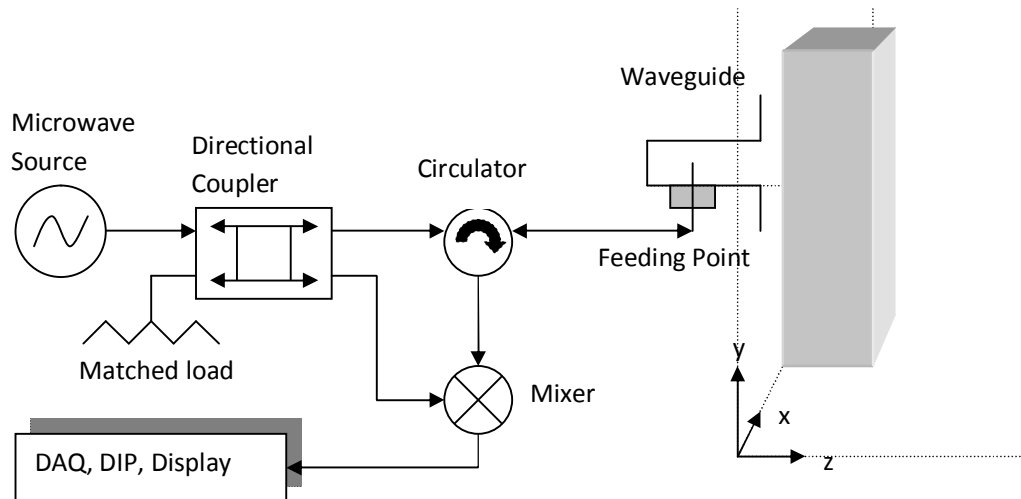


Figure 2.7: Phase imager Scatterometer diagram, the waveguide is scanned in the xy -plane.

The microwave oscillator is used to generate electromagnetic waves in the microwave frequency range. The directional coupler is used to split the signal into two parts. Part of the signal will be fed into a circulator and the other part, which has less power, will be fed into a mixer as a reference signal. The output of circulator will be fed into a waveguide that is used to illuminate the structure with electromagnetic waves. The reflected waves will bounce back to the circulator, which will isolate it from the transmitted signal and feed it to the mixer. The input to mixer will be the reference signal, which carries the information about the phase of the transmitted signal, and the reflected signal. Since the material under inspection is stationary, no change in the frequency of the reflected signal is introduced, which means that the reference signal and the reflected signal will differ only in the phase. The output of the mixer will be a DC voltage proportionally related to the phase difference.

2.4.1.2. Magnitude Images

In a magnitude imaging system, the intensity of each point in the captured image is proportionally related to the magnitude of the reflection coefficient. A possible realization of the microwave circuit is shown in Figure 2.8.

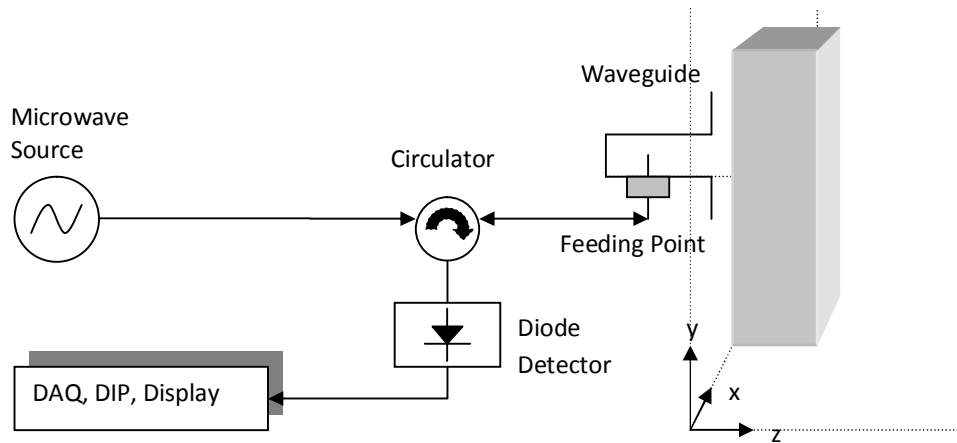


Figure 2.8: Magnitude Imager Scatterometer circuit diagram, the waveguide scans in the xy -plane.

The microwave oscillator is used to generate electromagnetic waves in the microwave frequency range. The microwave signal is fed into the circulator which in turns directs it to a waveguide that is used to illuminate the structure with electromagnetic waves. The reflected waves will bounce back to the circulator, which will isolate it from the transmitted signal and feed it to the diode detector. The diode detector output is a DC voltage that is proportional to the reflected power and hence proportional to the squared magnitude of the reflection coefficient which depends on the input admittance seen at the aperture [5].

2.4.1.3. Complex Images

In a complex imaging system, the intensity of each point in the captured image is proportionally related to the power of the standing wave, which is a resultant of both the transmitted and the reflected waves. A complex imaging system can be implemented in a way similar to that used in magnitude imaging system but without the circulator.

2.5 Near-Field Single Frequency Mathematical Modelling

This section will include the mathematical derivation done by [5]. They model the interaction of linearly polarized electric field with stratified media consisting of N -layers. The modelling was done such that the equations work for both near-field and far field ranges of the open-ended rectangular waveguide

To model near-field radiation within a structure the setup needs to be defined and the assumptions need to be stated. As shown in Figure 2.9, the rectangular

waveguide's (RWG's) aperture lies in the xy -plane at $z = 0$. The aperture has dimensions (a) along x and (b) along y and is mounted on an electrically infinite flange to control the boundary conditions at $z = 0$. When observing the front view of the aperture, its left bottom corner is also considered as the origin of the rectangular coordinate system. The layers are modeled according to their spatial order (n), $n = 1..N$, depth (d_n) at which the layer ends and complex relative permittivity relative to free space, (ϵ_{r_n}). The electromagnetic radiation is modeled as the solution to the homogenous wave equation within the region $z > 0$. Uniqueness theory guarantees a unique solution when all the boundary conditions are defined around the source free region.

The model assumes simple media, such that the permittivity does not vary as a function of electric field strength (linear), as a function of the location (homogenous), or as a function of the direction of the polarizing field (isotropic). It is also assumed that the structure consists of finite number of stratified layers where the last layer is an infinite half space of a dielectric or a perfectly conducting sheet. The layers lay in a source free region and they extend infinitely over the xy -plane. Interfaces between dielectrics are flat and defined as depth in z . The media are non-magnetic and defined solely on the complex relative dielectric property ϵ_{r_n} for each layer. The waveguide is operating at its dominant mode TE_{10} , and the frequency is low enough such that no higher modes exist on the aperture.

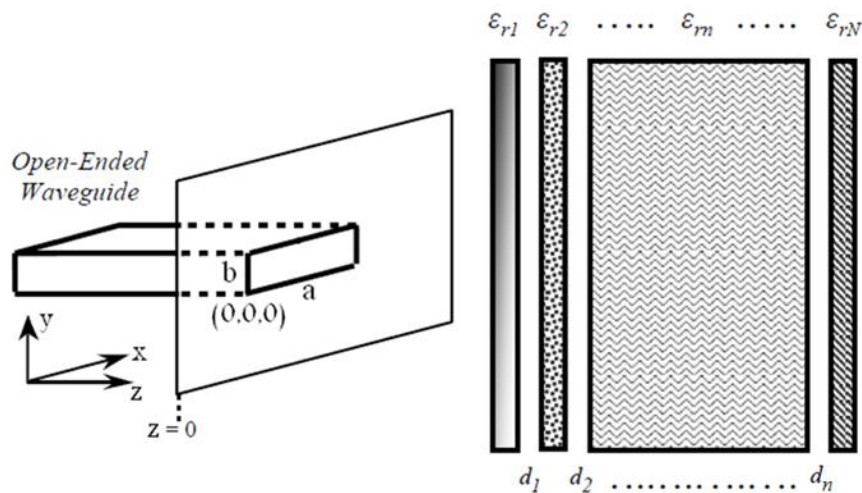


Figure 2.9: Problem setup viewed in the yz -plane.

Abou Khousa [5] was successful in computing the electric and the magnetic field coefficients for any layered structure radiated by a rectangular waveguide as a function of the space coordinates under single frequency operation. The intention is to find the electric field's coefficients in each layer. For TE_{10} mode, the excitation aperture fields are,

$$\vec{E}_{ap}(x, y) = \hat{y}(1 + \Gamma(x, y)) \frac{j\pi\omega\mu}{ak_{10}^2} \sin\left(\frac{\pi}{a}x\right) \quad (2.37)$$

$$\vec{H}_{ap}(x, y) = \hat{x}(1 - \Gamma(x, y)) \frac{-j\pi\omega\mu}{ak_{10}^2} Y_o \sin\left(\frac{\pi}{a}x\right) \quad (2.38)$$

Where:

$k_{10} = \frac{\pi}{a}$, and a is the broad dimension of the waveguide

$Y_o = \frac{\sqrt{K^2 - k_{10}^2}}{\omega\mu}$, is the admittance of the fundamental mode.

$K^2 = K_o^2 \epsilon_r \mu_r$, and K_o is the free space wave number

$K_o = \frac{2\pi}{\lambda_o}$, and λ_o is the free space wave length at the frequency of operation.

$\Gamma(x, y)$, is the reflection coefficient as a function of the spatial coordinates x and y .

Starting from Maxwell's equations, we can obtain the field solution by applying Fourier Transform technique. This involves expanding the field in each layer in terms of the Fourier Integrals and applying boundary conditions at each interface. Having the solution for the field in the first layer, the reflection coefficient is calculated by matching the magnetic field expression on both sides of the waveguide's aperture.

In a source free region Maxwell's equations will be rewritten for ease of tracking as:

$$\nabla \times \vec{E}(x, y, z) = -j\omega\mu\vec{H}(x, y, z) \quad (2.39)$$

$$\nabla \times \vec{H}(x, y, z) = j\omega\epsilon\vec{E}(x, y, z) \quad (2.40)$$

$$\nabla \cdot \vec{E}(x, y, z) = 0 \quad (2.41)$$

$$\nabla \cdot \vec{H}(x, y, z) = 0 \quad (2.42)$$

Taking the curl of Equation (2.39)

$$\nabla \times \nabla \times \vec{E}(x, y, z) = -j\omega\mu \nabla \times \vec{H}(x, y, z) \quad (2.43)$$

Substitution of Equation (2.40) and (2.41) in the previous equation yields the wave equation in the source-free region:

$$\nabla \left(\nabla \cdot \vec{E}(x, y, z) \right) - \nabla^2 \vec{E}(x, y, z) = \omega^2 \mu \varepsilon \vec{E}(x, y, z) \quad (2.44)$$

$$\nabla^2 \vec{E}(x, y, z) + K^2 \vec{E}(x, y, z) = 0 \quad (2.45)$$

Where: $K^2 = K_o^2 \varepsilon_r \mu_r$

The solution of the wave equation can be expressed in term of the Fourier integrals.

$$\vec{E}(x, y, z) = \int_{-\infty}^{\infty} \int_{-\infty}^{\infty} \vec{\tilde{E}}(k_x, k_y, z) e^{j(k_x x + k_y y)} dk_x dk_y \quad (2.46)$$

Substituting (2.46) in (2.45) yields:

$$\frac{d^2 \vec{\tilde{E}}(k_x, k_y, z)}{dz^2} - \gamma^2 \vec{\tilde{E}}(k_x, k_y, z) = 0 \quad (2.47)$$

Where $\gamma = \sqrt{k_x^2 + k_y^2 - K^2}$

The solution of Equation (2.47) is:

$$\vec{\tilde{E}}(k_x, k_y, z) = \vec{A} e^{-\gamma z} + \vec{B} e^{\gamma z} \quad (2.48)$$

Where,

$$\vec{A} = A_x \hat{x} + A_y \hat{y} + A_z \hat{z}$$

$$\vec{B} = B_x \hat{x} + B_y \hat{y} + B_z \hat{z}$$

Substituting Equation (2.48) in Equation (2.46) yields:

$$\vec{E}(x, y, z) = \int_{-\infty}^{\infty} \int_{-\infty}^{\infty} [\hat{x}(A_x e^{-\gamma z} + B_x e^{\gamma z}) + \hat{y}(A_y e^{-\gamma z} + B_y e^{\gamma z}) + \hat{z}(A_z e^{-\gamma z} + B_z e^{\gamma z})] e^{j(k_x x + k_y y)} dk_x dk_y \quad (2.49)$$

Applying Equation (2.41) on Equation (2.49), the following relations are obtained.

$$(jk_x A_x + jk_y A_y - \gamma A_z) e^{-\gamma z} = 0$$

$$(jk_x B_x + jk_y B_y + \gamma B_z) e^{\gamma z} = 0$$

$$A_z = \frac{jk_x A_x + jk_y A_y}{\gamma}$$

$$B_z = \frac{-jk_x B_x - jk_y B_y}{\gamma}$$

Using the above relations, Equation (2.49) can be written as.

$$\begin{aligned} \vec{E}(x, y, z) = \int_{-\infty}^{\infty} \int_{-\infty}^{\infty} & \left[A_x \left(\hat{x} + \hat{z} \frac{jk_x}{\gamma} \right) + A_y \left(\hat{y} + \hat{z} \frac{jk_y}{\gamma} \right) \right] e^{-\gamma z} \\ & + \left[B_x \left(\hat{x} - \hat{z} \frac{jk_x}{\gamma} \right) + B_y \left(\hat{y} - \hat{z} \frac{jk_y}{\gamma} \right) \right] e^{\gamma z} e^{j(k_x x + k_y y)} dk_x dk_y \end{aligned} \quad (2.50)$$

By applying Equation (2.40) on Equation (2.50), the \vec{H} field is given by:

$$\vec{H}(x, y, z) = \frac{j}{\omega \mu} \int_{-\infty}^{\infty} \int_{-\infty}^{\infty} [(\tilde{c}_1 A_x + \tilde{c}_2 A_y) e^{-\gamma z} + (\tilde{c}_3 B_x + \tilde{c}_4 B_y) e^{\gamma z}] e^{j(k_x x + k_y y)} dk_x dk_y \quad (2.51)$$

Where,

$$\tilde{c}_1 = -\hat{x} \frac{k_x k_y}{\gamma} + \hat{y} \frac{K^2 - k_y^2}{\gamma} - \hat{z} (jk_y)$$

$$\tilde{c}_2 = -\hat{x} \frac{K^2 - k_x^2}{\gamma} + \hat{y} \frac{k_x k_y}{\gamma} + \hat{z} (jk_x)$$

$$\tilde{c}_3 = \hat{x} \frac{k_x k_y}{\gamma} - \hat{y} \frac{K^2 - k_y^2}{\gamma} - \hat{z} (jk_y)$$

$$\tilde{c}_4 = \hat{x} \frac{K^2 - k_x^2}{\gamma} - \hat{y} \frac{k_x k_y}{\gamma} + \hat{z} (jk_x)$$

Since we have N-layers, assume $\mu_n = \mu_o \forall n$ for paramagnetic and diamagnetic materials (i.e. nonmagnetic material).

From Equation (2.37) we notice that the excitation field is y-directed only. Therefore,

$$A_{xn} = 0 \quad \forall n$$

$$B_{xn} = 0 \quad \forall n$$

Then, the electric field has z and y components in the n^{th} layer as follows,

$$\tilde{E}_{yn}(k_x, k_y, z) = A_{yn} e^{-\gamma_n z} + B_{yn} e^{\gamma_n z} \quad (2.52)$$

$$\tilde{E}_{zn}(k_x, k_y, z) = \frac{jk_y A_{yn}}{\gamma_n} e^{-\gamma_n z} - \frac{jk_y B_{yn}}{\gamma_n} e^{\gamma_n z} \quad (2.53)$$

The y-component of the electric field in the n^{th} layer is,

$$E_{yn}(x, y, z) = \int_{-\infty}^{\infty} \int_{-\infty}^{\infty} \tilde{E}_{yn}(k_x, k_y, z) e^{j(k_x x + k_y y)} dk_x dk_y \quad (2.54)$$

The z-component of the electric field in the n^{th} layer is,

$$E_{zn}(x, y, z) = \int_{-\infty}^{\infty} \int_{-\infty}^{\infty} \tilde{E}_{zn}(k_x, k_y, z) e^{j(k_x x + k_y y)} dk_x dk_y \quad (2.55)$$

Also, the \vec{H} field in each layer is found using Equation (2.51),

$$\vec{H}_n(x, y, z) = \frac{j}{\omega\mu} \int_{-\infty}^{\infty} \int_{-\infty}^{\infty} (\tilde{c}_{2n} A_{yn} e^{-\gamma_n z} + \tilde{c}_{4n} B_{yn} e^{\gamma_n z}) e^{j(k_x x + k_y y)} dk_x dk_y \quad (2.56)$$

By enforcing the appropriate boundary conditions at the boundaries between the layers, the field coefficients A_{yn} and $B_{yn} \forall n$ are determined [5].

2.5.1 General N-Layer Composite Terminated with IHS

The derivations done by [5] lead to a general form for the solution of A_{yn} and B_{yn} for N-layers terminated with IHS.

$$A_{yn} = \left\{ \begin{array}{ll} \frac{(\prod_{i=1}^n G_{i-1}) I}{1 + g_1} \phi_{n-1} & : n \in [1, N - 1] \\ \frac{(\prod_{i=1}^{n-1} G_{i-1}) I}{1 + g_1} (1 + g_{n-1} e^{2\gamma_{n-1} d_{n-1}}) \phi_{n-1} & : n = N \end{array} \right\} \quad (2.57)$$

$$B_{yn} = g_n A_{yn} \quad (2.58)$$

Where, n is the layer we want to solve for, and N is the total number of layers.

$$I = A_{y1} + B_{y1} = \frac{1}{(2\pi)^2} \int_0^b \int_0^a \vec{E}_{ap}(x, y) e^{-j(k_x x + k_y y)} dx dy$$

$$g_i = \left\{ \begin{array}{ll} \frac{C_i - C_{i+1} M_i}{C_i + C_{i+1} M_i} e^{-2\gamma_i d_i} & : i \in [1, N - 1] \\ 0 & : i = 0, i = N \end{array} \right\}$$

$$C_i = \frac{K_i^2 - k_x^2}{\gamma_i}$$

$$M_i = \left\{ \begin{array}{l} \frac{1 - g_{i+1}e^{2\gamma_{i+1}d_i}}{1 + g_{i+1}e^{2\gamma_{i+1}d_i}} \\ 1 \end{array} \quad \begin{array}{l} : i \in [1, N - 2] \\ : i = N - 1 \end{array} \right\}$$

$$G_i = \left\{ \begin{array}{l} 1 \\ \frac{1 + g_i e^{2\gamma_i d_i}}{1 + g_{i+1} e^{2\gamma_{i+1} d_i}} \end{array} \quad \begin{array}{l} : i \leq 0 \\ : i \in [1, N - 2] \end{array} \right\}$$

$$\Phi_i = \left\{ \begin{array}{l} 1 \\ \prod_{j=1}^i e^{-\gamma_j d_j} e^{\gamma_{j+1} d_j} \end{array} \quad \begin{array}{l} : i = 0 \\ : i \in [1, N - 1] \end{array} \right\}$$

2.6 Multimode Solutions

Multimode solutions differ from the previous approach by considering the independent modes being generated at the aperture. The exact analytical solution for near-field open-ended RWG includes an infinite set of linear equations. The multimode solution usually predicts the modes that are most significant and includes them in the solution while ignoring the rest of the modes. The more modes that are considered in the solution the more it approaches convergence.

Many researchers have tried to simplify the infinite set of equations using different methods [13]. The multimode approach will be attempted in the derivations chapter but will not be implemented. The purpose is to show the complexity behind it and it is applicable only to a single layer. Simulation results will be compared to one of the papers who followed the multimode method.

CHAPTER 3

MATHEMATICAL DERIVATIONS

This chapter contains the original mathematical work done during the research period. Part of the work is based on the assumptions made by [5] and [1] and will be stated clearly within the proper context. The chapter starts by studying the reflection coefficient Γ over the waveguide's aperture. After deriving Γ as a function of (x, y) coordinates, further mathematical manipulation is performed to compute the effective value of the reflection coefficient. Additional simplification provides a possible alternative formula to the effective value of Γ .

Another approach will be taken to compute the reflection coefficient using multimode solution. A general model will be derived to work for any excitation mode even when operating beyond the dominant mode frequency. However, the general model is not going to be simulated. A discussion containing more details can be found in the simulation and analysis chapter.

3.1 The Reflection Coefficient's Derivations

Using the derivations of [5] which are shown in the background section we were able to arrive to an expression that relates the magnetic and electric fields outside and inside the aperture. However, little contribution was done to compute the reflection coefficient which was assumed to be a constant value over the waveguide's aperture. Researchers such as [13] and [14] have shown that the discontinuity at the waveguide's aperture from bounded to unbounded propagation will result in the excitation of higher order modes. Such a result has a direct impact on the nature of the reflection at the waveguide's aperture. Excitation of higher order modes means that the wave front was not reflected equally over the aperture and the unequal distribution of Γ is what resulted in the excitation of those modes. Due to the complex nature of

the problem some valid assumptions are made to simplify the matter and they are given as follows:

- The waveguide is operating at its dominant mode TE_{10} , and the frequency is low enough such that no higher modes are incident on the aperture.
- Higher order modes will be excited from the original incident mode.
- The field at the aperture is only polarized in the direction of y
- The reflection coefficient has a spatial distribution in the xy -plane.
- The reflection coefficient acting on the electric field is the same one acting on the magnetic field over the aperture.

With these assumptions we can start the problem of finding $\Gamma(x, y)$. The field outside the waveguide is given by Equation (3.1).

$$\begin{aligned} \vec{H}_{outside}(x, y, z) = & \frac{j}{\omega\mu} \int_{-\infty}^{\infty} \int_{-\infty}^{\infty} \left[A_y \left(-\frac{K^2 - k_x^2}{\gamma} \hat{x} + \frac{k_y k_x}{\gamma} \hat{y} + j k_x \hat{z} \right) e^{-\gamma z} \right. \\ & \left. + B_y \left(\frac{K^2 - k_x^2}{\gamma} \hat{x} - \frac{k_y k_x}{\gamma} \hat{y} + j k_x \hat{z} \right) e^{\gamma z} \right] e^{j(k_x x + k_y y)} dk_x dk_y \end{aligned} \quad (3.1)$$

Using (2.57) the magnetic field along the x can be found to be:

$$\tilde{H}_x(k_x, k_y, 0) = A_{y1} \frac{j}{\omega\mu_0} \frac{K^2 - k_x^2}{\gamma} (-1 + g_1) \quad (3.2)$$

Where:

$$\begin{aligned} A_{y1} = & \frac{I}{1 + g_1} \\ I = & \frac{1}{4\pi^2} \int_0^b \int_0^a \left[(1 + \Gamma(x, y)) \frac{j\pi\omega\mu}{ak_{c10}^2} \sin\left(\frac{\pi}{a}x\right) e^{-j(k_x x + k_y y)} \right] dx dy \end{aligned}$$

When put together, \tilde{H}_x outside the waveguide is given as:

$$\begin{aligned} \tilde{H}_x(k_x, k_y, 0) = & \\ & \frac{j(K^2 - k_x^2)(-1 + g_1)}{\gamma\omega\mu_0(1 + g_1)4\pi^2} \int_0^b \int_0^a (1 + \Gamma(x, y)) \frac{j\pi\omega\mu}{ak_{c10}^2} \sin\left(\frac{\pi}{a}x\right) e^{-j(k_x x + k_y y)} dx dy \end{aligned} \quad (3.3)$$

The magnetic field inside the waveguide is given by Equation (3.4)

$$\tilde{H}_x(k_x, k_y, 0) = \int_0^b \int_0^a (1 - \Gamma(x, y)) \frac{-j\pi\omega\mu}{ak_{c10}^2} Y_o \sin\left(\frac{\pi}{a}x\right) e^{-j(k_x x + k_y y)} dx dy \quad (3.4)$$

The two fields must match at the aperture of the waveguide producing Equation (3.5)

$$\begin{aligned} \frac{1}{4\pi^2} \int_0^b \int_0^a \left[(1 - \Gamma(x, y)) \frac{-j\pi\omega\mu}{ak_{c10}^2} Y_o \sin\left(\frac{\pi}{a}x\right) e^{-j(k_x x + k_y y)} \right] dx dy = \\ \frac{j(K^2 - k_x^2)(-1 + g_1)}{\gamma\omega\mu_o(1 + g_1)4\pi^2} \int_0^b \int_0^a \left[(1 + \Gamma(x, y)) \frac{j\pi\omega\mu}{ak_{c10}^2} \sin\left(\frac{\pi}{a}x\right) e^{-j(k_x x + k_y y)} \right] dx dy \quad (3.5) \end{aligned}$$

By splitting the integration and moving the terms containing the reflection coefficient to one side we arrive at Equation (3.6):

$$\begin{aligned} \int_0^b \int_0^a \frac{j\pi\omega\mu}{ak_{c10}^2} Y_o \sin\left(\frac{\pi}{a}x\right) e^{-j(k_x x + k_y y)} dx dy = \\ \int_0^b \int_0^a \left[(\Phi(1 + \Gamma(x, y)) + Y_o\Gamma(x, y)) \frac{j\pi\omega\mu}{ak_{c10}^2} \sin\left(\frac{\pi}{a}x\right) e^{-j(k_x x + k_y y)} \right] dx dy \quad (3.6) \end{aligned}$$

Where

$$\Phi = \frac{K^2 - k_x^2 (g_1 - 1)}{j\omega\mu_o\gamma (g_1 + 1)}$$

The above term can be further simplified by moving the terms that does not contain the reflection coefficient to the other side.

$$\frac{\int_0^b \int_0^a (Y_o - \Phi) \sin\left(\frac{\pi}{a}x\right) e^{-j(k_x x + k_y y)} dx dy}{(\Phi + Y_o)} = \int_0^b \int_0^a \Gamma(x, y) \sin\left(\frac{\pi}{a}x\right) e^{-j(k_x x + k_y y)} dx dy$$

With further manipulation the term is simplified further into Equation (3.7)

$$\begin{aligned} \int_0^b \int_0^a \left[\Gamma(x, y) \sin\left(\frac{\pi}{a}x\right) e^{-j(k_x x + k_y y)} \right] dx dy \\ = \frac{\left[Y_o - \frac{1}{j\omega\mu_o} \frac{K^2 - k_x^2 (g_1 - 1)}{\gamma (g_1 + 1)} \right]}{\left[Y_o + \frac{1}{j\omega\mu_o} \frac{K^2 - k_x^2 (g_1 - 1)}{\gamma (g_1 + 1)} \right]} \int_0^b \int_0^a \sin\left(\frac{\pi}{a}x\right) e^{-j(k_x x + k_y y)} dx dy \quad (3.7) \end{aligned}$$

Equation (3.7) has two applications, finding the spatial distribution of $\Gamma(x, y)$ over the waveguide's aperture and finding the effective reflection coefficient Γ_{10} for the dominant mode.

3.1.1 The Spatial Distribution of the Reflection Coefficient $\Gamma(x, y)$

To compute $\Gamma(x, y)$ Equation (3.7) can be manipulated further into (3.8):

$$\Gamma(x, y) = \frac{1}{4\pi^2 \sin\left(\frac{\pi}{a}x\right)} \int_{-\infty}^{\infty} \int_{-\infty}^{\infty} \tilde{\Psi}(k_x, k_y) \tilde{\Lambda}(k_x, k_y) e^{j(k_x x + k_y y)} dk_x dk_y \quad (3.8)$$

Where:

$$\tilde{\Psi}(k_x, k_y) = \frac{\left(Y_o - \frac{1}{j\omega\mu_o} \frac{K^2 - k_x^2}{\gamma_1(k_x, k_y)} (g_1(k_x, k_y) - 1) \right)}{\left(Y_o + \frac{1}{j\omega\mu_o} \frac{K^2 - k_x^2}{\gamma_1(k_x, k_y)} (g_1(k_x, k_y) + 1) \right)}$$

$$\tilde{\Lambda}(k_x, k_y) = \int_0^b \int_0^a \sin\left(\frac{\pi}{a}x\right) e^{-j(k_x x + k_y y)} dx dy = \int_0^b \int_0^a \left(\frac{e^{j\frac{\pi}{a}x} - e^{-j\frac{\pi}{a}x}}{2j} \right) e^{-j(k_x x + k_y y)} dx dy$$

$$\begin{aligned} \tilde{\Lambda}(k_x, k_y) &= \int_0^b \int_0^a \left(\frac{e^{j\left(\frac{\pi}{a}x - jk_x x\right)} - e^{-j\left(\frac{\pi}{a}x + jk_x x\right)}}{2j} \right) e^{-j(k_y y)} dx dy \\ &= \int_0^b \int_0^a \left(\frac{e^{jx\left(\frac{\pi}{a} - k_x\right)} - e^{-jx\left(\frac{\pi}{a} + k_x\right)}}{2j} \right) e^{-j(k_y y)} dx dy \\ &= \int_0^b \int_0^a \left(\frac{e^{jx\left(\frac{\pi}{a} - k_x\right)}}{2j} \right) e^{-j(k_y y)} dx dy - \int_0^b \int_0^a \left(\frac{e^{-jx\left(\frac{\pi}{a} + k_x\right)}}{2j} \right) e^{-j(k_y y)} dx dy \\ &= \frac{1}{2j} \int_0^b e^{-j(k_y y)} dy \left[\int_0^a e^{jx\left(\frac{\pi}{a} - k_x\right)} dx - \int_0^a e^{-jx\left(\frac{\pi}{a} + k_x\right)} dx \right] \end{aligned}$$

$$\begin{aligned} \tilde{\Lambda}(k_x, k_y) &= \frac{1}{2j} b e^{j\frac{-k_y b}{2}} \operatorname{sinc}\left(\frac{-k_y b}{2\pi}\right) \left[a e^{j\frac{(\pi - ak_x)}{2}} \operatorname{sinc}\left(\frac{(\pi - ak_x)}{2\pi}\right) \right. \\ &\quad \left. - a e^{-j\frac{(\pi + ak_x)}{2}} \operatorname{sinc}\left(\frac{(\pi + ak_x)}{2\pi}\right) \right] \end{aligned}$$

$$\operatorname{sinc}(x) = \begin{cases} \frac{\sin(\pi x)}{\pi x} & x \neq 0 \\ 1 & x = 0 \end{cases}$$

The spatial distribution of Γ is valid only over the aperture of the waveguide and has two singularity axes at $x = 0$ and $x = b$ since the electric field approaches zero at these edges of the waveguide. The closed form expression of Γ might prove too difficult to be written explicitly for $N \gg 1$. Hence, the evaluation of the function is best suited to be done numerically. In order to implement Equation (3.8) its form has to be optimized for a computationally efficient evaluation. Fast Fourier Transform (FFT) is used as a very efficient algorithm to implement Discrete Fourier Transform (DFT). Two dimensional FFT can replace its continuous equivalent of Fourier transform in Equation (3.8) by variable substitution resulting in Equation (3.9):

$$\begin{aligned} & \Gamma \left(C \frac{\pi}{L_x}, D \frac{\pi}{L_y} \right) \\ &= \frac{\Delta k_x \cdot \Delta k_y \cdot L_x \cdot L_x}{4\pi^2 \sin \left(\frac{\pi}{a} C \frac{\pi}{L_x} \right)} \sum_{u=0}^{L_x-1} \sum_{v=0}^{L_y-1} \tilde{\Psi}(u\Delta k_x, v\Delta k_y) \tilde{\Lambda}(u\Delta k_x, v\Delta k_y) e^{j2\pi \left(\frac{u}{L_x} C + \frac{v}{L_y} D \right)} \end{aligned} \quad (3.9)$$

Where Δk_x and Δk_y are the sample spacing in the frequency domain, L_x and L_y are the number of steps in dimensions k_x and k_y , respectively, and C and D are integers representing the discretized spatial variables x and y .

The proper values for Δk_x and Δk_y are dependent on the number of values we want to evaluate and the size of the mesh in the spatial domain (x, y) . This issue will be discussed in detail in the simulation chapter since the reason why these values cannot be chosen randomly can be best explained by an example.

3.1.2 The Effective Value of the Reflection Coefficient Γ

The previous subsection provided a formula to evaluate the distribution of the reflection coefficient over the waveguide's aperture. How much of the signal does reach the receiver? To answer this question we need to go back to the concepts explained in the background chapter. Only certain modes can propagate within the waveguide under a certain operating frequency. Since the assumptions stated that the frequency of operation guarantees the elimination of higher modes within the waveguide, then what returns from the aperture is the portion of the signal carried over the dominant mode TE_{10} . The nature of wave propagation within the waveguide dictates that discrete and infinite numbers of modes might exist within the waveguide

and these modes are orthogonal. The orthogonality principle provides the following property Equation (3.10).

$$\int_0^1 e^{jm2\pi x} e^{-jn2\pi x} dx = \begin{cases} 1 & m = n \\ 0 & m \neq n \end{cases} \quad (3.10)$$

Using this property allows us to isolate the magnitude of the reflection coefficient related to a specific propagation mode. To illustrate assume the signal reflected is written in a multimodal expression as shown in Equation (3.11).

$$\Gamma(x, y) \sin\left(\frac{\pi}{a}x\right) = E_y^r = \sum_{m=0}^{\infty} \sum_{n=0}^{\infty} \Gamma_{mn} \sin\left(\frac{m\pi}{a}x\right) \cos\left(\frac{n\pi}{b}y\right) \quad (3.11)$$

Where the superscript r refers to the reflected electric field and the subscript y is the direction in which the vector is pointing. To extract the reflection coefficient we multiply by the normalized basis function for TE_{10} and integrate over the aperture.

$$\begin{aligned} \Gamma_{10} &= \frac{2}{ab} \int_0^b \int_0^a E_y^r \sin\left(\frac{\pi}{a}x\right) dx dy = \frac{2}{ab} \int_0^b \int_0^a \sum_{m=0}^{\infty} \sum_{n=0}^{\infty} \Gamma_{mn} \sin\left(\frac{m\pi}{a}x\right) \cos\left(\frac{n\pi}{b}y\right) \sin\left(\frac{\pi}{a}x\right) dx dy \\ \Gamma_{10} &= \frac{\int_0^b \int_0^a [\Gamma(x, y) \sin^2\left(\frac{\pi}{a}x\right)] dx dy}{\int_0^b \int_0^a \sin^2\left(\frac{\pi}{a}x\right) dx dy} \end{aligned} \quad (3.12)$$

The normalized admittance of the waveguide's aperture is related to the reflection coefficient by Equation (3.13).

$$Y_{norm} = \frac{Y_{aperture}}{Y_{10}} = \frac{G}{Y_{10}} + j \frac{B}{Y_{10}} = \frac{1 - \Gamma_{10}}{1 + \Gamma_{10}} \quad (3.13)$$

Equation (3.12) requires the evaluation of Equation (3.9) which in turn becomes computationally intensive when evaluated for many frequencies. When dealing with the inverse problem for such a high dimensionality i.e. many variables, the problem of time becomes a major concern especially when employing an exhaustive search algorithm. For example, since a direct relation between the reflection coefficient and the structure's parameters is not clear, then an iterative technique might require many evaluations for the forward problem until a matching output is reached. An approximation can be made to accelerate the process. If we assumed that the higher modes have negligible contribution and the reflection

coefficient is almost flat over the aperture, then Equation (3.7) can be evaluated at $k_x = k_y = 0$ for the normalized value of Γ .

$$\frac{\int_0^b \int_0^a \left[\Gamma(x, y) \sin\left(\frac{\pi}{a}x\right)^2 \right] dx dy}{\int_0^b \int_0^a \sin\left(\frac{\pi}{a}x\right)^2 dx dy} \approx \frac{\int_0^b \int_0^a \left[\Gamma(x, y) \sin\left(\frac{\pi}{a}x\right) \right] dx dy}{\int_0^b \int_0^a \sin\left(\frac{\pi}{a}x\right) dx dy}$$

Given that:

$$\frac{\int_0^b \int_0^a \left[\Gamma(x, y) \sin\left(\frac{\pi}{a}x\right) \right] dx dy}{\int_0^b \int_0^a \sin\left(\frac{\pi}{a}x\right) dx dy} = \left. \frac{\left(Y_o - \frac{1}{j\omega\mu_o} \frac{K^2 - k_x^2}{\gamma_1} \frac{(g_1 - 1)}{(g_1 + 1)} \right)}{\left(Y_o + \frac{1}{j\omega\mu_o} \frac{K^2 - k_x^2}{\gamma_1} \frac{(g_1 - 1)}{(g_1 + 1)} \right)} \right|_{(k_x, k_y) \rightarrow (0, 0)} \quad (3.14)$$

Equation (3.14) evaluates the reflection coefficient as in the far field and introduces an error that is a function of the dielectric facing the waveguide and the range of the furthest interface. The advantage of (3.14) is speed. Single point substitution gives a very fast response time to be used in inverse problems at the cost of inaccuracy. The inaccuracy issue will be discussed in the simulation chapter where the final decision about using Equation (3.14) will be made.

3.2 Multimode General Solution

To appreciate the complexity of multimode solutions compared to the one derived in this thesis; the multimode general solution will be attempted analytically but will not be implemented. Moreover, it should be kept in mind that this derivation is for a single layer of IHS of a dielectric. So far I have no knowledge of any reference that attempted multilayer multimode analytical solution but it is achievable and such a solution is possible to exist in today's literature.

The electromagnetic field inside the waveguide can be written as an infinite Fourier series of the hertzian fields. That includes all possible propagation modes Equations (3.15) and (3.16).

$$H_{z_{wg}}(x, y, z) = \sum_{m=-\infty}^{\infty} \sum_{n=-\infty}^{\infty} \tilde{H}_{z_{wg}}(m, n, z) e^{j\left(\frac{m\pi}{a}x + \frac{n\pi}{b}y\right)} \quad (3.15)$$

$$E_{z_{wg}}(x, y, z) = \sum_{m=-\infty}^{\infty} \sum_{n=-\infty}^{\infty} \tilde{E}_{z_{wg}}(m, n, z) e^{j\left(\frac{m\pi}{a}x + \frac{n\pi}{b}y\right)} \quad (3.16)$$

Where the subscript wg refers to the field inside the waveguide, the subscript z refers to the hertzian field in the z direction, the tilde notation means the field coefficient in the frequency domain and m and n are the harmonic frequency at which that coefficient exists.

The hertzian modes can be written in terms of the incident and reflected wave as shown in Equations

$$H_{z_{wg}}(x, y, z) = \sum_{m=-\infty}^{\infty} \sum_{n=-\infty}^{\infty} \left(A_{z_{wg}}^h(m, n)e^{-\gamma z} + B_{z_{wg}}^h(m, n)e^{\gamma z} \right) e^{j\left(\frac{m\pi}{a}x + \frac{n\pi}{b}y\right)} \quad (3.17)$$

$$E_{z_{wg}}(x, y, z) = \sum_{m=-\infty}^{\infty} \sum_{n=-\infty}^{\infty} \left(A_{z_{wg}}^e(m, n)e^{-\gamma z} + B_{z_{wg}}^e(m, n)e^{\gamma z} \right) e^{j\left(\frac{m\pi}{a}x + \frac{n\pi}{b}y\right)} \quad (3.18)$$

As given in Table 2.3 any incident i.e. in the direction of $+z$, TE mode is given by Equations (3.19) to (3.23).

$$H_z^i(x, y, z) = A_{z_{wg}}^h(m, n) \cos\left(\frac{m\pi}{a}x\right) \cos\left(\frac{n\pi}{b}y\right) e^{-j\beta z} \quad (3.19)$$

$$E_{x_{mn}}^i(x, y, z) = \frac{j\omega\mu n\pi}{k_{mn}^2 b} A_{z_{wg}}^h(m, n) \cos\left(\frac{m\pi}{a}x\right) \sin\left(\frac{n\pi}{b}y\right) e^{-j\beta z} \quad (3.20)$$

$$E_{y_{mn}}^i(x, y, z) = \frac{-j\omega\mu m\pi}{k_{mn}^2 a} A_{z_{wg}}^h(m, n) \sin\left(\frac{m\pi}{a}x\right) \cos\left(\frac{n\pi}{b}y\right) e^{-j\beta z} \quad (3.21)$$

$$H_{x_{mn}}^i(x, y, z) = \frac{j\beta m\pi}{k_{mn}^2 a} A_{z_{wg}}^h(m, n) \sin\left(\frac{m\pi}{a}x\right) \cos\left(\frac{n\pi}{b}y\right) e^{-j\beta z} \quad (3.22)$$

$$H_{y_{mn}}^i(x, y, z) = \frac{j\beta n\pi}{k_{mn}^2 b} A_{z_{wg}}^h(m, n) \cos\left(\frac{m\pi}{a}x\right) \sin\left(\frac{n\pi}{b}y\right) e^{-j\beta z} \quad (3.23)$$

Where the superscript i means incident, the subscripts x and y refer to the spatial dimension at which the vector is pointing and the subscripts m and n refer to the mode number i.e. the harmonic frequency value.

Similarly any incident TM mode inside a rectangular waveguide is given by Equations (3.24) to (3.28).

$$E_z^i(x, y, z) = A_{z_{wg}}^e(m, n) \sin\left(\frac{m\pi}{a}x\right) \sin\left(\frac{n\pi}{b}y\right) e^{-j\beta z} \quad (3.24)$$

$$E_{x_{mn}}^i(x, y, z) = \frac{-j\beta m\pi}{k_{mn}^2 a} A_{z_{wg}}^e(m, n) \cos\left(\frac{m\pi}{a}x\right) \sin\left(\frac{n\pi}{b}y\right) e^{-j\beta z} \quad (3.25)$$

$$E_{y_{mn}}^i(x, y, z) = \frac{-j\beta n\pi}{k_{mn}^2 b} A_{z_{wg}}^e(m, n) \sin\left(\frac{m\pi}{a}x\right) \cos\left(\frac{n\pi}{b}y\right) e^{-j\beta z} \quad (3.26)$$

$$H_{xmn}^i(x, y, z) = \frac{j\omega\varepsilon n\pi}{k_{mn}^2 b} A_{z_{wg}}^e(m, n) \sin\left(\frac{m\pi}{a}x\right) \cos\left(\frac{n\pi}{b}y\right) e^{-j\beta z} \quad (3.27)$$

$$\begin{aligned} H_{y_{mn}}^i(x, y, z) \\ = \frac{-j\omega\varepsilon m\pi}{k_{mn}^2 a} A_{z_{wg}}^e(m, n) \cos\left(\frac{m\pi}{a}x\right) \sin\left(\frac{n\pi}{b}y\right) e^{-j\beta z} \end{aligned} \quad (3.28)$$

The return TE and TM modes propagate in the negative z direction and have the superscript r . They will have slightly different equations which are given by Equations (3.29) to (3.33) for TE modes and Equations (3.34) to (3.38) for TM modes.

TE Modes:

$$H_z^r(x, y, z) = B_{z_{wg}}^h(m, n) \cos\left(\frac{m\pi}{a}x\right) \cos\left(\frac{n\pi}{b}y\right) e^{j\beta z} \quad (3.29)$$

$$E_{x_{mn}}^r(x, y, z) = \frac{j\omega\mu n\pi}{k_{mn}^2 b} B_{z_{wg}}^h(m, n) \cos\left(\frac{m\pi}{a}x\right) \sin\left(\frac{n\pi}{b}y\right) e^{j\beta z} \quad (3.30)$$

$$E_{y_{mn}}^r(x, y, z) = \frac{-j\omega\mu m\pi}{k_{mn}^2 a} B_{z_{wg}}^h(m, n) \sin\left(\frac{m\pi}{a}x\right) \cos\left(\frac{n\pi}{b}y\right) e^{j\beta z} \quad (3.31)$$

$$H_{x_{mn}}^r(x, y, z) = -\frac{j\beta m\pi}{k_{mn}^2 a} B_{z_{wg}}^h(m, n) \sin\left(\frac{m\pi}{a}x\right) \cos\left(\frac{n\pi}{b}y\right) e^{j\beta z} \quad (3.32)$$

$$H_{y_{mn}}^r(x, y, z) = -\frac{j\beta n\pi}{k_{mn}^2 b} B_{z_{wg}}^h(m, n) \cos\left(\frac{m\pi}{a}x\right) \sin\left(\frac{n\pi}{b}y\right) e^{j\beta z} \quad (3.33)$$

TM Modes:

$$E_z^r(x, y, z) = B_{z_{wg}}^e(m, n) \sin\left(\frac{m\pi}{a}x\right) \sin\left(\frac{n\pi}{b}y\right) e^{j\beta z} \quad (3.34)$$

$$E_{x_{mn}}^r(x, y, z) = \frac{j\beta m\pi}{k_{mn}^2 a} B_{z_{wg}}^e(m, n) \cos\left(\frac{m\pi}{a}x\right) \sin\left(\frac{n\pi}{b}y\right) e^{j\beta z} \quad (3.35)$$

$$E_{y_{mn}}^r(x, y, z) = \frac{j\beta n\pi}{k_{mn}^2 b} B_{z_{wg}}^e(m, n) \sin\left(\frac{m\pi}{a}x\right) \cos\left(\frac{n\pi}{b}y\right) e^{j\beta z} \quad (3.36)$$

$$H_{x_{mn}}^r(x, y, z) = \frac{j\omega\varepsilon n\pi}{k_{mn}^2 b} B_{z_{wg}}^e(m, n) \sin\left(\frac{m\pi}{a}x\right) \cos\left(\frac{n\pi}{b}y\right) e^{j\beta z} \quad (3.37)$$

$$H_{y_{mn}}^r(x, y, z) = \frac{j\omega\varepsilon m\pi}{-k_{mn}^2 a} B_{z_{wg}}^e(m, n) \cos\left(\frac{m\pi}{a}x\right) \sin\left(\frac{n\pi}{b}y\right) e^{j\beta z} \quad (3.38)$$

The fields outside the waveguide can be written in terms of its hertzian modes which are shown in Equations (3.39) and (3.40).

$$H_{z_1}(x, y, z) = \int_{-\infty}^{\infty} \int_{-\infty}^{\infty} (A_{z_1}^h(\zeta_x, \zeta_y)e^{-\psi z} + B_{z_1}^h(\zeta_x, \zeta_y)e^{\psi z}) e^{j(\zeta_x x + \zeta_y y)} d\zeta_x d\zeta_y \quad (3.39)$$

$$E_{z_1}(x, y, z) = \int_{-\infty}^{\infty} \int_{-\infty}^{\infty} (A_{z_1}^e(\zeta_x, \zeta_y)e^{-\psi z} + B_{z_1}^e(\zeta_x, \zeta_y)e^{\psi z}) e^{j(\zeta_x x + \zeta_y y)} d\zeta_x d\zeta_y \quad (3.40)$$

Using Equations (2.30) to (2.33) we can write the transverse field components as shown in Equations (3.41) to (3.44)

$$\tilde{E}_{x_1}(\zeta_x, \zeta_y, 0) = C_c \zeta_x (A_{z_1}^e(\zeta_x, \zeta_y) - B_{z_1}^e(\zeta_x, \zeta_y)) + C_d \mu_1 \zeta_y (A_{z_1}^h(\zeta_x, \zeta_y) + B_{z_1}^h(\zeta_x, \zeta_y)) \quad (3.41)$$

$$\tilde{E}_{y_1}(\zeta_x, \zeta_y, 0) = C_c \zeta_y (A_{z_1}^e(\zeta_x, \zeta_y) - B_{z_1}^e(\zeta_x, \zeta_y)) - C_d \mu_1 \zeta_x (A_{z_1}^h(\zeta_x, \zeta_y) + B_{z_1}^h(\zeta_x, \zeta_y)) \quad (3.42)$$

$$\tilde{H}_{x_1}(\zeta_x, \zeta_y, 0) = -C_d \varepsilon_1 \zeta_y (A_{z_1}^e(\zeta_x, \zeta_y) + B_{z_1}^e(\zeta_x, \zeta_y)) + C_c \zeta_x (A_{z_1}^h(\zeta_x, \zeta_y) - B_{z_1}^h(\zeta_x, \zeta_y)) \quad (3.43)$$

$$\tilde{H}_{y_1}(\zeta_x, \zeta_y, 0) = C_d \varepsilon_1 \zeta_x (A_{z_1}^e(\zeta_x, \zeta_y) + B_{z_1}^e(\zeta_x, \zeta_y)) + C_c \zeta_y (A_{z_1}^h(\zeta_x, \zeta_y) - B_{z_1}^h(\zeta_x, \zeta_y)) \quad (3.44)$$

Where:

$$C_c = -\frac{j\psi}{k_L^2}, \quad C_d = \frac{\omega}{k_L^2}, \quad k_L^2 = \zeta_x^2 + \zeta_y^2$$

$$\psi = \sqrt{\zeta_x^2 + \zeta_y^2 - K^2}$$

$K = \omega\sqrt{\mu\varepsilon}$ is the wave number

Considering a single layer, the terms which imply the existence of a signal propagating in the negative z direction will be nullified hence the previous set of equations is simplified into Equations (3.45) to (3.48).

$$\tilde{E}_{x_1}(\zeta_x, \zeta_y, 0) = C_c \zeta_x A_{z_1}^e(\zeta_x, \zeta_y) + C_d \mu_1 \zeta_y A_{z_1}^h(\zeta_x, \zeta_y) \quad (3.45)$$

$$\tilde{E}_{y_1}(\zeta_x, \zeta_y, 0) = C_c \zeta_y A_{z_1}^e(\zeta_x, \zeta_y) - C_d \mu_1 \zeta_x A_{z_1}^h(\zeta_x, \zeta_y) \quad (3.46)$$

$$\tilde{H}_{x_1}(\zeta_x, \zeta_y, 0) = -C_d \varepsilon_1 \zeta_y A_{z_1}^e(\zeta_x, \zeta_y) + C_c \zeta_x A_{z_1}^h(\zeta_x, \zeta_y) \quad (3.47)$$

$$\tilde{H}_{y_1}(\zeta_x, \zeta_y, 0) = C_d \varepsilon_1 \zeta_x A_{z_1}^e(\zeta_x, \zeta_y) + C_c \zeta_y A_{z_1}^h(\zeta_x, \zeta_y) \quad (3.48)$$

We will assume dominant mode excitation i.e. TE_{10} , which means only $A_{z_{wg}}^h(1,0) = 1$ exists as an incident mode. Then by equating the transverse

components at both sides of the waveguide's aperture $z = 0$, we obtain an infinite set of linear equations. If we truncate the modes that are higher than $TE_{\alpha\alpha}$ and $TM_{\alpha\alpha}$ where α is a predefined number depending on the required accuracy of the result, we obtain the following equations:

$$\begin{aligned} \sum_{m=0}^{\alpha} \sum_{n=0}^{\alpha} \left(\frac{j\beta m\pi}{k_{mn}^2 a} B_{z\text{wg}}^e(m, n) + \frac{j\omega\mu n\pi}{k_{mn}^2 b} B_{z\text{wg}}^h(m, n) \right) \cos\left(\frac{m\pi}{a}x\right) \sin\left(\frac{n\pi}{b}y\right) \\ = \int_{-\infty}^{\infty} \int_{-\infty}^{\infty} \left(C_c \zeta_x A_{z_1}^e(\zeta_x, \zeta_y) + C_d \mu_1 \zeta_y A_{z_1}^h(\zeta_x, \zeta_y) \right) e^{j(\zeta_x x + \zeta_y y)} d\zeta_x d\zeta_y \end{aligned} \quad (3.49)$$

$$\begin{aligned} \sum_{m=0}^{\alpha} \sum_{n=0}^{\alpha} \left(\frac{j\beta n\pi}{k_{mn}^2 b} B_{z\text{wg}}^e(m, n) - \frac{j\omega\mu m\pi}{k_{mn}^2 a} \left(\delta(1,0) + B_{z\text{wg}}^h(m, n) \right) \right) \sin\left(\frac{m\pi}{a}x\right) \cos\left(\frac{n\pi}{b}y\right) \\ = \int_{-\infty}^{\infty} \int_{-\infty}^{\infty} \left(C_c \zeta_y A_{z_1}^e(\zeta_x, \zeta_y) - C_d \mu_1 \zeta_x A_{z_1}^h(\zeta_x, \zeta_y) \right) e^{j(\zeta_x x + \zeta_y y)} d\zeta_x d\zeta_y \end{aligned} \quad (3.50)$$

$$\begin{aligned} \sum_{m=0}^{\alpha} \sum_{n=0}^{\alpha} \left(\frac{j\omega\varepsilon n\pi}{k_{mn}^2 b} B_{z\text{wg}}^e(m, n) - \frac{j\beta m\pi}{k_{mn}^2 a} \left(-\delta(1,0) + B_{z\text{wg}}^h(m, n) \right) \right) \sin\left(\frac{m\pi}{a}x\right) \cos\left(\frac{n\pi}{b}y\right) \\ = \int_{-\infty}^{\infty} \int_{-\infty}^{\infty} \left(-C_d \varepsilon_1 \zeta_y A_{z_1}^e(\zeta_x, \zeta_y) + C_c \zeta_x A_{z_1}^h(\zeta_x, \zeta_y) \right) e^{j(\zeta_x x + \zeta_y y)} d\zeta_x d\zeta_y \end{aligned} \quad (3.51)$$

$$\begin{aligned} \sum_{m=0}^{\alpha} \sum_{n=0}^{\alpha} \left(\frac{-j\omega\varepsilon m\pi}{k_{mn}^2 a} B_{z\text{wg}}^e(m, n) - \frac{j\beta n\pi}{k_{mn}^2 b} B_{z\text{wg}}^h(m, n) \right) \cos\left(\frac{m\pi}{a}x\right) \sin\left(\frac{n\pi}{b}y\right) \\ = \int_{-\infty}^{\infty} \int_{-\infty}^{\infty} \left(C_d \varepsilon_1 \zeta_x A_{z_1}^e(\zeta_x, \zeta_y) + C_c \zeta_y A_{z_1}^h(\zeta_x, \zeta_y) \right) e^{j(\zeta_x x + \zeta_y y)} d\zeta_x d\zeta_y \end{aligned} \quad (3.52)$$

Using the orthogonality principle defined by Equation (3.10) we can arrive at the relation between each mode with the field outside the waveguide as shown in Equations

$$\begin{aligned} \left(\frac{j\beta m\pi}{k_{mn}^2 a} B_{z\text{wg}}^e(m, n) + \frac{j\omega\mu n\pi}{k_{mn}^2 b} B_{z\text{wg}}^h(m, n) \right) \\ = \int_{-\infty}^{\infty} \int_{-\infty}^{\infty} \left(C_c \zeta_x A_{z_1}^e(\zeta_x, \zeta_y) + C_d \mu_1 \zeta_y A_{z_1}^h(\zeta_x, \zeta_y) \right) P d\zeta_x d\zeta_y \end{aligned} \quad (3.53)$$

$$\begin{aligned} \left(\frac{j\beta n\pi}{k_{mn}^2 b} B_{z\text{wg}}^e(m, n) - \frac{j\omega\mu m\pi}{k_{mn}^2 a} \left(\delta(1,0) + B_{z\text{wg}}^h(m, n) \right) \right) \\ = \int_{-\infty}^{\infty} \int_{-\infty}^{\infty} \left(C_c \zeta_y A_{z_1}^e(\zeta_x, \zeta_y) - C_d \mu_1 \zeta_x A_{z_1}^h(\zeta_x, \zeta_y) \right) S d\zeta_x d\zeta_y \end{aligned} \quad (3.54)$$

$$\left(\frac{j\omega\varepsilon n\pi}{k_{mn}^2 b} B_{z\,wg}^e(m, n) - \frac{j\beta m\pi}{k_{mn}^2 a} \left(B_{z\,wg}^h(m, n) - \delta(1,0) \right) \right) \quad (3.55)$$

$$= \int_{-\infty}^{\infty} \int_{-\infty}^{\infty} \left(-C_d \varepsilon_1 \zeta_y A_{z_1}^e(\zeta_x, \zeta_y) + C_c \zeta_x A_{z_1}^h(\zeta_x, \zeta_y) \right) S d\zeta_x d\zeta_y$$

$$\left(\frac{-j\omega\varepsilon m\pi}{k_{mn}^2 a} B_{z\,wg}^e(m, n) - \frac{j\beta n\pi}{k_{mn}^2 b} B_{z\,wg}^h(m, n) \right) \quad (3.56)$$

$$= \int_{-\infty}^{\infty} \int_{-\infty}^{\infty} \left(C_d \varepsilon_1 \zeta_x A_{z_1}^e(\zeta_x, \zeta_y) + C_c \zeta_y A_{z_1}^h(\zeta_x, \zeta_y) \right) P d\zeta_x d\zeta_y$$

Where P and S are given by Equations (3.57) and (3.58)

$$P(m, n, \zeta_x, \zeta_y) = \frac{1}{C} \int_0^b \int_0^a \cos\left(\frac{m\pi}{a} x\right) \sin\left(\frac{n\pi}{b} y\right) e^{j(\zeta_x x + \zeta_y y)} dx dy \quad (3.57)$$

$$S(m, n, \zeta_x, \zeta_y) = \frac{1}{C} \int_0^b \int_0^a \sin\left(\frac{m\pi}{a} x\right) \cos\left(\frac{n\pi}{b} y\right) e^{j(\zeta_x x + \zeta_y y)} dx dy \quad (3.58)$$

Where C is the integration constant given by:

$$C = \begin{cases} \frac{4}{ab} & mn \neq 0 \\ \frac{2}{ab} & mn = 0 \end{cases}$$

In a similar manner we can isolate the (ζ_x, ζ_y) harmonic field outside the waveguide aperture by multiplying it by the basis functions and integrating over the aperture obtaining Equations (3.59) to (3.62).

$$\sum_{m=0}^{\alpha} \sum_{n=0}^{\alpha} \left(\frac{j\beta m\pi}{k_{mn}^2 a} B_{z\,wg}^e(m, n) + \frac{j\omega\mu n\pi}{k_{mn}^2 b} B_{z\,wg}^h(m, n) \right) Q \quad (3.59)$$

$$= \left(C_c \zeta_x A_{z_1}^e(\zeta_x, \zeta_y) + C_d \mu_1 \zeta_y A_{z_1}^h(\zeta_x, \zeta_y) \right)$$

$$\sum_{m=0}^{\alpha} \sum_{n=0}^{\alpha} \left(\frac{j\beta n\pi}{k_{mn}^2 b} B_{z\,wg}^e(m, n) - \frac{j\omega\mu m\pi}{k_{mn}^2 a} \left(\delta(1,0) + B_{z\,wg}^h(m, n) \right) \right) W \quad (3.60)$$

$$= \left(C_c \zeta_y A_{z_1}^e(\zeta_x, \zeta_y) - C_d \mu_1 \zeta_x A_{z_1}^h(\zeta_x, \zeta_y) \right)$$

$$\sum_{m=0}^{\alpha} \sum_{n=0}^{\alpha} \left(\frac{j\omega\varepsilon n\pi}{k_{mn}^2 b} B_{z\,wg}^e(m, n) - \frac{j\beta m\pi}{k_{mn}^2 a} (B_{z\,wg}^h(m, n) - \delta(1,0)) \right) W \quad (3.61)$$

$$= (-C_d \varepsilon_1 \zeta_y A_{z_1}^e(\zeta_x, \zeta_y) + C_c \zeta_x A_{z_1}^h(\zeta_x, \zeta_y))$$

$$\sum_{m=0}^{\alpha} \sum_{n=0}^{\alpha} \left(\frac{-j\omega\varepsilon m\pi}{k_{mn}^2 a} B_{z\,wg}^e(m, n) - \frac{j\beta n\pi}{k_{mn}^2 b} B_{z\,wg}^h(m, n) \right) Q \quad (3.62)$$

$$= (C_d \varepsilon_1 \zeta_x A_{z_1}^e(\zeta_x, \zeta_y) + C_c \zeta_y A_{z_1}^h(\zeta_x, \zeta_y))$$

Where Q and W are given by Equations (3.63) and (3.64)

$$Q(m, n, \zeta_x, \zeta_y) = \frac{1}{4\pi^2} \int_0^b \int_0^a \cos\left(\frac{m\pi}{a}x\right) \sin\left(\frac{n\pi}{b}y\right) e^{-j(\zeta_x x + \zeta_y y)} dx dy \quad (3.63)$$

$$W(m, n, \zeta_x, \zeta_y) = \frac{1}{4\pi^2} \int_0^b \int_0^a \sin\left(\frac{m\pi}{a}x\right) \cos\left(\frac{n\pi}{b}y\right) e^{-j(\zeta_x x + \zeta_y y)} dx dy \quad (3.64)$$

By substituting Equations (3.59) to (3.62) back into Equations (3.53) to (3.56) we obtain the following relations.

$$\left(\frac{j\beta m\pi}{k_{mn}^2 a} B_{z\,wg}^e(m, n) + \frac{j\omega\mu n\pi}{k_{mn}^2 b} B_{z\,wg}^h(m, n) \right) = \int_{-\infty}^{\infty} \int_{-\infty}^{\infty} \sum_{m=0}^{\alpha} \sum_{n=0}^{\alpha} \left(\frac{j\beta m\pi}{k_{mn}^2 a} B_{z\,wg}^e(m, n) + \frac{j\omega\mu n\pi}{k_{mn}^2 b} B_{z\,wg}^h(m, n) \right) Q Pd\zeta_x d\zeta_y \quad (3.65)$$

$$\left(\frac{j\beta n\pi}{k_{mn}^2 b} B_{z\,wg}^e(m, n) - \frac{j\omega\mu m\pi}{k_{mn}^2 a} (\delta(1,0) + B_{z\,wg}^h(m, n)) \right) = \int_{-\infty}^{\infty} \int_{-\infty}^{\infty} \sum_{m=0}^{\alpha} \sum_{n=0}^{\alpha} \left(\frac{j\beta n\pi}{k_{mn}^2 b} B_{z\,wg}^e(m, n) - \frac{j\omega\mu m\pi}{k_{mn}^2 a} (\delta(1,0) + B_{z\,wg}^h(m, n)) \right) W Sd\zeta_x d\zeta_y \quad (3.66)$$

$$\left(\frac{j\omega\varepsilon n\pi}{k_{mn}^2 b} B_{z\,wg}^e(m, n) - \frac{j\beta m\pi}{k_{mn}^2 a} (B_{z\,wg}^h(m, n) - \delta(1,0)) \right) = \int_{-\infty}^{\infty} \int_{-\infty}^{\infty} \sum_{m=0}^{\alpha} \sum_{n=0}^{\alpha} \left(\frac{j\omega\varepsilon n\pi}{k_{mn}^2 b} B_{z\,wg}^e(m, n) - \frac{j\beta m\pi}{k_{mn}^2 a} (B_{z\,wg}^h(m, n) - \delta(1,0)) \right) W Sd\zeta_x d\zeta_y \quad (3.67)$$

$$\left(\frac{-j\omega\varepsilon m\pi}{k_{mn}^2 a} B_{z\,wg}^e(m, n) - \frac{j\beta n\pi}{k_{mn}^2 b} B_{z\,wg}^h(m, n) \right) = \int_{-\infty}^{\infty} \int_{-\infty}^{\infty} \sum_{m=0}^{\alpha} \sum_{n=0}^{\alpha} \left(\frac{-j\omega\varepsilon m\pi}{k_{mn}^2 a} B_{z\,wg}^e(m, n) - \frac{j\beta n\pi}{k_{mn}^2 b} B_{z\,wg}^h(m, n) \right) Q Pd\zeta_x d\zeta_y \quad (3.68)$$

Equations (3.65) through (3.68) can be rewritten in an equivalent form as:

$$\left(\frac{j\beta m\pi}{k_{mn}^2 a} B_{z\,wg}^e(m, n) + \frac{j\omega\mu n\pi}{k_{mn}^2 b} B_{z\,wg}^h(m, n) \right) = \sum_{m=0}^{\alpha} \sum_{n=0}^{\alpha} \left(\frac{j\beta m\pi}{k_{mn}^2 a} B_{z\,wg}^e(m, n) + \frac{j\omega\mu n\pi}{k_{mn}^2 b} B_{z\,wg}^h(m, n) \right) \int_{-\infty}^{\infty} \int_{-\infty}^{\infty} QP d\zeta_x d\zeta_y \quad (3.69)$$

$$\left(\frac{j\beta n\pi}{k_{mn}^2 b} B_{z\,wg}^e(m, n) - \frac{j\omega\mu m\pi}{k_{mn}^2 a} (\delta(1,0) + B_{z\,wg}^h(m, n)) \right) = \sum_{m=0}^{\alpha} \sum_{n=0}^{\alpha} \left(\frac{j\beta n\pi}{k_{mn}^2 b} B_{z\,wg}^e(m, n) - \frac{j\omega\mu m\pi}{k_{mn}^2 a} (\delta(1,0) + B_{z\,wg}^h(m, n)) \right) \int_{-\infty}^{\infty} \int_{-\infty}^{\infty} WS d\zeta_x d\zeta_y \quad (3.70)$$

$$\left(\frac{j\omega\varepsilon n\pi}{k_{mn}^2 b} B_{z\,wg}^e(m, n) - \frac{j\beta m\pi}{k_{mn}^2 a} (B_{z\,wg}^h(m, n) - \delta(1,0)) \right) = \sum_{m=0}^{\alpha} \sum_{n=0}^{\alpha} \left(\frac{j\omega\varepsilon n\pi}{k_{mn}^2 b} B_{z\,wg}^e(m, n) - \frac{j\beta m\pi}{k_{mn}^2 a} (B_{z\,wg}^h(m, n) - \delta(1,0)) \right) \int_{-\infty}^{\infty} \int_{-\infty}^{\infty} WS d\zeta_x d\zeta_y \quad (3.71)$$

$$\left(\frac{-j\omega\varepsilon m\pi}{k_{mn}^2 a} B_{z\,wg}^e(m, n) - \frac{j\beta n\pi}{k_{mn}^2 b} B_{z\,wg}^h(m, n) \right) = \sum_{m=0}^{\alpha} \sum_{n=0}^{\alpha} \left(\frac{-j\omega\varepsilon m\pi}{k_{mn}^2 a} B_{z\,wg}^e(m, n) - \frac{j\beta n\pi}{k_{mn}^2 b} B_{z\,wg}^h(m, n) \right) \int_{-\infty}^{\infty} \int_{-\infty}^{\infty} QP d\zeta_x d\zeta_y \quad (3.72)$$

The final set of linear equations can be found by either substituting Equations (3.59) through (3.62) back into Equations (3.49) to (3.52) or a simpler approach can be attained by using Equations (3.69) through (3.72) to obtain a finite set of independent equations by varying the variables m, n until we have the complete set of independent equations.

A matrix solution is possible after the evaluation of the continuous integrals which require further mathematical manipulation. No further derivation will be done on the integrals since these equations are not going to be implemented in this thesis. They are merely to show the usual methodology taken in multimode solutions since results from other authors which are obtained using multimode solutions will be compared to the results of this thesis.

CHAPTER 4

RESULTS ANALYSIS AND SIMULATION

The first section of this chapter includes the simulation and commented results of the mathematical derivations chapter. The algorithms for computing the reflection coefficient will be applied and commented on. The sources of error in computation will be reasoned where applicable. Detailed explanation will be given for the methodology of implementing the derived equations in numerical and discretized form. A comparison will be made between the different techniques in terms of speed and accuracy. The second section includes an identification of the frequency response of a multilayered structure along with simulated scenarios. The following section will establish the forward problem of near-field open-ended RWG FMCW radar. The forward problem will predict the return signal of an applied FMCW signal given a structure model. The observation of the return signal will be commented on.

4.1 The Reflection Coefficient's Γ Computations

4.1.1 The Spatial Distribution of Γ

The value of the reflection coefficient over the aperture is distributed unevenly. Researchers such as [13] and [14] claimed that many modes are bound to be generated due to the sudden change from bounded to unbounded propagation at the waveguide's aperture. The way to visualize the physical interpretation of the multimode generation at the aperture is by inspecting the way the wavefront gets reflected. Varying reflection coefficient will decompose the dominant mode into many other evanescent modes. Due to the geometry of the waveguide and the wavefront of the dominant mode, the distribution of the reflection coefficient is expected to be a symmetric function around the midpoint $(x, y) = (a/2, b/2)$.

Moreover, the reflection coefficient cannot exceed a unity value unless the assumptions made and computational precision affected the results.

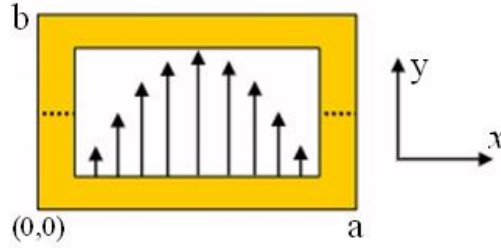


Figure 4.1. Rectangular waveguide's aperture symmetry around the midpoint.

Following is an implementation of Equation (3.9) for different permittivities of an infinite half space (IHS) with different permittivities facing the waveguide's aperture. All the following computations are computed at $f = 9.5GHz$ (well within the X-band) unless stated otherwise.

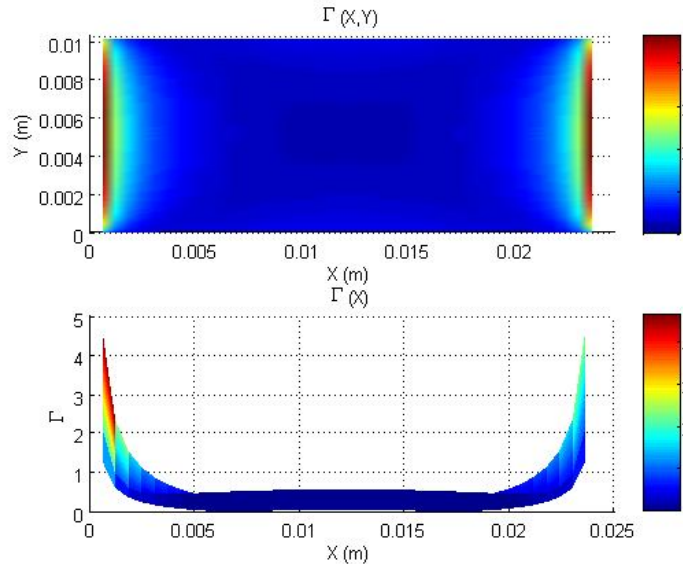


Figure 4.2. The magnitude of the Reflection coefficient over the aperture for IHS of free space $\epsilon_r = 1$.

Since the reflection coefficient cannot be more than unity in magnitude, we can reason the irregularity in Figure 4.2 for three possible causes. It could be caused by the two singularity axes at $x = 0$ and $x = a$ since $\sin\left(\frac{\pi}{a}x\right)$ approaches zero at these edges of the waveguide and we divide by it in Equation (3.9). Moreover, it is partially due to the inaccurate built-in $\sin(x)$ function within Matlab. It could also be due to the assumption made that only fields in the direction of \hat{y} exist. The reason for this last claim is because of a simple fact that the field in the \hat{y} direction is zero but the

field in the direction of \hat{x} is not necessarily zero. This effect is reduced with increased permittivity outside the waveguide's aperture.

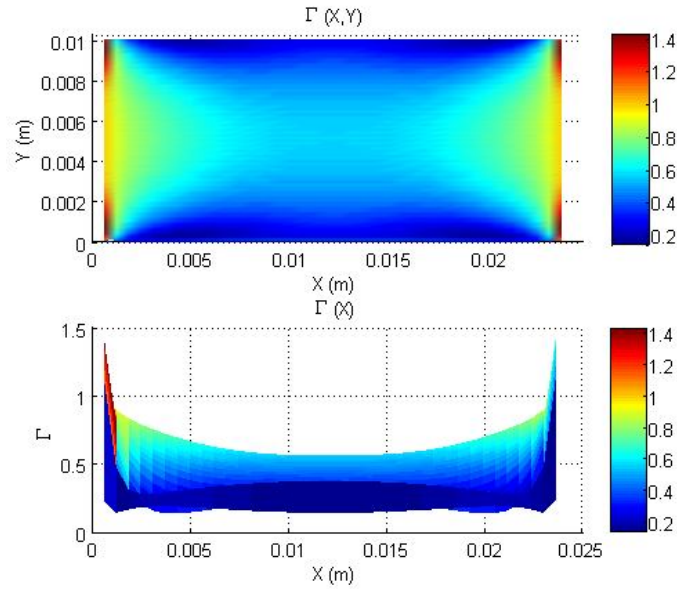


Figure 4.3. The magnitude of the Reflection coefficient over the aperture for IHS of $\epsilon_r = 3$.

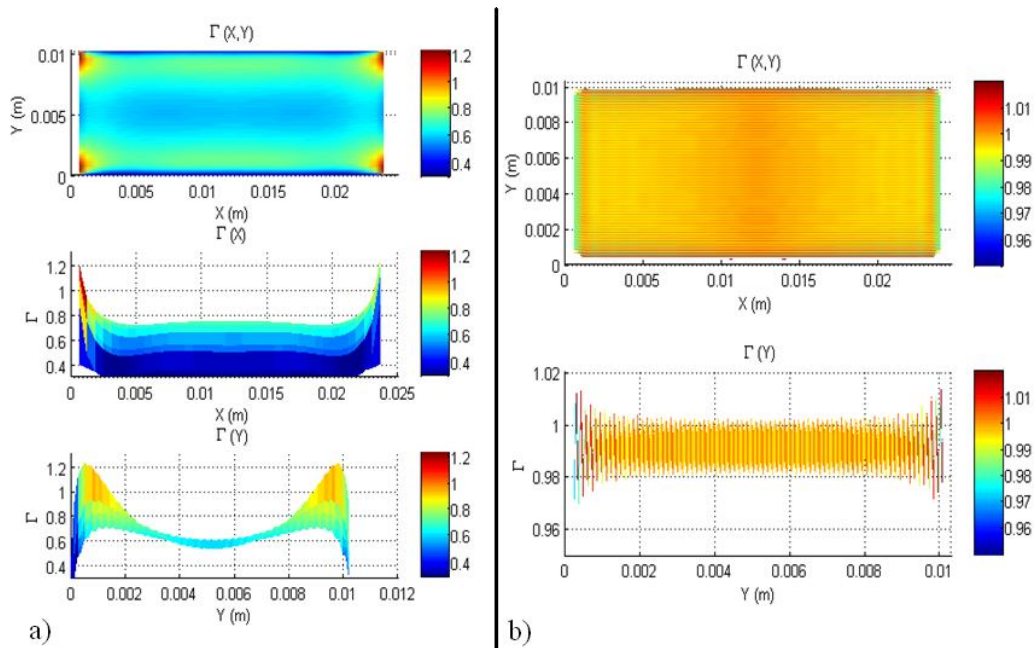


Figure 4.4. The magnitude of the Reflection coefficient over the aperture for IHS of
a) $\epsilon_r = 10$ b) $\epsilon_r \approx \infty$.

As seen in Figure 4.3 and Figure 4.4, the distribution of Γ approaches a more reasonable shape (in terms of the peaks near the singularity) with the increase in the relative permittivity. However, the error will not affect the computations of the effective value of Γ since the sides where the singularities exist are multiplied by very

low weights according to the weight function $\sin^2\left(\frac{\pi}{a}x\right)$ Equation (3.12). In Figure 4.4 b) a rippling effect can be observed clearly. Although, this effect exists in all simulated cases, it is not significant unless the scale is small enough. To see the impact of the ripples on the values more clearly we can take a cross section along the y axis and x axis as shown in Figure 4.5

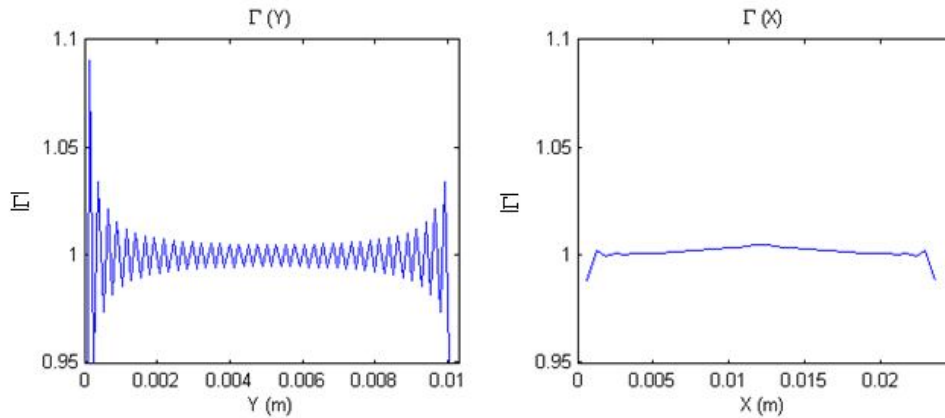


Figure 4.5. The rippling effect in both dimensions along x and along y .

The change along the y axis is a sudden change given by a rectangular function. Meanwhile, the function changes more smoothly along the x axis and is given by a sin function. We can visualize the distribution of the electric field over the aperture as shown in Figure 4.6.

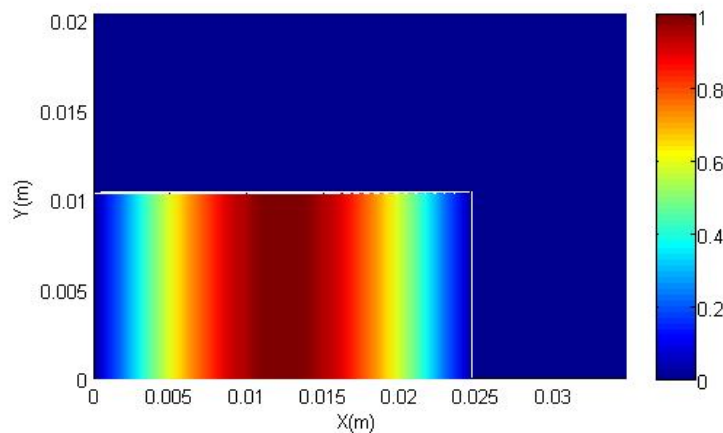


Figure 4.6. The distribution of the electric field over the aperture.

The initial guess for why the rippling effect appeared on the y axis while being much smoother on the x axis was that because of the step change from high to low which produces a lot of frequency leakage. In turn when we limit the frequency domain in terms of the frequency content considered the ripples will appear when we apply the inverse transformation. However, this issue has been thought of before

applying inverse transform such that when the inverse FFT (IFFT) is applied we only get a discrete number of samples on a mesh over the aperture such that these discrete samples are accurate. An illustration for the previous idea can be as follows. Assuming we have a one dimensional rectangular signal as shown in Figure 4.7

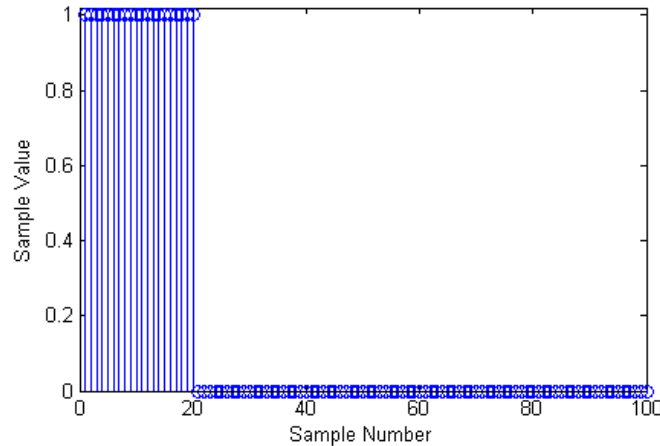


Figure 4.7. One dimensional discrete rectangular signal.

The DFT of a rectangular signal is a discretized sinc function shown in Figure 4.8

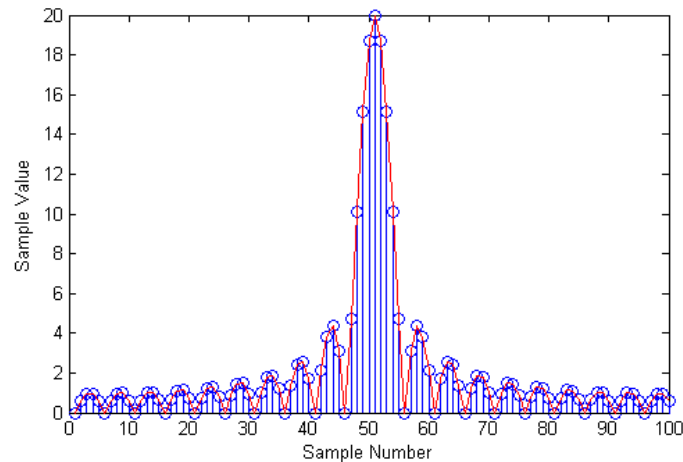


Figure 4.8. The DFT of the discrete rectangular signal (shifted spectrum using fftshift).

Now if we tried to reconstruct the rectangular function from its DFT coefficients then we are going to have an exact representation of the original rectangular function. In our case however, we are computing the DFT spectrum and then we are computing the inverse transformation. Obtaining the proper number of samples with the proper separation is of extreme importance to prevent the appearance of the ripples. For example, if we tried to compute the inverse transformation using the DFT coefficients computed in Figure 4.8 after removing two

samples from the edges of the spectrum we are going to have a distorted version of the original rectangular function Figure 4.9.

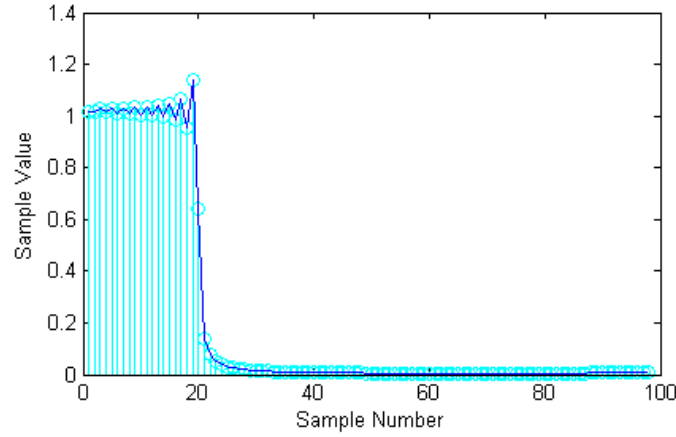


Figure 4.9. Reconstructed Rectangular Signal with the truncated spectrum.

In the developed code this issue was taken into consideration. However, the cause for the ripples was investigated further and it turned out that it was caused by the inaccuracy of the built-in $\text{sinc}(x)$ function. Specifically, the evaluation of $\tilde{\Lambda}(k_x, k_y)$ caused small computational errors which when combined produces the ripples over the distribution of Γ . Recall that $\Lambda(k_x, k_y)$ is given by Equation (4.1)

$$\tilde{\Lambda}(k_x, k_y) = \int_0^b \int_0^a \sin\left(\frac{\pi}{a}x\right) e^{-j(k_x x + k_y y)} dx dy = \frac{ab}{2j} e^{-\frac{jk_y b}{2}} \text{sinc}\left(\frac{-k_y b}{2\pi}\right) \left[e^{\frac{j(\pi - ak_x)}{2}} \text{sinc}\left(\frac{(\pi - ak_x)}{2\pi}\right) - e^{-\frac{j(\pi + ak_x)}{2}} \text{sinc}\left(\frac{(\pi + ak_x)}{2\pi}\right) \right] \quad (4.1)$$

According to the properties of $\text{sinc}(x)$, the function is equal to zero when the argument is a nonzero integer. However, when implemented on Matlab the value was in the order of 10^{-4} which is satisfactory enough in most applications. This inaccuracy and other possible related computational issues caused the appearance of the ripples. To counter this issue FFT was used to compute the Fourier transform. This way the effects of the analytical functions on the computed spectrum are minimized. To do that first we need to define the relation between the samples in the frequency domain (u, v) and the samples in the spatial domain (C, D) . During numerical evaluation of Fourier Transform it is impractical to assume an infinite spatial domain. When implementing DFT using FFT both the frequency, and spatial domains are assumed to be periodic and discrete in nature. The period in the spatial domain should cover a region wide enough such that the function on the edges of that

region is almost zero. If this condition was violated then aliasing will occur and the results will lose its reliability. The region in the simulation will be a function of the waveguide's dimensions a and b such that $0 < x < S_x a$ and $0 < y < S_y b$. Where S_x, S_y are scaling factors along the dimensions (x, y) , respectively.

For TE_{10} the weight function over the aperture has the following formula

$$\Lambda(x, y) = \begin{cases} \sin\left(\frac{\pi}{a}x\right) & 0 \leq x \leq a, 0 \leq y \leq b \\ 0 & a < x < S_x a, b < y < S_y b \end{cases} \quad (4.2)$$

By discretizing the x and y coordinates for numerical evaluation we need to make sure that the domain is sampled properly to avoid aliasing in frequency. Another problem might occur if the sampling in x, y produced margins on the edges of the region under study. To guarantee integer number of samples across the domain two constants referring to the number of steps in each dimension x and y will be defined as L_x and L_y , respectively. Accordingly, the spatial spacing x, y and frequency spacing k_x, k_y will become:

$$\Delta x = \frac{S_x a}{L_x}, \quad \Delta y = \frac{S_y b}{L_y}, \quad \Delta k_x = \frac{2\pi}{S_x a}, \quad \Delta k_y = \frac{2\pi}{S_y b}$$

This assignment of the step size will guarantee proper transfer between the two domains (frequency, and spatial) with minimal irregularity in the numerical approach. Since we sampled both domains then the handling of a finite number of data points is validated and should give us the same results as the continuous approach assuming the inquest rate is satisfied in both regions and assuming that 32-bit accuracy is sufficient.

$$\Lambda(C, D) = \begin{cases} \sin\left(\frac{\pi}{a}C \frac{S_x a}{L_x}\right) & C = 0, 1, 2 \dots \frac{L_x}{S_x}, D = 0, 1, 2 \dots \frac{L_y}{S_y} \\ 0 & C = \frac{L_x}{S_x} + 1 \dots L_x - 1, D = \frac{L_y}{S_y} + 1 \dots L_y - 1 \end{cases}$$

$$\tilde{\Lambda}(u, v) = \mathcal{J} \sum_{D=0}^{L_y-1} \sum_{C=0}^{L_x-1} \Lambda(C, D) e^{-j2\pi\left(\frac{u}{L_x}C + \frac{v}{L_y}D\right)}$$

Where \mathcal{J} is a scaling term so that the function can be used in Equation (3.9)

$$\mathcal{J} = \frac{1}{\Delta k_x \cdot \Delta k_y \cdot L_x \cdot L_y}$$

After implementing the modified version of (3.9) the ripples disappeared over the mesh and it was possible to compute a flat and constant reflection coefficient without any visible error.

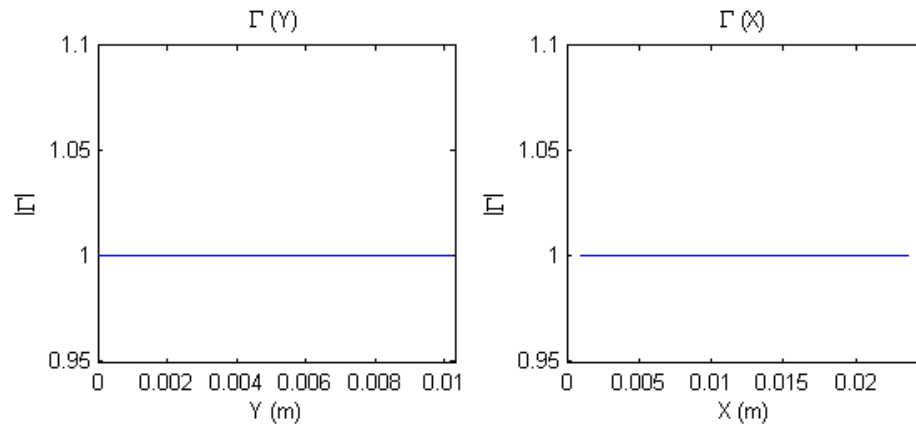


Figure 4.10. The flat response of the reflection coefficient over the aperture.

The new results showed significant improvement over the old approach using the same step size for the mesh covering the aperture as shown in Figure 4.11

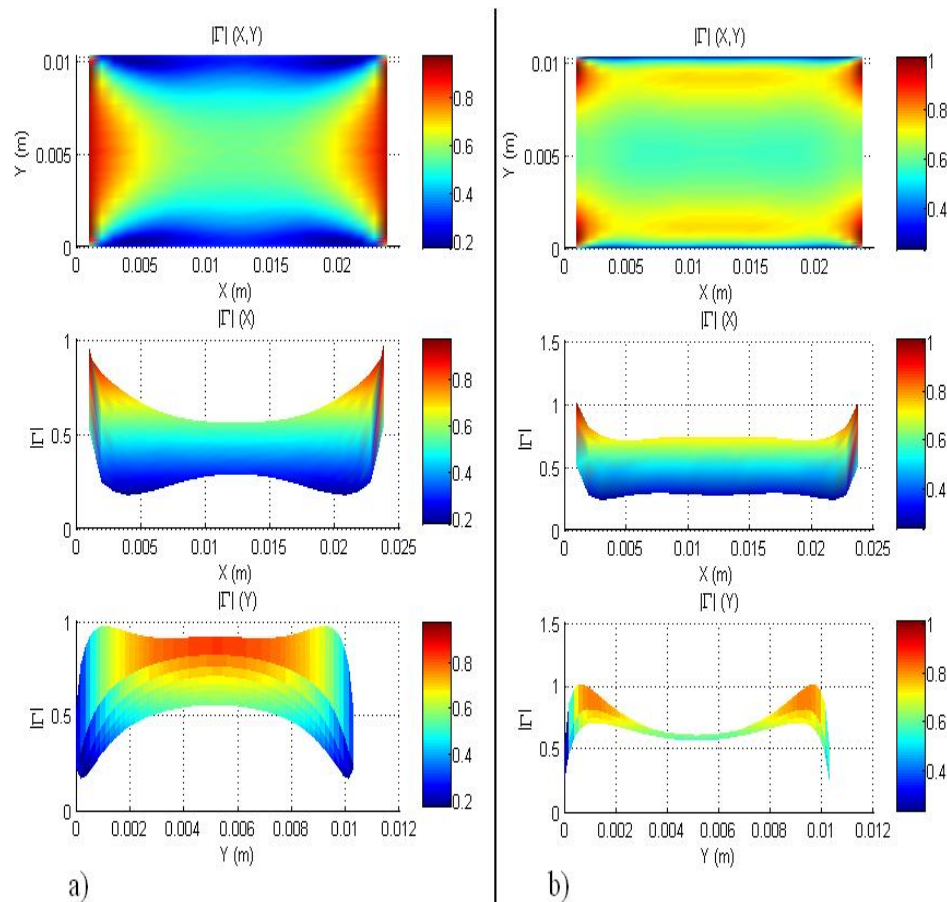


Figure 4.11. The magnitude of the Reflection coefficient over the aperture for IHS using the improved algorithm of a) $\epsilon_r = 3$ b) $\epsilon_r = 10$.

After obtaining a proper representation of the distribution of the reflection coefficient over the aperture more computations were done for increasing permittivity to show the change in the behavior of $\Gamma(x, y)$.

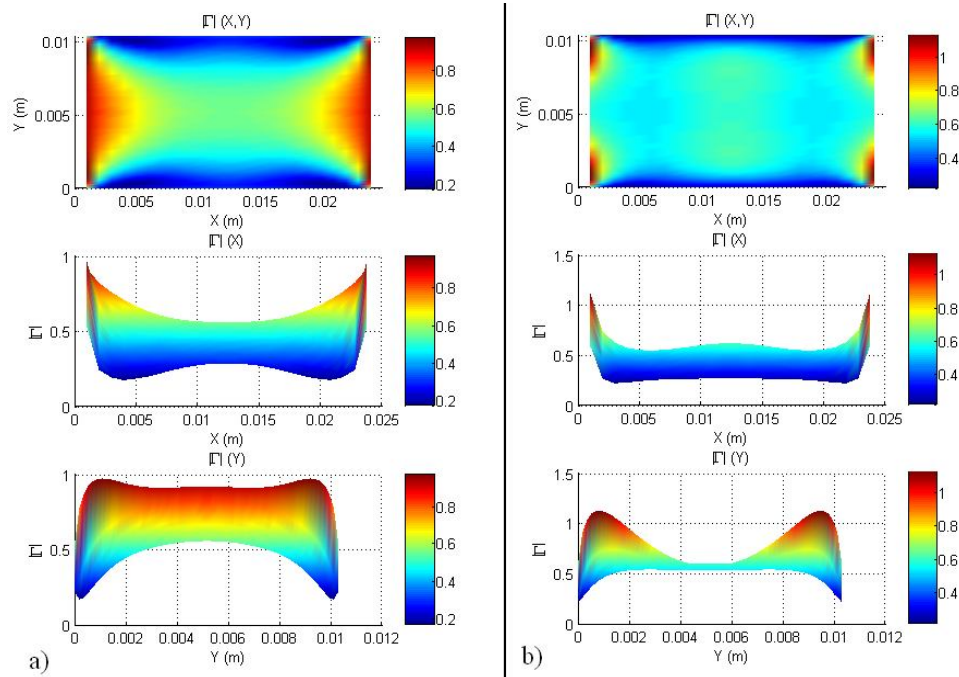


Figure 4.12. The magnitude of the Reflection coefficient over the aperture for IHS using the improved algorithm of a) $\epsilon_r = 3$ b) $\epsilon_r = 5$.

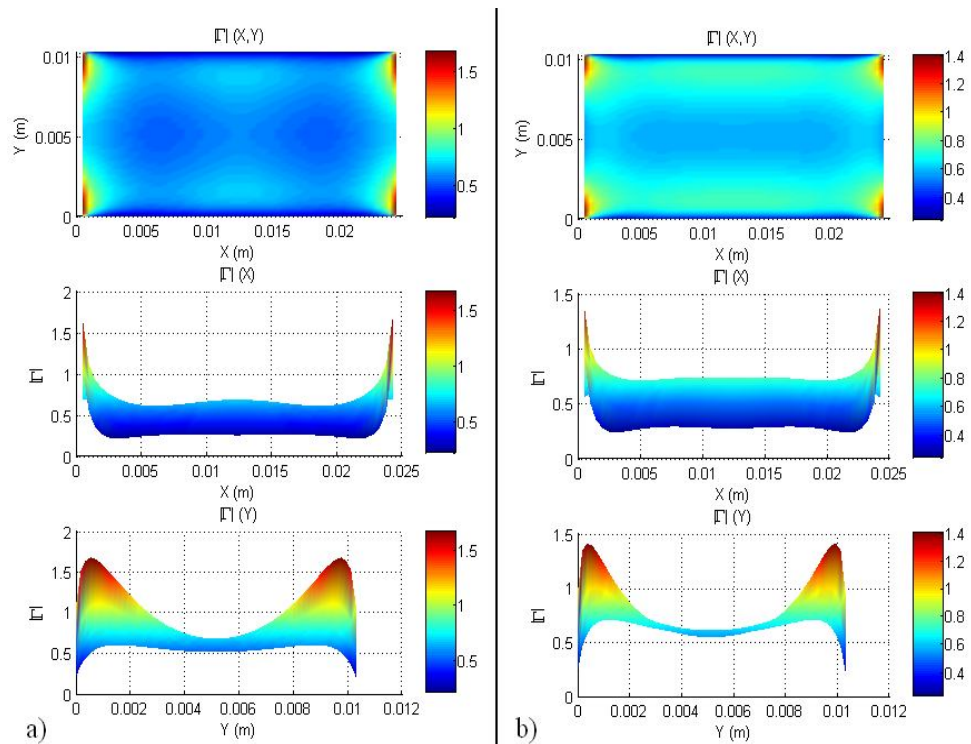


Figure 4.13. The magnitude of the Reflection coefficient over the aperture for IHS using the improved algorithm of a) $\epsilon_r = 7$ b) $\epsilon_r = 10$.

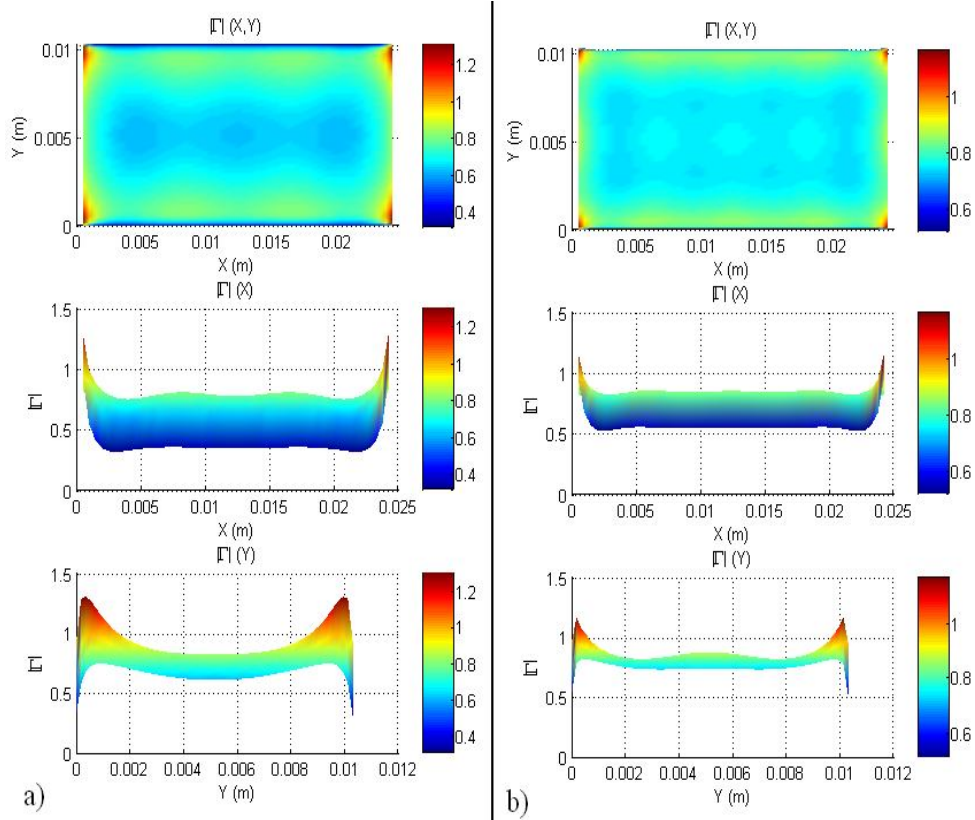


Figure 4.14 The magnitude of the Reflection coefficient over the aperture for IHS using the improved algorithm of a) $\epsilon_r = 15$ b) $\epsilon_r = 30$.

From the previous images we can observe how the reflection coefficient approaches a flat distribution as the permittivity of the IHS facing the waveguide's aperture increases. This behavior explains why the contribution of higher order modes is reduced as a function of increasing permittivity of the layer facing the waveguide's aperture. The small portions at the corners of the image exceed unity due to the computational limitation and the singularity at $x = 0$, and $x = a$.

4.1.2 The Effective Value of the Reflection Coefficient Γ

As discussed earlier in the background chapter, the evanescent modes i.e. the higher order modes do not have enough energy to travel back to the receiver i.e. in this thesis it is the waveguide to coaxial adapter. Hence, the reflection coefficient is measured according to the reflected magnitudes of the modes that can travel through the waveguide. The derivations are done with an assumption of single mode propagation namely TE_{10} and an operating frequency low enough to insure that no higher modes can travel far enough. Hence, the effective measured reflection coefficient is the magnitude of the return TE_{10} mode denoted by Γ . In chapter 3 the

formula to compute Γ was derived and is given by Equation (3.12). Other researchers such as [13] and [14] derived reliable multimode solutions for a single layer. The results obtained using Equation (3.12) will be compared to the results found in [13] which also include some experimental data from [15]. Since worst case scenario happens when the waveguide is faced with an infinite half free space, then maximum expected error will most probably occur under that scenario. It is safe to assume that if the results from the multimode solution were comparable to the results of this thesis at the worst case scenario then other cases are expected to have better matching. Hence, the results of Equation (3.12) will be compared to the results found in [13] for open-ended rectangular waveguide onto an IHS of free space. The testing conditions used to develop the following results are as follows:

- Waveguide: X-band rectangular waveguide $a = 2.286 \text{ cm}$, $b = 1.016 \text{ cm}$
- IHS: Free space with permittivity of $\epsilon_0 = \frac{1}{36\pi} \times 10^{-9} \text{ F/m}$
- Frequency Range: 8.2 – 12.4GHz

In Figure 4.17 a comparison is made between the results of this thesis and the results of [13] using 1 mode, 6 modes and 15 modes to approximate the solution.

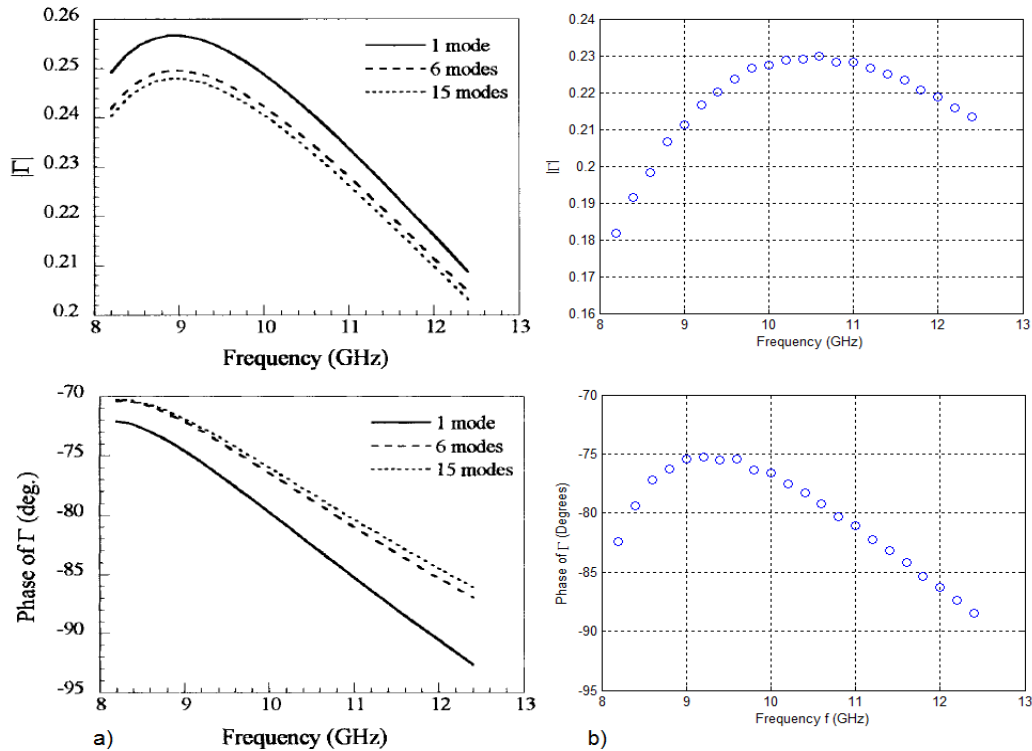


Figure 4.15. Reflection coefficient Magnitude and phase comparison with [13] a) The results of [13] b) The values computed using Equation (3.12).

To compare the results more clearly, the two graphs will be overlaid as shown in Figure 4.16.

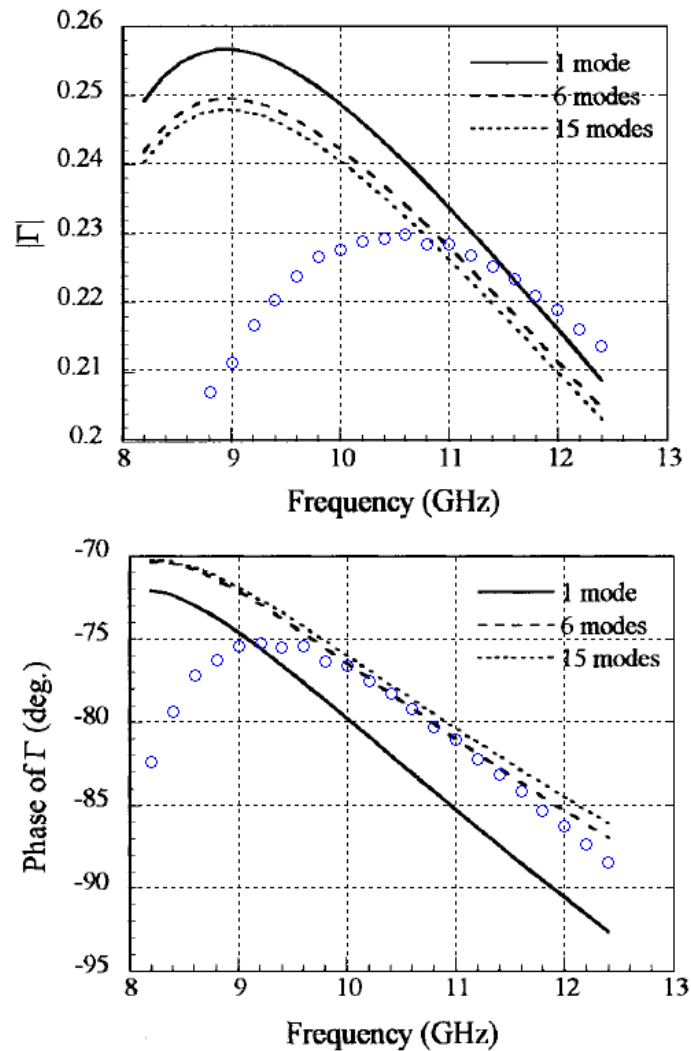


Figure 4.16. The overlaid result comparison of this thesis in blue circles with [13] in black solid and dashed lines.

The maximum difference between the two techniques is around 0.06 in magnitude and around 13° degrees in phase. Compared to the full range of both the magnitude and phase, the maximum error is around 6% in magnitude and less than 4% in phase. Note that given the scale of the reflection coefficient the difference seems more significant than it actually is this is why the admittance measurements will be used as a better comparison representation for the same exact scenario.

The reflection coefficient is directly related to the admittance by Equation (3.13). Figure 4.17 shows the results obtained using multimode approach by [13] where he compared his results with the experimental values of [15] i.e. [18] in his

paper. The comparison was using 1 mode, 6 modes and 15 modes to approximate the normalized waveguide admittance. Where Y_o denotes Y_{10} .

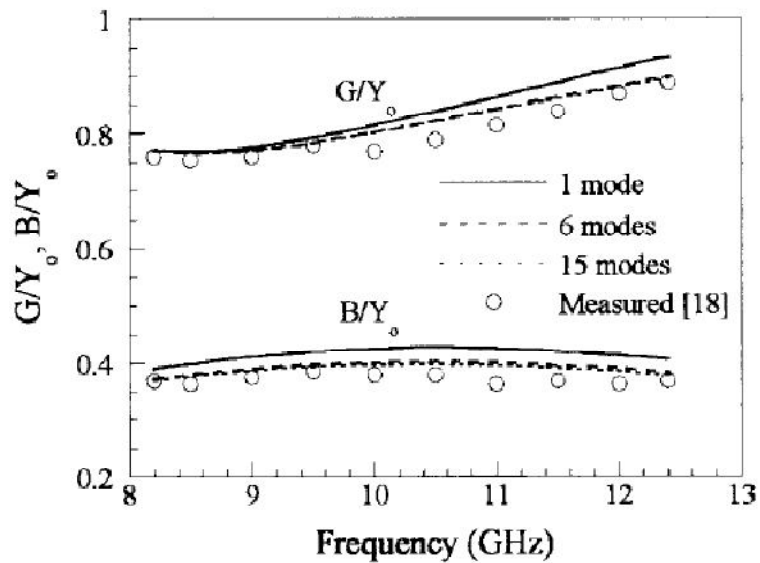


Figure 4.17. Waveguide normalized admittance comparison between [13] and [15].

For a clear comparison with their results the normalized admittance computed in this thesis is overlaid in color on the same graph using the same scale as shown in Figure 4.18.

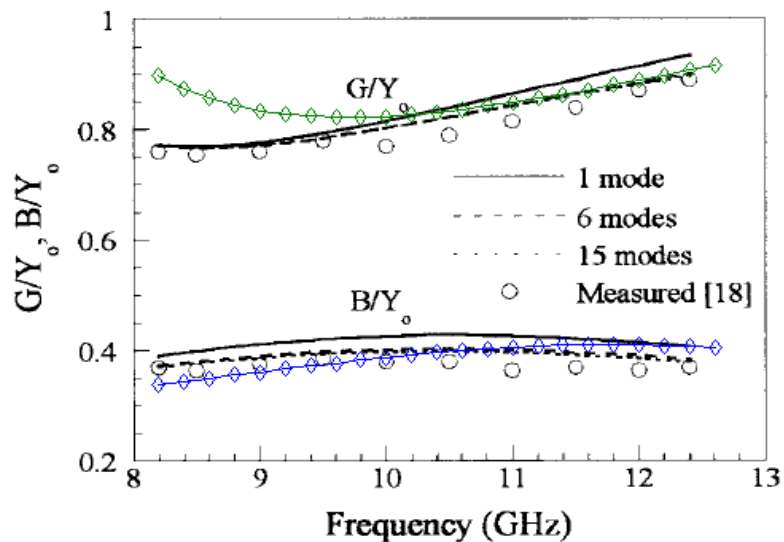


Figure 4.18. Overlaid Waveguide normalized admittance comparison between the results of this thesis and the results obtained by [13] and [15] i.e. written as [18] on the graph.

The maximum difference occurred at the low frequency of the X-band range and is around 0.1 for the real part of the normalized admittance.

After verifying the relative accuracy under the worst case scenario, it is possible to assume that the error in other cases is upper bounded by around 0.06 in magnitude and 13° degrees in phase. To strengthen this assumption other comparisons are made with higher permittivities. In the figures to come the value of ϵ_r refers to the real part of the complex relative permittivity and $\tan(\delta)$ is the loss factor as shown in Equation (2.17). The results published by [13] were derived using 6 modes and are shown in Figure 4.19 while the results obtained using Equation (3.12) are shown in Figure 4.20.

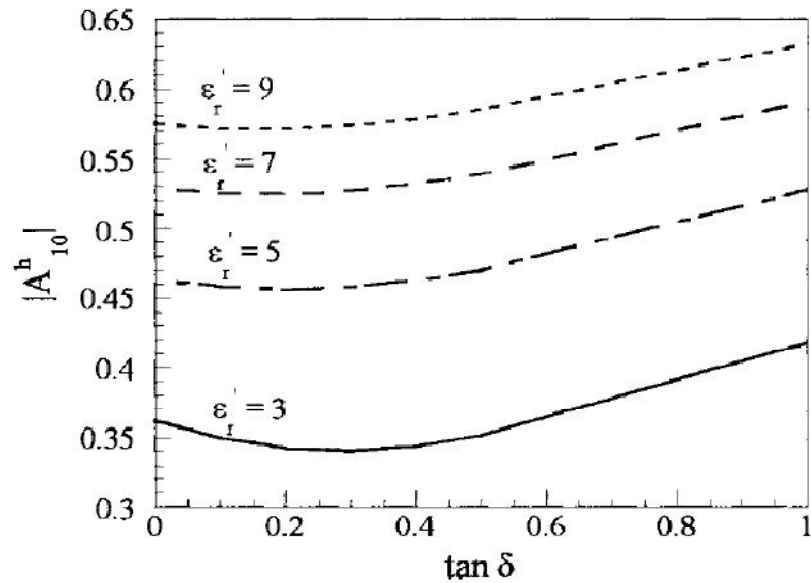


Figure 4.19. Magnitude of Γ as presented in [13] as a function of permittivity using 6 modes.

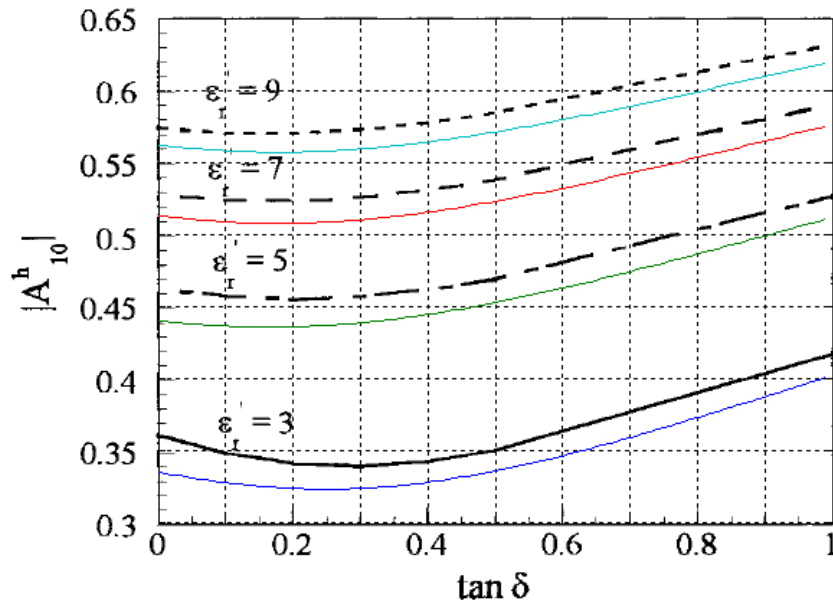


Figure 4.20. Magnitude of Γ using Equation (3.12) in color overlaid over the results found in [13] using 6 modes only.

It was mentioned back in the derivations' chapter that Equation (3.14) provides a much faster evaluation but at the cost of accuracy. In the case of a single layer the accuracy of Equation (3.14) is related to the permittivity of that layer. The reason behind this claim is because the distribution of Γ tends to become flatter over the aperture and the error introduced by the approximation made in Equation (3.14) tends to disappear. The mathematical explanation of the error behavior is best described by Equation (4.3).

$$\frac{\int_0^b \int_0^a \left[\Gamma(x, y) \sin\left(\frac{\pi}{a}x\right)^2 \right] dx dy}{\int_0^b \int_0^a \sin\left(\frac{\pi}{a}x\right)^2 dx dy} \approx \frac{\int_0^b \int_0^a \left[\Gamma(x, y) \sin\left(\frac{\pi}{a}x\right) \right] dx dy}{\int_0^b \int_0^a \sin\left(\frac{\pi}{a}x\right) dx dy} \text{ if } \Gamma(x, y) \approx \text{Constant} \quad (4.3)$$

Figure 4.21 shows the absolute value of the difference between the results of Equations (3.12) and (3.14) as a function of changing permittivity using three different frequencies. The frequencies were selected such that the frequencies define the edges and one of the frequencies of the X-band as defined by [12].

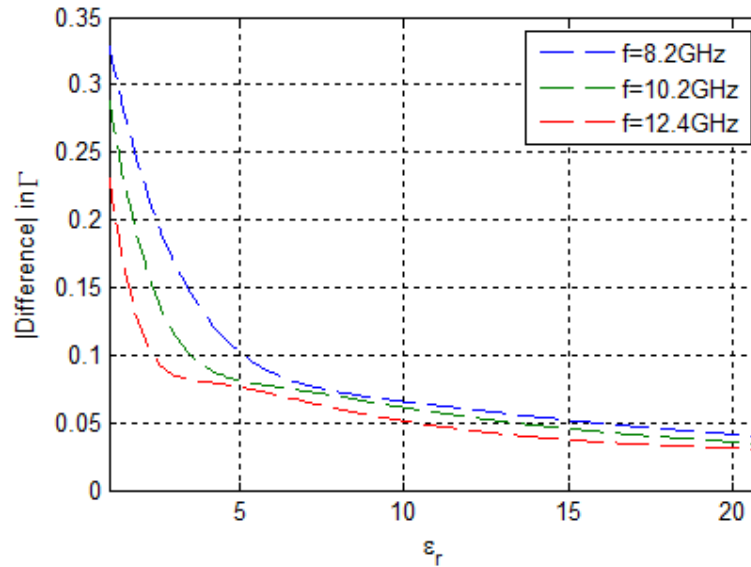


Figure 4.21. The absolute difference in the complex value of Γ for three different frequencies as a function of the relative permittivity ϵ_r .

As shown in Figure 4.21 the difference between the two approaches decreases with increasing permittivity as predicted for all frequencies in the X-band. However, it is important to note that the magnitude difference is considerably less significant than the phase difference given the same permittivity as shown in Figure 4.22 and Figure 4.23.

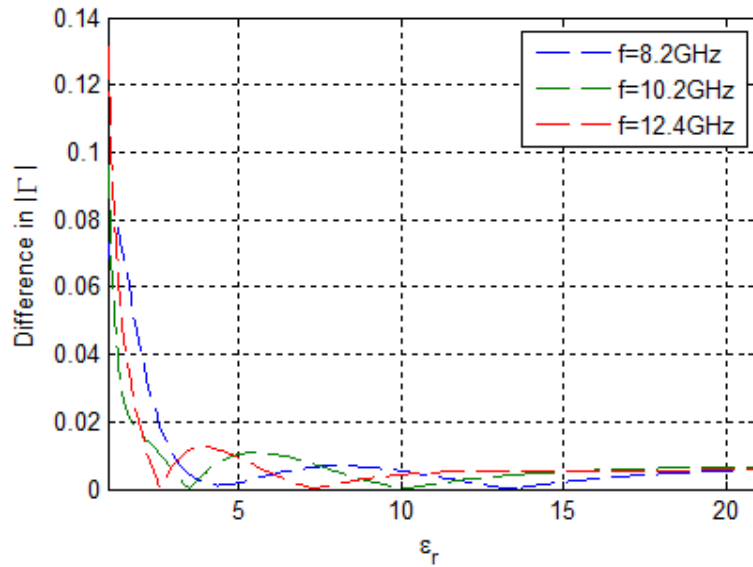


Figure 4.22. The difference in the magnitude of Γ for three different frequencies as a function of the relative permittivity ϵ_r .

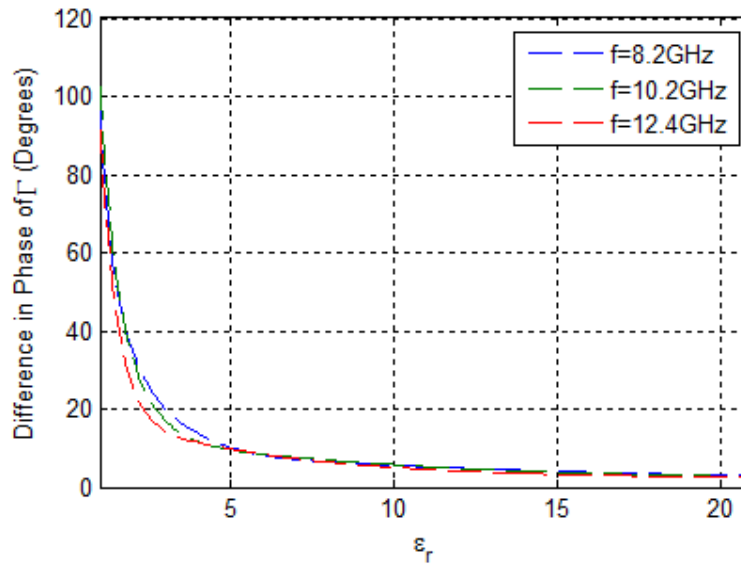


Figure 4.23. The difference in the phase of Γ for three different frequencies as a function of the relative permittivity ϵ_r .

The difference in the phase is what causes most of the difference between the two approaches in computing Γ . While, it can be seen from Figure 4.22 that for $\epsilon_r > 4$ the difference in the magnitude of Γ tends to be well below 2% compared to the full range. Therefore, if we can guarantee that the difference is controlled under a certain level, then the use of the fast algorithm is going to become more reliable when searching for a solution that solves the inverse problem. A possible way to control the difference is by imposing a layer with high permittivity and low loss between the structure and the waveguide. The minimum thickness of this layer can be determined

either experimentally or by reliable simulation. Assuming that the developed simulation formulas are reliable enough, we can sweep the properties of the first layer to determine the conditions under which the maximum difference between the two algorithms is 2%. We will start with $\epsilon_r = 4$ in unity steps up to $\epsilon_r = 13$ such that for each trial the thickness will be swept over $0.01 - 10\text{cm}$ in steps of 1 mm and Γ will be computed using Equations (3.12) and (3.14). Note that the layer is backed by an IHS of free space since it theoretically introduces worst case scenario.

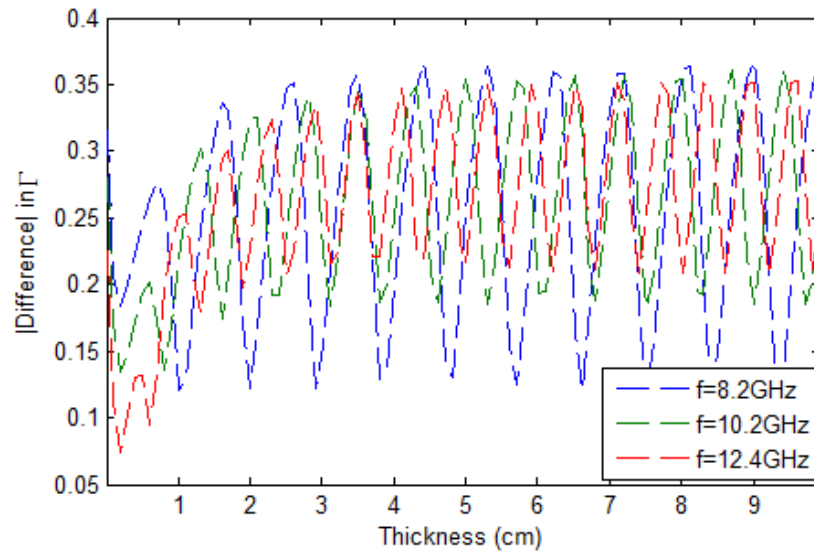


Figure 4.24. Magnitude of the difference between Equations (3.12) and (3.14) as a function of thickness of first layer and frequency for $\epsilon_r = 4$.

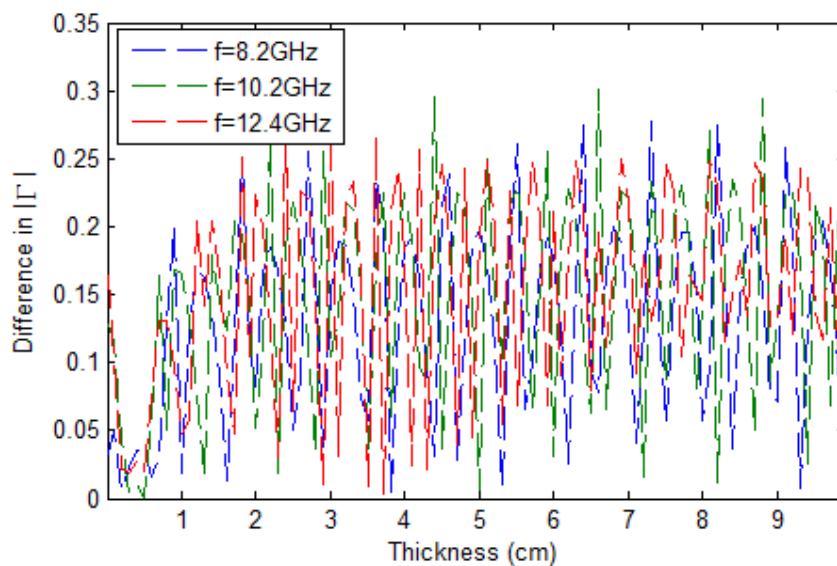


Figure 4.25. The Difference in magnitude between the Equations (3.12) and (3.14) as a function of thickness of first layer and frequency for $\epsilon_r = 4$.

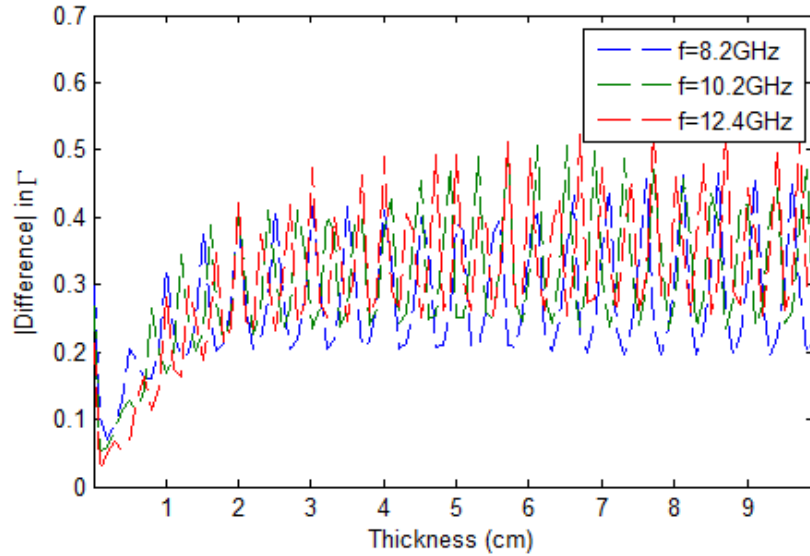


Figure 4.26. Magnitude of the difference between Equations (3.12) and (3.14) as a function of thickness of first layer and frequency for $\epsilon_r = 13$.

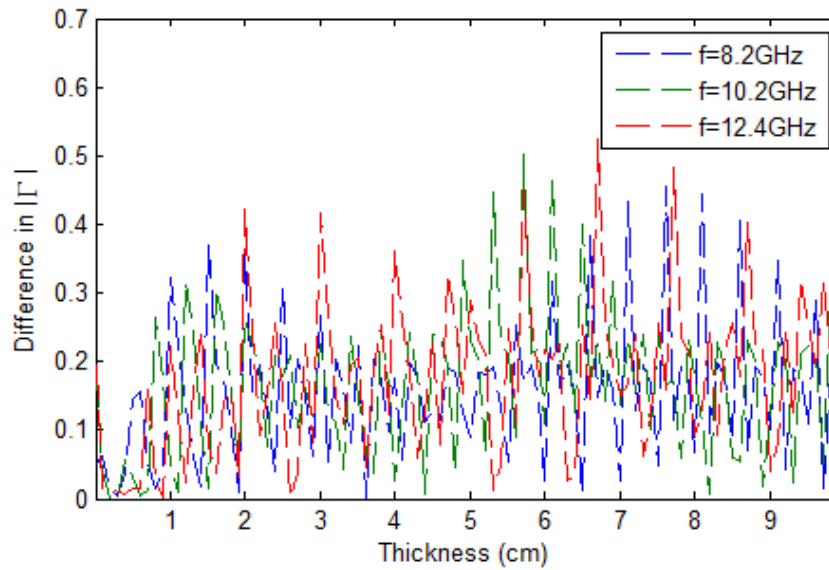


Figure 4.27. The Difference in magnitude between the Equations (3.12) and (3.14) as a function of thickness of first layer and frequency for $\epsilon_r = 13$.

A pattern can be clearly seen in Figure 4.24 and Figure 4.26. The difference is periodic as a function of thickness. The period is equal to half the wavelength within the first layer. The reason behind the periodic behavior is due to the constructive and destructive addition of the two return signals. One signal is reflected directly at the aperture while the other reflection comes from the interface between the first layer and the free space backing. This behavior can be reasoned in different ways. One way is by observing the distribution of the reflection coefficient over the aperture for the case where the first layer has a relative permittivity of $\epsilon_r = 13$ and a thickness of

1cm backed by free space Figure 4.28. It is evident that the distribution is not constant and cannot be approximated by a constant over the aperture hence the error introduced by Equation (3.14) is significant.

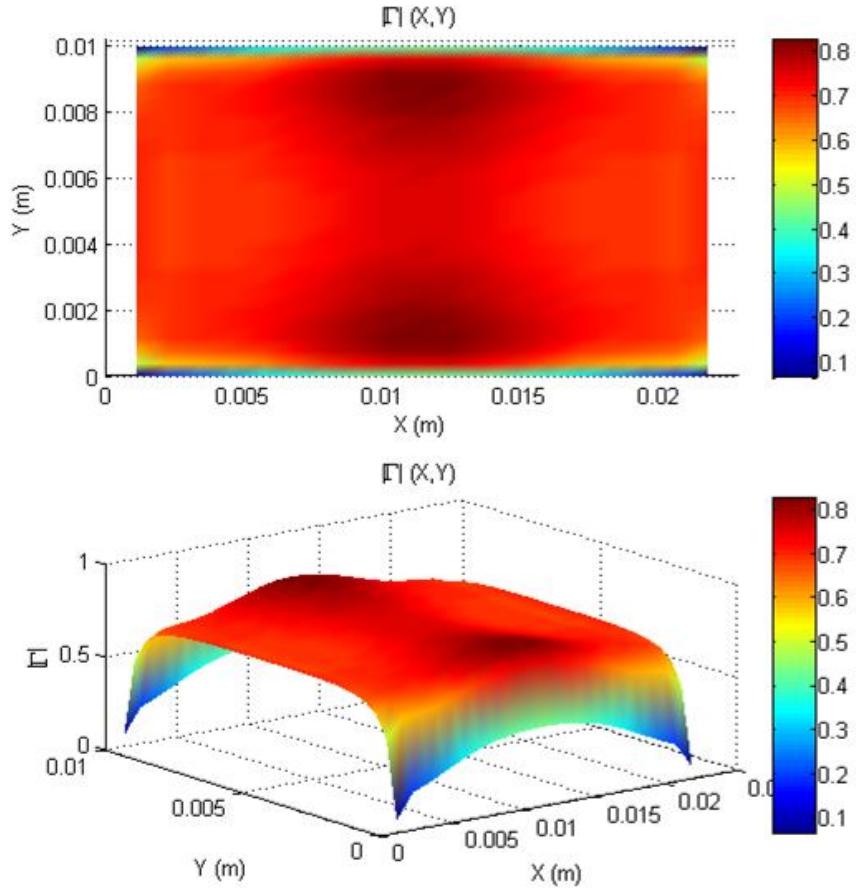


Figure 4.28. The distribution of Γ over the aperture for a single layer with $\epsilon_r = 12$ and 1.5cm thickness.

In addition, Equation (3.14) evaluates the function at $k_x = k_y = 0$ which mathematically refers to a plane wave that does not decay with distance. Theoretically as the second interface gets further away its effect diminishes. Equation (3.12) matches this prediction. Figure 4.29 shows how $|\Gamma|$ converges as the second interface gets further away from the aperture while this does not happen when using Equation (3.14) as shown in Figure 4.30. The difference between the two approaches is significant once there is an interface far enough from the aperture. On the other hand, there exists a gap within the first centimeter where there is a good match between Equation (3.12) and (3.14) for all frequencies. To show the relation of this gap with the permittivity, another simulation was conducted with finer steps for the range between 0.1 – 10mm in steps of 0.1 mm. By observing the difference in $|\Gamma|$ for three

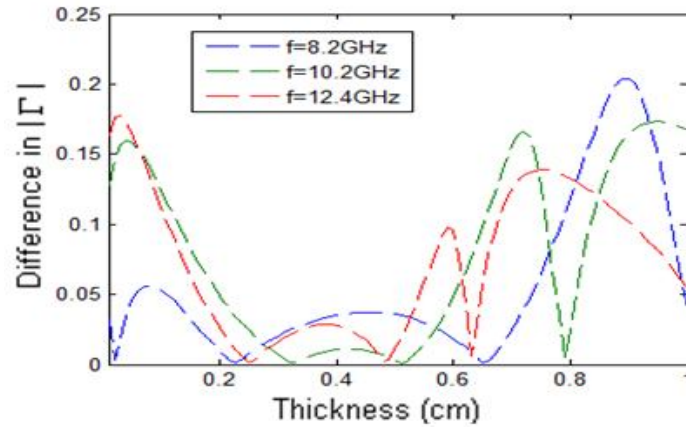


Figure 4.31. The Difference in magnitude between the Equations (3.12) and (3.14) as a function of thickness of first layer and frequency for $\epsilon_r = 4$.

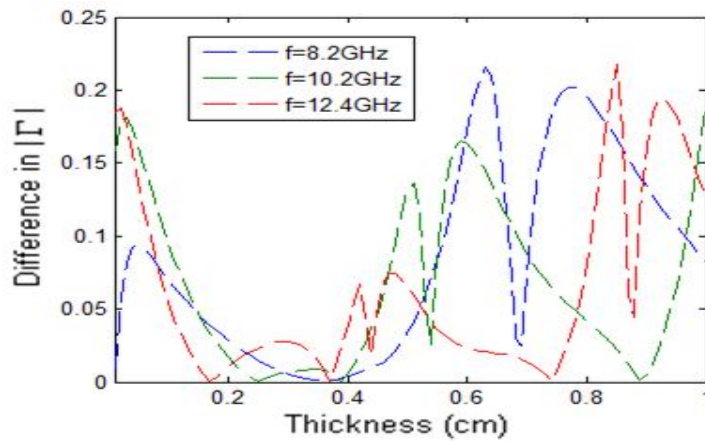


Figure 4.32. The difference in magnitude between the Equations (3.12) and (3.14) as a function of thickness of first layer and frequency for $\epsilon_r = 8$.

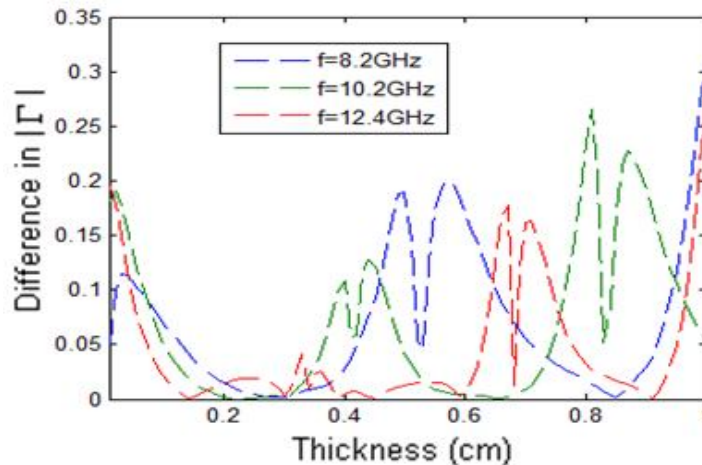


Figure 4.33. The difference in magnitude between the Equations (3.12) and (3.14) as a function of thickness of first layer and frequency for $\epsilon_r = 13$.

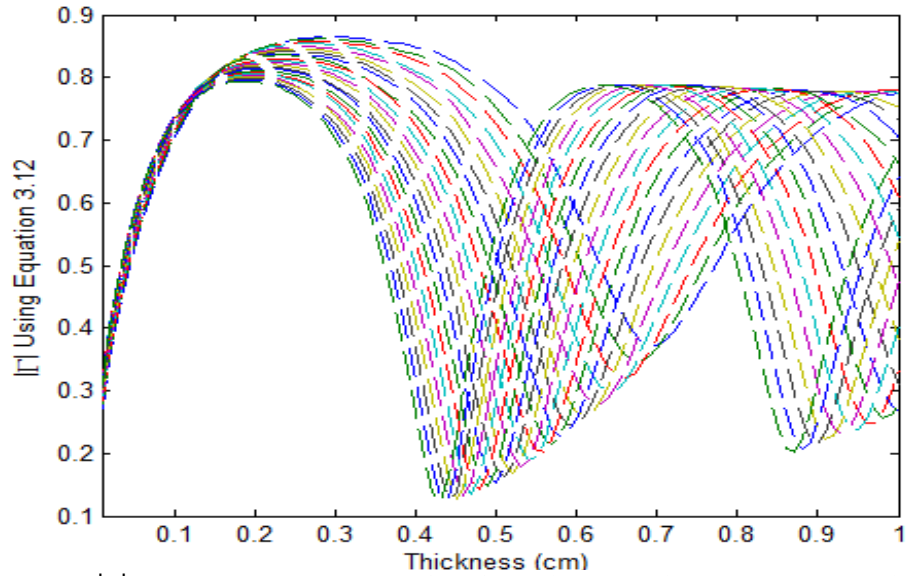


Figure 4.34. $|\Gamma|$ as computed by Equation (3.12) as a function of varying thickness of first layer over the X-band range and $\epsilon_r = 8$, starting from 8.2 GHz (blue inner most) up to 12.4GHz.

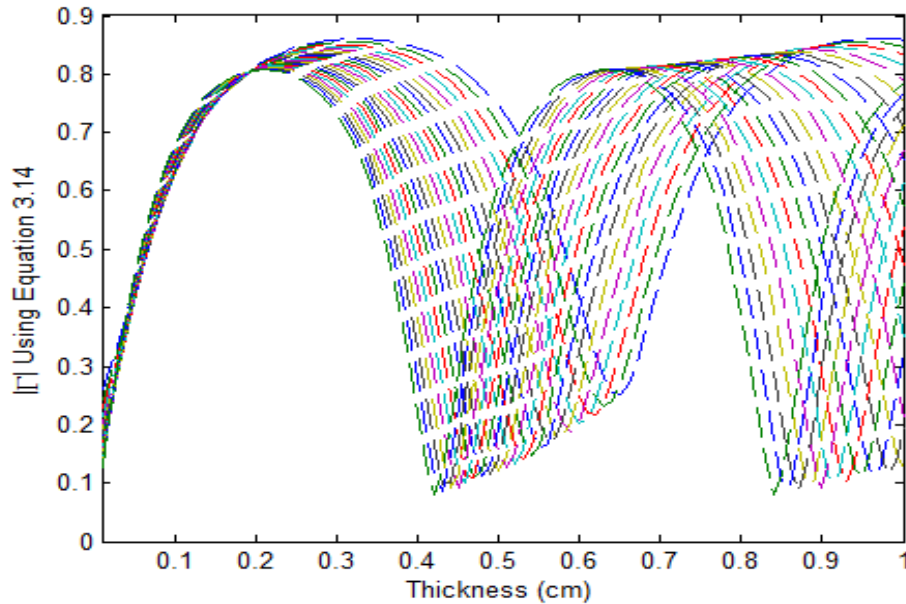


Figure 4.35. $|\Gamma|$ as computed by Equation (3.14) as a function of varying thickness of first layer over the X-band range and $\epsilon_r = 8$, starting from 8.2 GHz (blue inner most) up to 12.4GHz.

Despite the apparent similarity, the computed difference between the two algorithms exceeds 20% in some values and at others it drops to zero. In conclusion, Equation (3.14) is not a reliable replacement of Equation (3.12). However, visual comparison might become handy in predicting the general shape within the first few millimeters.

4.2 Frequency Response of a multilayered structure

4.2.1 LTI System Analogy

A Linear Time Invariant (LTI) system is a basic type of systems used widely in the literature of signal processing and many other fields. An LTI system is defined to possess the linearity property and no dependence on the time at which an input is applied. To explain the analogy of an LTI system with multilayered structures the following paragraphs are given in detail.

The reflection coefficient Γ at the waveguide's aperture is determined by the structure's properties. The structure in this thesis is considered to be a multilayer nonmagnetic dielectric structure. Each layer is defined by its relative permittivity ϵ_{r_n} and thickness i.e. the depth at which this layer ends d_n . A fixed structure with simple media illuminated by an open-ended RWG can be proven to act like a linear system where the input is the incident wave and the output is the reflected wave. In literature this fact is taken for granted and can easily be proven by an experiment. It means that a signal can be decomposed into its basis functions and dealt with each separately to obtain the combined final output i.e. reflected signal. I based this observation on the way multimode solutions are obtained and on how modes inside a waveguide are dealt with separately even if the waveguide is operating way above its dominant mode frequencies. Moreover, there is absolutely no dependence of the return of a certain signal on any other existing signals when assuming simple media (linear, isotropic and homogenous). The fact that a structure is time invariant is also widespread in literature, not necessarily explicitly, since the time factor is usually taken out of the equation by just assuming harmonic time dependence. Therefore, any time shift will also be taken out and returned at the end of the solution. To wrap up the analogy between a conventional LTI system and the reflections from a multilayer structure the following bullet points are given:

- A multilayered structure can be viewed as an LTI system.
- The incident signal is the input to that LTI system.
- The return signal after passing the waveguide back to the coaxial cable is the output of the system (only the dominant mode will reach the coaxial cable).

-
- The reflection coefficient for a single operating frequency is a constant and can be thought of as the Eigen value of the system at that frequency.
 - The Eigen functions in this case are pure sinusoids which are also used as basis function in Fourier transform.

Evaluating a single frequency measurement f provides a single complex value of the reflection coefficient Γ . We can think of any multilayered structure as a system and Γ is the Eigen value for that specific structure at that specific Eigen function i.e. the sinusoid with the frequency of operation f .

4.2.2 Frequency Response

Since any LTI system can be fully described by its frequency response, the same goes for any multilayered structure made of simple media. However, there is no guarantee for the uniqueness of the structure. In other words, there is a one to one relationship going from the structure model to its frequency response, but it is not proven to be one to one relation when going from the frequency response to the structure parameters. Given the complexity of the inverse problem the study of uniqueness can be left for an independent research. In this thesis it will be assumed that it is unique.

4.2.2.1. Two Layer Structure

A simple structure consisting of one layer backed by an IHS of another medium was simulated to obtain its frequency response over the X-band as shown in Figure 4.36. The structure has the following parameters:

First layer: 1cm- thickness, with $\epsilon_r = 4.5 - 0.045j$

Second layer: IHS , with $\epsilon_r = 1.1 - 0.0026j$

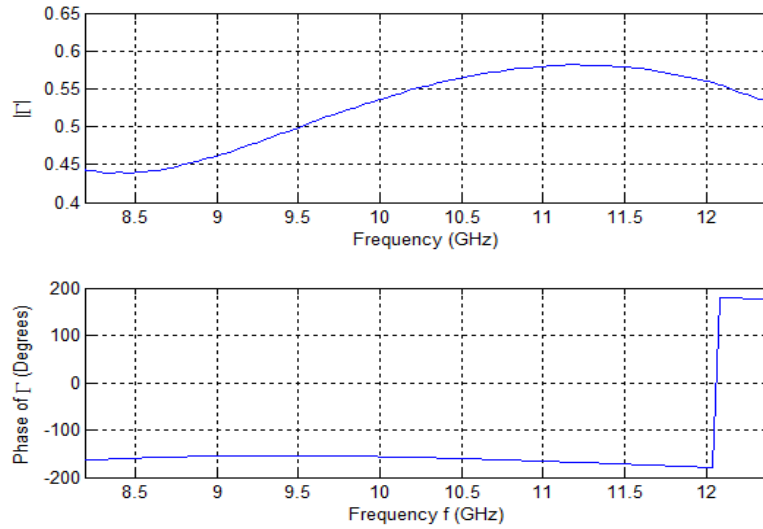


Figure 4.36. The frequency response of a simple structure consisting of two layers over the X-band.

Given the frequency response of the simple structure a question might arise about the possible resolution we can achieve with the X-band range of frequencies. It is possible to try and test the effects on the frequency response if the thickness of the first layer changed. In order to do that, the first layer will be varied over the range 0.5-1.5 m in steps of 0.1mm while keeping the rest of the variables constant. The behavior of the frequency response can be shown as a function of first layer thickness and frequency in Figure 4.37.

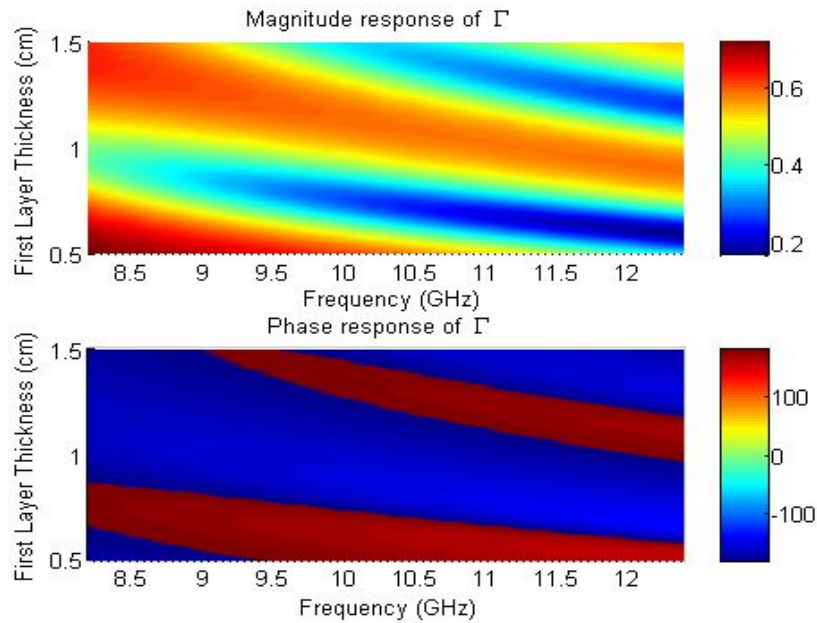


Figure 4.37. The change in the frequency response of the structure as a function of varying thickness over the X-band frequency range.

4.2.2.2. Six Layer Structure:

To enrich the problem, a complex structure consisting of five layers backed by an IHS of free space was simulated. The structure is a practical sandwich composite structure described in [1] and truncated to five layers with air backing Figure 4.38.

The modeled structure has the following parameters:

First layer: 2.5mm- thickness, with $\epsilon_r = 4.5 - 0.045j$

Second layer: 0.3mm- thickness, with $\epsilon_r = 3.1 - 0.01j$

Third layer: 1cm- thickness, with $\epsilon_r = 1.1 - 0.0026j$

Fourth layer: 0.3mm- thickness, with $\epsilon_r = 3.1 - 0.01j$

Fifth layer: 2.5mm- thickness, with $\epsilon_r = 4.5 - 0.045j$

Sixth layer: air backing, IHS, with $\epsilon_r = 1$

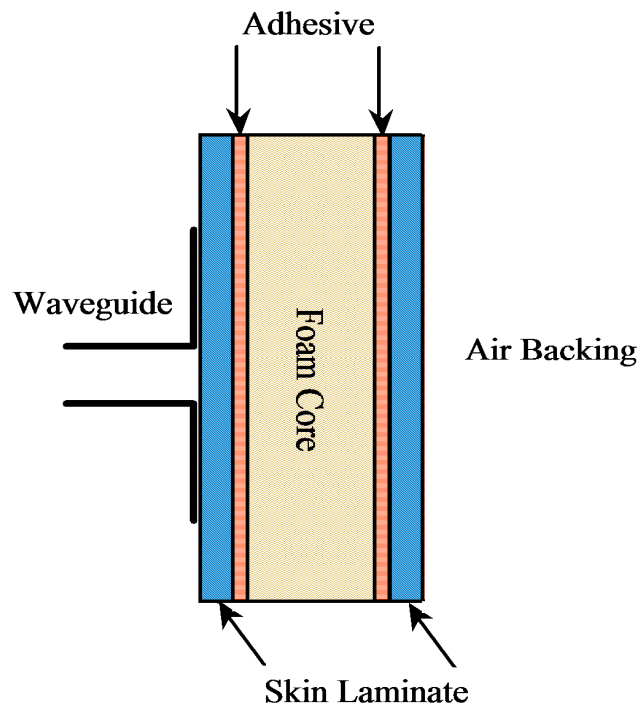


Figure 4.38. Schematic of the truncated sandwich composite [1].

Its frequency response over the X-band frequency range is shown in Figure 4.39.

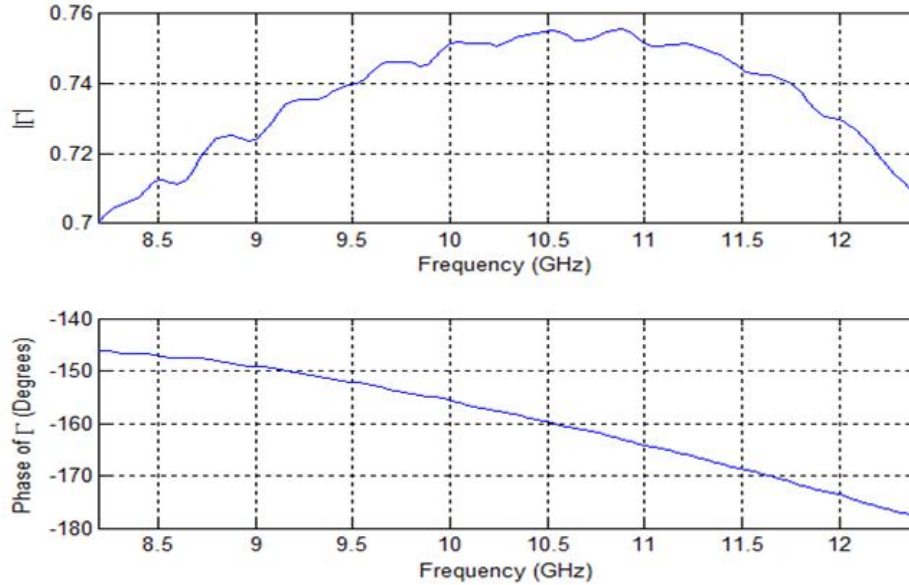


Figure 4.39. The frequency response of a complex structure consisting of six layers over the X-band.

Assuming that we are interested in the thickness of the foam layer, we will vary the thickness from 0.5 cm to 1.5 cm and record the frequency response for every change of 0.1mm. Overall 100 frequency response simulations will be recorded and plotted as a two dimensional surface with the color representing the value. The simulation result is shown Figure 4.40.

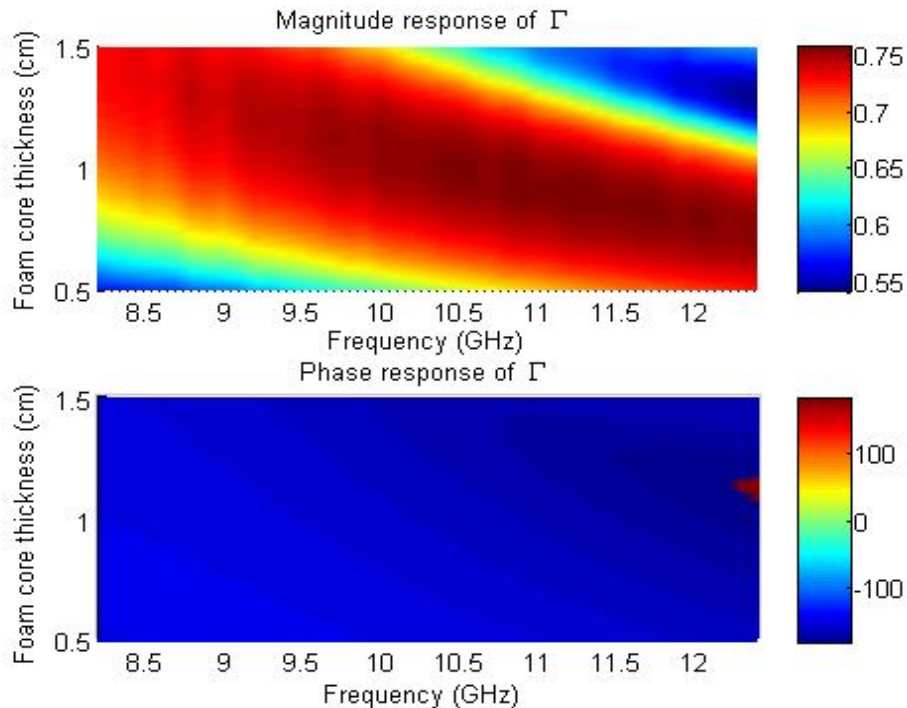


Figure 4.40. The change in the frequency response of the structure as a function of varying thickness over the X-band frequency range.

The phase response in Figure 4.40 appears to be flat however the existence of a jump in the frequency value from -180 degrees to 180 degrees created a discontinuity in the graph. The variations of the phase are indistinguishable since the intensity variations of the blue color are not clear. To enhance the changes within the phase a built-in Matlab function known as “unwrap” will be used to force the values to go beyond -180 degrees instead of jumping to +180 degrees. The “unwrap” function will be used just for illustration purposes Figure 4.41.

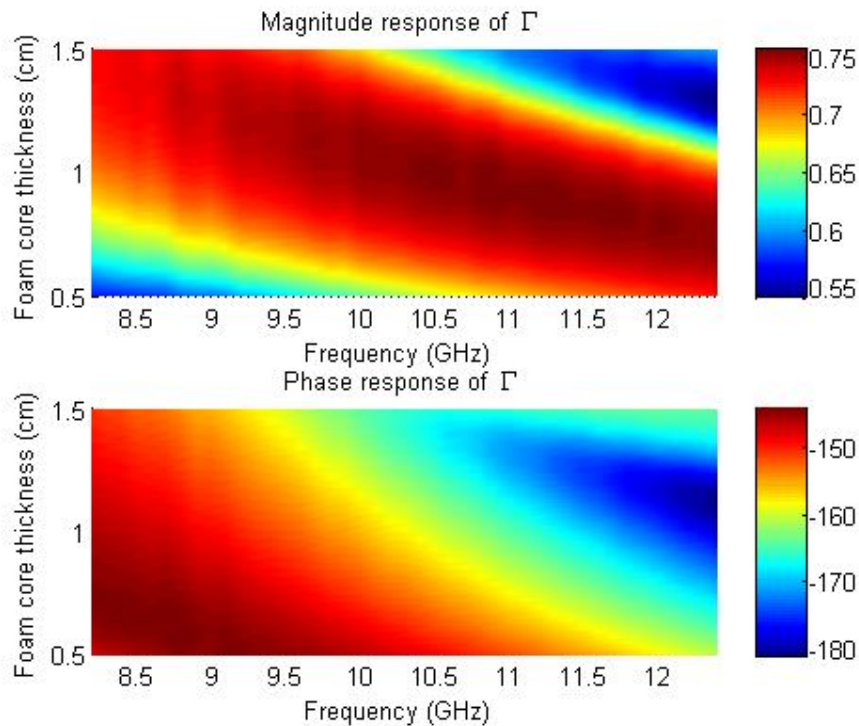


Figure 4.41. The change in the phase response of the structure as a function of varying thickness over the X-band frequency range (unwrapped phase response).

4.2.3 Impulse Response

Given the complexity of the forward problem, it is hard to find a direct relation that could relate the structure’s parameters to its frequency response. However, if we theoretically compute the frequency response of a structure over a sufficiently wide bandwidth a relation between the structure and its impulse response can be made. As shown in Figure 4.42 the approximate impulse response was computed using an equivalent bandwidth of $300GHz$ for the structure model given in Figure 4.38 with foam thickness of 0.5 cm.

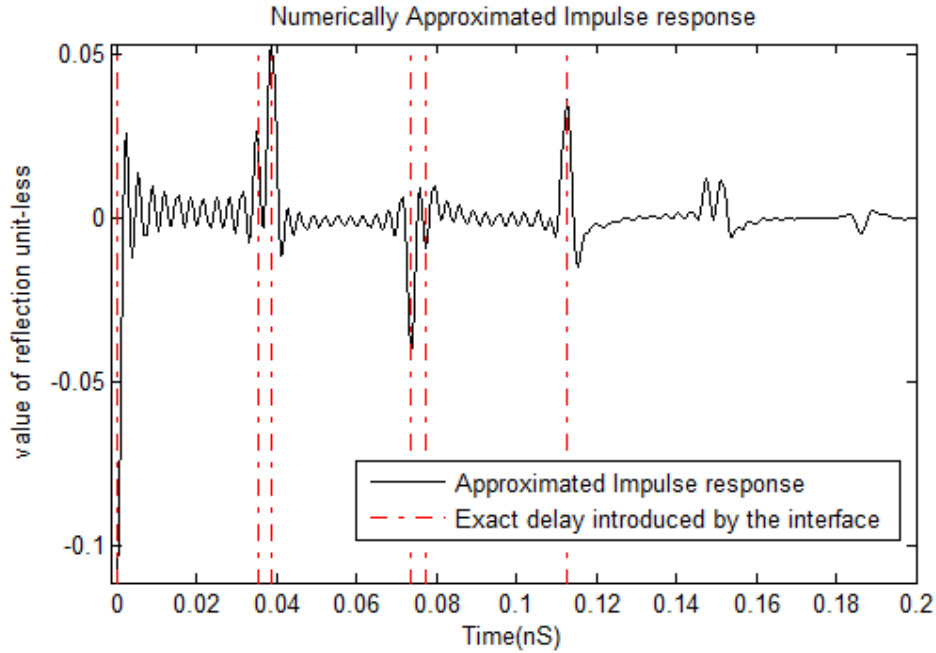


Figure 4.42. Approximated impulse response using a band limited frequency response of 300GHz bandwidth.

The band limited impulse response provides sufficient information about the structure. Each impulse represents a reflection from an interface or an echo due to multiple reflections. The multiple reflection scenario happens when a signal reflect from the same interface twice when trapped within a layer.

4.3 FMCW Radar Simulation

The return of FMCW can be simulated by either convolving the time domain FMCW signal with the structure's impulse response or by simply multiplying the frequency domain representation of the signal with the structure's frequency response according to the convolution theorem. Let \mathcal{F} denote the Fourier transform operator, the asterisk $*$ denote the convolution operator and f and g denote the system's impulse response and the input signal in the time domain, respectively. Then the convolution theorem is mathematically represented by Equation (4.4).

$$\mathcal{F}\{g * f\} = \mathcal{F}\{g\} \cdot \mathcal{F}\{f\} \quad (4.4)$$

The frequency response of a multilayered structure can be computed as explained in the previous section. Using the computed frequency response it is possible to obtain the return FMCW signal. The return signal is as accurate as the estimated frequency response of the structure. Assuming the frequency response is

sufficiently accurate then mixing the FMCW signal with the reference transmitted signal will result in the beat frequency spectrum as explained in the literature review chapter. A structure consisting of two layers will be used to simulate the FMCW radar. The linear chirp used to represent the FMCW signal is given by Equation (4.5)

$$g(t) = \sin\left(2\pi f_o t + \alpha \frac{t^2}{2}\right) \quad (4.5)$$

Where t denotes time, f_o denotes the initial frequency at which the chirp starts and α denotes the rate at which the frequency changes with time and it is given by the following relation:

$$\alpha = \frac{f_1 - f_o}{T_{sw}} \quad (4.6)$$

Where f_1 is the final frequency at which the chirp stops and T_{sw} is the sweeping period.

The parameters used to simulate the FMCW radar are given in Table 4.1.

Table 4.1. FMCW radar parameters.

Symbol	Description	Value
f_o	Initial sweep frequency	8.2 GHz
f_1	Final sweep frequency	12.4 GHz
n	Number of samples per sweep	5000
T_s	Sampling interval	$5 \times 10^{-13} s$
T_{sw}	Sweep (Chirp) time	$nT_s = 2.5 \times 10^{-9} s$
C	Speed of light	$3 \times 10^8 m/s$
BW	Chirp frequency Bandwidth	$BW = f_1 - f_o = 4.2 GHz$
α	Chirp slope	$\alpha = \frac{BW}{T_{sw}} = 1.68 \times 10^{18} Hz/s$
Win	Window Type	Rectangular/Hamming

The structure to be simulated is a two layer structure with the following parameters:

First layer: 0.1-10cm- varying thickness, with $\epsilon_r = 3$

Second layer: IHS, with $\epsilon_r = 50$

The parameters were chosen such that visual observation is enough to convey the concepts which to be discussed in this section. The concept of overlapping beat

frequencies discussed in 2.1.2 will be illustrated since it is one of the main issues encountered in FMCW radars. In order to simulate the operation, the structure's frequency response was computed for all the cases of different thickness as shown in Figure 4.45. The two extreme cases i.e. thicknesses of 0.1 cm and 10 cm have the frequency responses shown in Figure 4.43 and Figure 4.44, respectively.

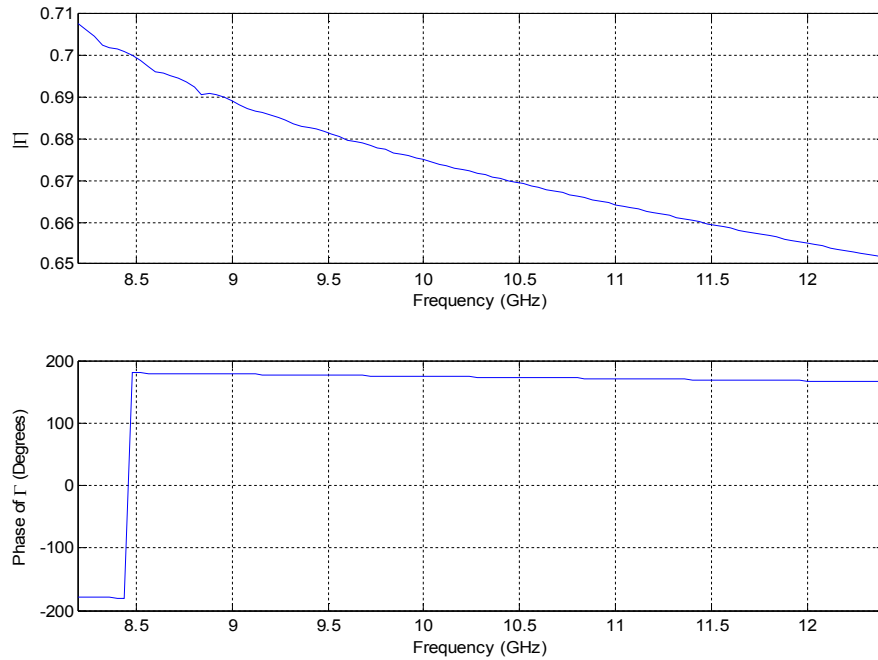


Figure 4.43. The frequency response of the structure when the first layer thickness is 0.1cm.

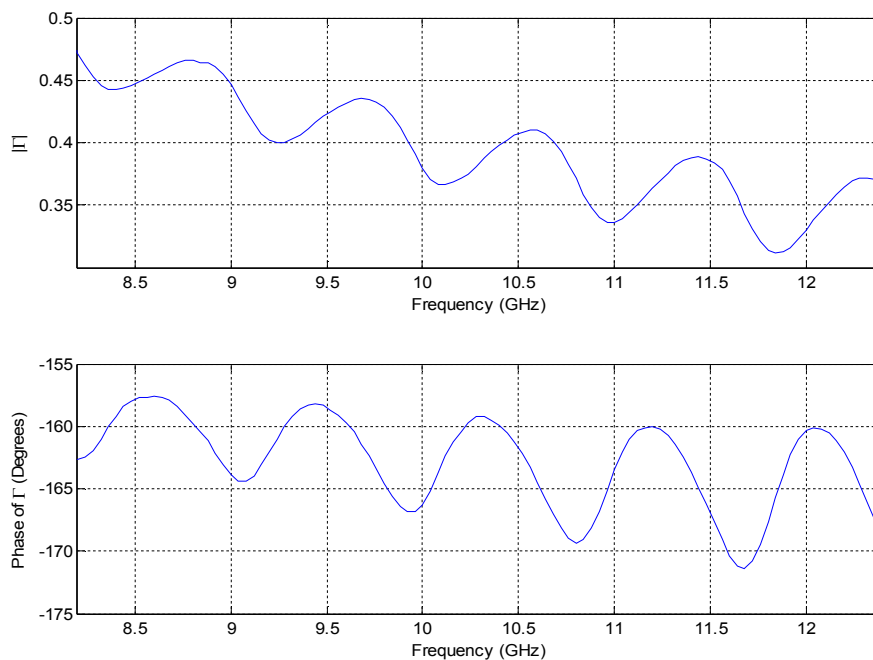


Figure 4.44. The frequency response of the structure when the first layer thickness is 10cm.

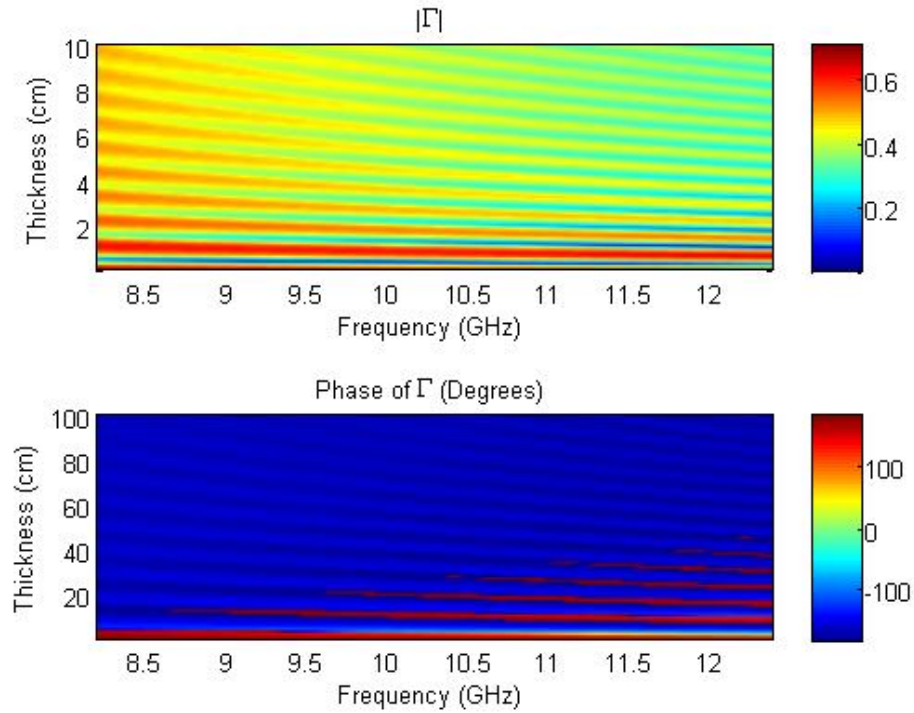


Figure 4.45. The frequency response of the structure as a function of first layer thickness.

The DFT for the FMCW signal is shown in Figure 4.46

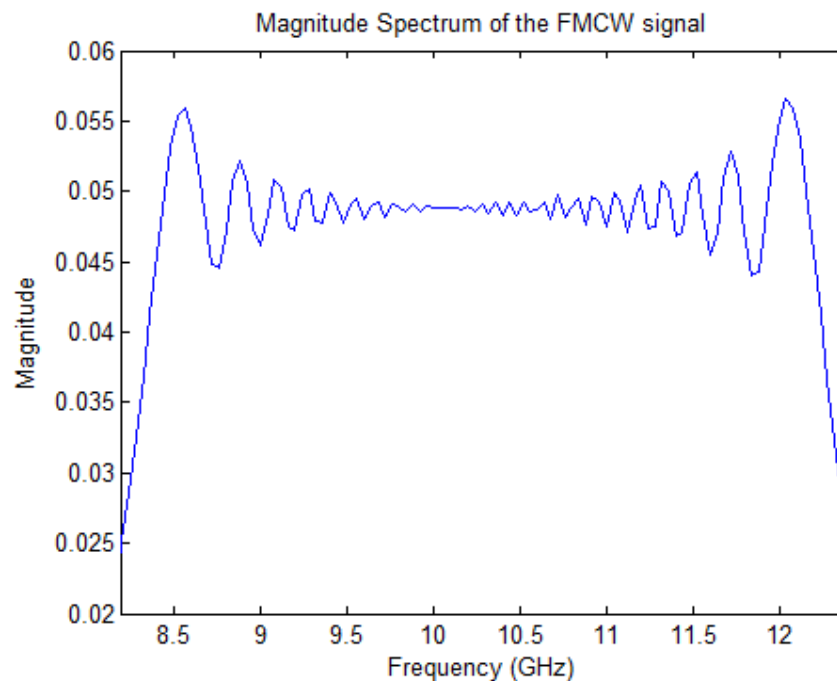


Figure 4.46. The magnitude spectrum of the FMCW signal.

By applying Equation (4.4) and taking the inverse DFT i.e. the IFFT function in Matlab, we obtain the simulated reflected FMCW signal from the structure using its frequency response Figure 4.47.

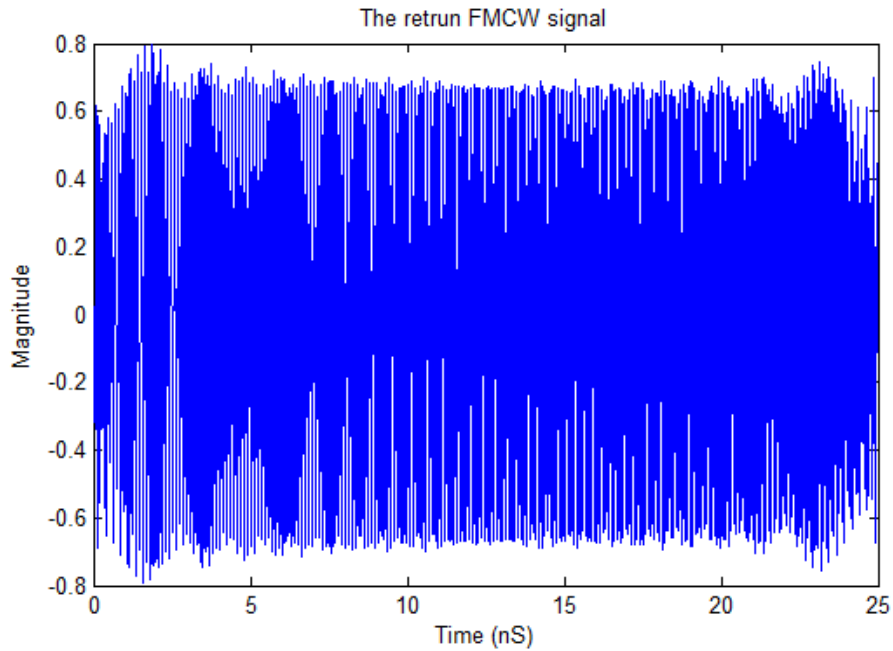


Figure 4.47. The return FMCW signal obtained using the structure's frequency response.

A delay was then introduced to the return signal to simulate the actual delay which happens when the signal propagate back to the mixing stage. In the mixing stage the return signal was mixed with the reference and the resulting beat frequency spectrum is shown in Figure 4.48 for the two extreme cases previously mentioned.

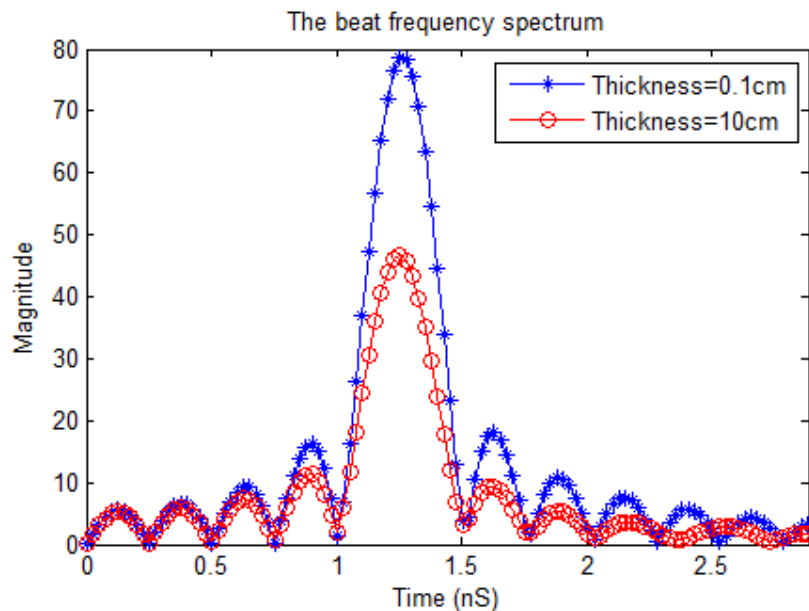


Figure 4.48. The beat frequency spectrum for two thicknesses 0.1cm and 10cm using rectangular window.

Figure 4.48 does not show any clear distinction between the two beat frequencies because of the high frequency leakage from the dominant frequency. To

reduce frequency leakage, the window type will be changed from a rectangular window to a smoother window such as Hamming, Blackman, Hanning, Kaiser etc. Hamming window was chosen since it has low frequency leakage. The latter is on the expense of wider main lobe –around twice as wide as a rectangular window.

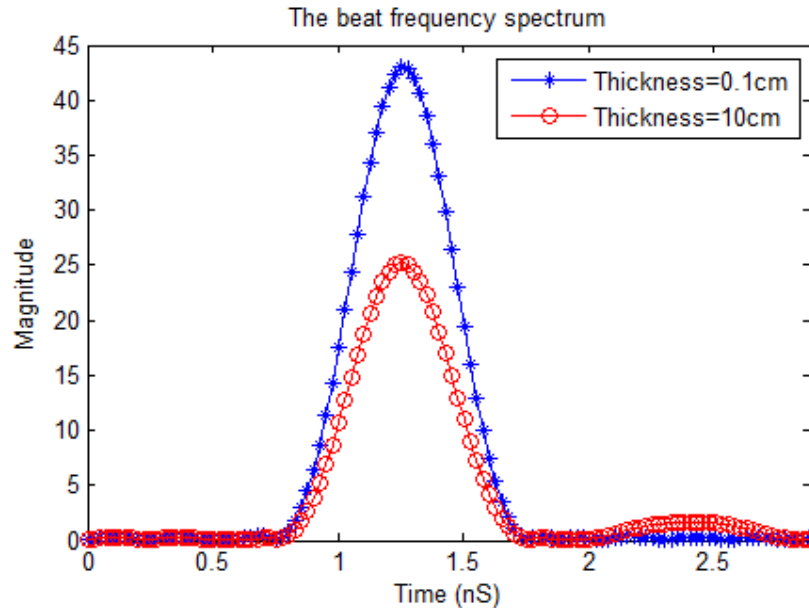


Figure 4.49. The beat frequency spectrum for two thicknesses 0.1cm and 10cm using hamming window in linear scale.

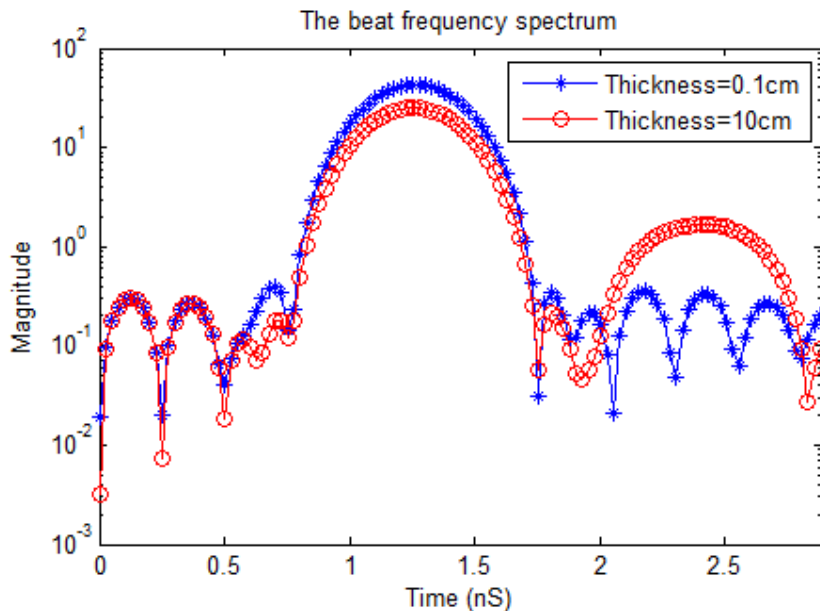


Figure 4.50. The beat frequency spectrum for two thicknesses 0.1cm and 10cm using hamming window in log scale.

From Figure 4.49 and Figure 4.50 we can observe that when the thickness of the layer was small the two beat frequencies were perceived as one from the

magnitude spectrum. As the thickness increase the second beat frequency started to move further to the right. The cause behind this shift is the increase in the time delay of the second reflection from the second interface i.e. between the first and second layers, while the time delay of the reflection from the first interface i.e. between the waveguide and the first layer, did not change. To show the change in the beat frequency spectrum, the thickness of the first layer was swept in steps of 0.1 cm and the beat frequency for each case was saved in a two dimensional array. The effect of the change in thickness on the beat frequency spectrum is shown in Figure 4.51 and Figure 4.52.

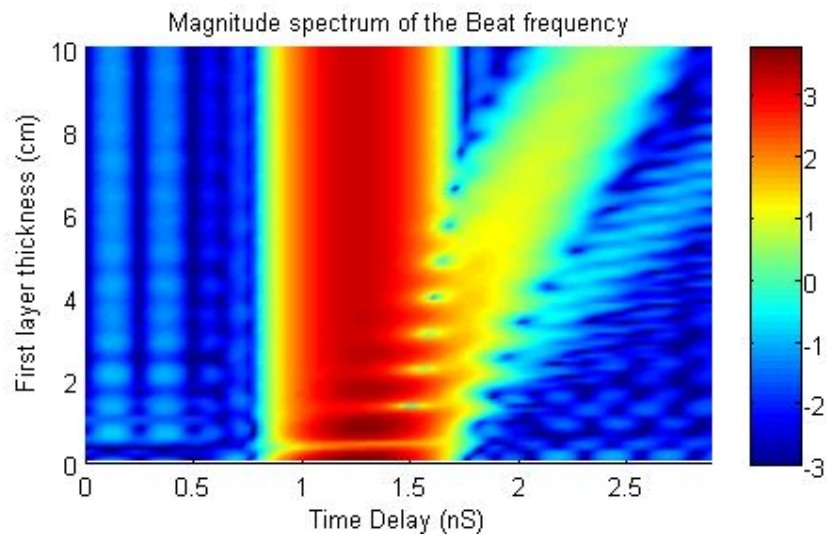


Figure 4.51. The change in the Beat frequency magnitude spectrum in log scale as a function of varying thickness.

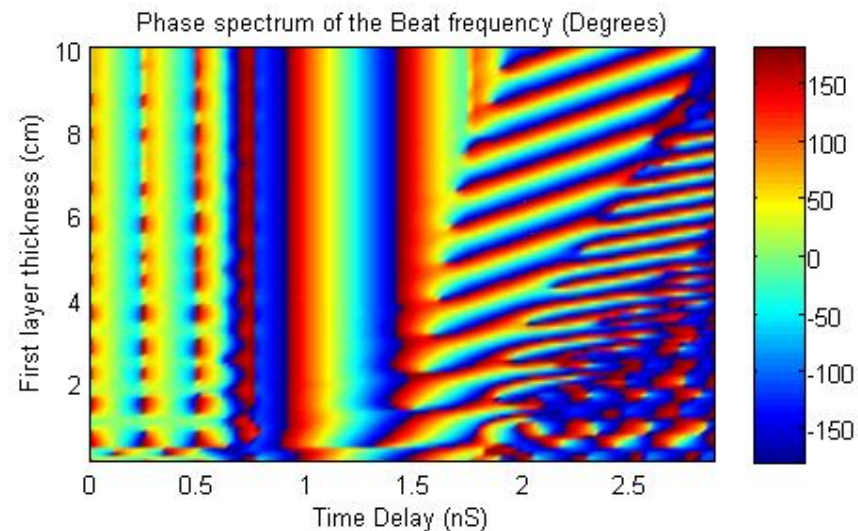


Figure 4.52. The change in the Beat frequency phase spectrum as a function of varying thickness.

4.4 Evaluation Time

The time which Matlab requires to evaluate Equation (3.12) varies with the number of layers. The number of points used to evaluate the inverse Fourier Transform was determined after trying different values. The finalized settings required the evaluation of a mesh with the size of 600x1600 elements. The algorithm will be used to evaluate the complex reflection coefficient on an Intel® Core™2 Quad Processor Q9550. The number of layers will be varied in each simulation and the average time to compute a single reflection coefficient will be calculated. For the cases of single layer up to 8 layers 100 computations were made while for 9 and 10 layers only 30 computations were made. The total time was then divided by the total number of computations hence obtaining the average time for single computation. This way we guarantee that the time of initializing constants and other parameters is not counted as part of the computation time since they are initialized once for all values. Table 4.2 shows the details of the computation time for each case.

Table 4.2. Computation Speed as a function of number of layers.

Number of Layers	Number of Computations	Total Time (Seconds)	Average Time (Seconds)
1	100	16.55	0.1655
2	100	39.06	0.3906
3	100	84.90	0.8490
4	100	146.81	1.4681
5	100	288.30	2.8830
6	100	783.00	7.8300
7	100	1243.0	12.430
8	100	2255.7	22.557
9	30	1292.8	43.093
10	30	2655.6	88.821

To observe the relation more clearly Figure 4.53 shows that there is an exponential relationship between the number of layers and computation time. The computation time almost doubles with every added layer.

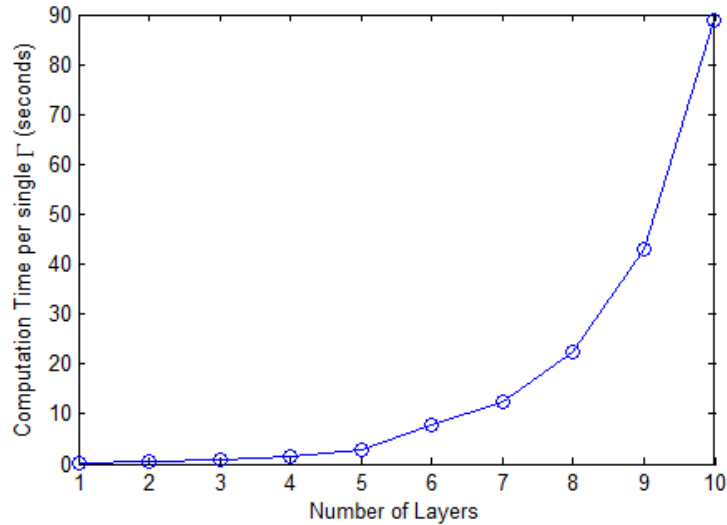


Figure 4.53. Computation time for a single value of Γ as a function of number of layers.

From Table 4.2 and Figure 4.53 it is possible to derive an empirical rule which relates the time required to compute a single value of Γ with the number of layers being evaluated. The computation time (CT) formula is given in Equation (4.7) as a function of number of layers n . The equation was derived by curve fitting using Microsoft Excel and has the unit of seconds per a single evaluation of Γ .

$$CT(n) = 0.0975e^{0.6867n} \quad (4.7)$$

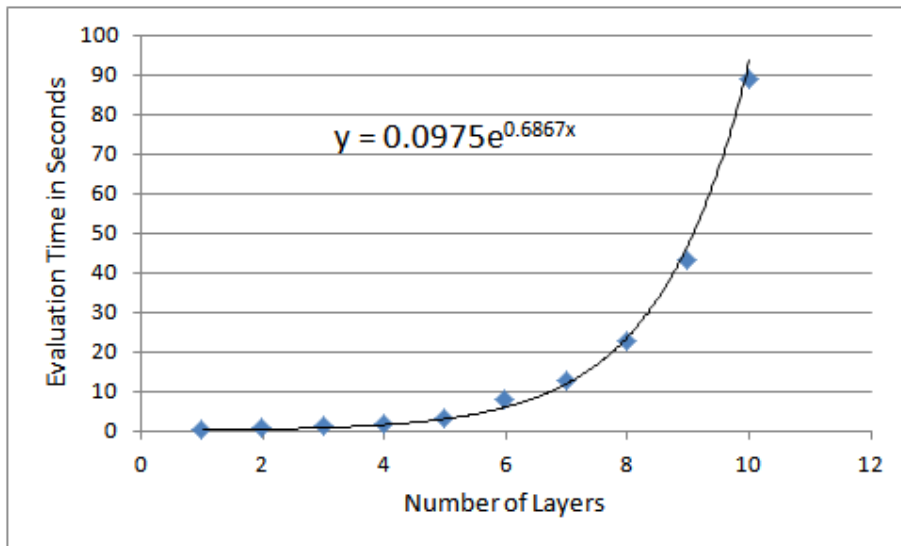


Figure 4.54. The time required to evaluate a single value of Γ as a function of number of layers (n).

CHAPTER 5

CONCLUSIONS AND FUTURE WORK

5.1 Conclusions

This research has established the forward problem of a near-field FMCW radiated by an open-ended RWG. This novel feat might be the base of further research to solve the inverse problem and be able to characterize structures using near-field FMCW. During this research, plenty of observations were made for each step of this work. This chapter is going to summarize the main findings and results of this thesis. The results are numerous and will be listed according to their order in this thesis.

The aperture reflection coefficient was proven to be a variable quantity over the aperture of an open-ended waveguide. The distribution of the reflection coefficient was estimated for a single layer of IHS for many permittivities. It was concluded that the higher the permittivity the more the distribution approached a constant unity value. In other words, none of the distributions were constant in value over the aperture except for the case of total reflection. In light of these results we can conclude that we cannot match the waveguide aperture using a single layer of simple media. Matching occurs when we have no reflections at the aperture and all the power is transferred from the waveguide to the outer medium. Although this conclusion has no direct impact on the main idea of the thesis, it provides an interesting insight on the nature of open-ended waveguide radiation.

The derived expression for the effective value of the reflection coefficient is given by Equation (3.12). The expression was derived based on an assumption that the structure does not affect the polarity of the electromagnetic field within the waveguide. It is claimed in this thesis that the reflected field inside the waveguide is the result of non-uniform reflection coefficient at the interface which in turn is what causes higher order modes to appear. The appearance of higher order modes was also

discussed by many other researchers. Since the operating frequency is within the dominant mode only then these higher order modes will become evanescent modes. Leaving only the dominant mode able to return to the beginning of the waveguide and then back to the receiver. This is why only the reflected dominant mode was of interest when computing the effective reflection coefficient. Using the orthogonality principle the reflected dominant mode was isolated and computed in both magnitude and phase. The computed reflection coefficient was compared to the findings of other researchers who used other techniques both theoretical and practical. The difference in the magnitude of the reflection coefficient did not exceed 0.06 for the worst case scenario and was well within 0.03 for other cases. Personally, I believe that multimode solutions are more exact. However, the issue with multimode derivations is that it is derived for a single layer of an IHS of a dielectric. It is also more complex than the approach used in this thesis. On the other hand, the derivations done in this thesis apply to multilayered structures which is the main concern of this research.

In an attempt to improve the speed of the algorithm an additional assumption was made. The reflection coefficient was approximated to be a constant which resulted in an extremely efficient formula which required a single point substitution in the frequency domain Equation (3.14). Tests were done to measure the difference between Equations (3.12) and (3.14). Based on the simulation, the alternative formula given by Equation (3.14) introduced a maximum difference of 0.02 in magnitude when simulated for a single layer with a relative permittivity higher than a nominal value of 3. In addition, when simulated for two layers the results were not satisfactory. It was concluded that Equation (3.14) cannot replace Equation (3.12) and the latter is the one that provides realistic results. This conclusion was drawn after noticing that the alternative formula evaluated plane wave scenario where the waves do not decay as a function of distance. Therefore, the efficient formula is rejected as an alternative and should not be used as a part of the forward problem of near-field FMCW.

After confirming that Equation (3.12) is to be used, the analogy between the structure and an LTI system was established. This new perspective allowed us to define a structure by its frequency response. The latter was used to compute the reflection for any applied input signal in general and for an FMCW signal in specific. The frequency response of multiple layers was simulated for two and six layers. The

effect of changing a single parameter on the frequency response was shown on a surface plot. It is possible to practically measure the frequency response of a structure using network vector analyzer. Therefore, it is possible by iterative means to estimate the structures parameters from its frequency response. As a secondary observation it is possible to establish a relatively good matching to the open-ended RWG's aperture using two layered structure. This observation is most clear in Figure 4.46 where the $|\Gamma|$ reaches a very low magnitude.

FMCW radar simulations seem to act well according to theory. The multiple reflections were decomposed into Beat frequencies by mixing the return signal with the reference signal. The latter is an exact version of the input but usually scaled and shifted in time. The return FMCW was obtained using the structure's frequency response which in turn was computed using Equation (3.12). The results showed that decomposing two overlapping beat frequencies using just the magnitude spectrum is difficult to achieve when the time delay between them is too small. This case is shown in Figure 4.49 for the case of 0.1 cm thickness. However, the phase spectrum was rich with information which could be used along with the magnitude spectrum to resolve the individual components Figure 4.51 and Figure 4.52. Establishing solid rules on solving the inverse problem is not possible with the current observations and will be left as future work.

The time required to evaluate a single value of Γ is related to the number of layers of the structure being evaluated. It was shown that the time is related by an exponential relationship to the number of layers. The time almost doubles with the addition of another layer to the structure model. The computation time has a direct impact on the speed of exhaustive search techniques when solving the inverse problem. It is apparent that such techniques will lose their meaning if the search is too slow.

5.2 Recommendations for Future Work

One of the most significant improvements that can be achieved is the derivation of a multimode analytical solution that works for multiple layers. The resulting algorithm is expected to be computationally intensive and slower than the expressions derived in this thesis. If the accuracy advantage of such solution outweighs the penalty on speed then it could be a better choice over Equation (3.12).

Optimizing the algorithm used to evaluate Equation (3.12) is also recommended to improve the computation time especially when using exhaustive search techniques to solve the inverse problem.

The FMCW simulation showed that using only the magnitude spectrum of the Beat frequency provides poor resolution over the X-band frequency range. Future work can involve the phase spectrum as a complementary set of information to the magnitude spectrum. There is high potential in being able to enhance the spatial resolution by decomposing partially overlapping beat frequency components. One way is already mentioned in the literature review is known as multiple signal characterization (MUSIC) algorithm [11]. This technique or any equivalent method can be used to enhance the resolution of the beat frequency spectrum. Doing so will provide valuable information about the expected number of layers in the structure. This in turn will help establish the dimensionality of the inverse problem. A rough estimate of layer's permittivities can be made if the signal's decay rate is known as a function of distance. Moreover, the amount of the reflected signal at that interface could be related to the amplitude of the impulse response at that interface Figure 4.42.

System identification techniques could work well as the solution for the inverse problem. System Identification is defined as mathematical tools and algorithms to describe and predict dynamic behavior of a system or process from measured data [16]. Simply put, the received signal from the structure could be applied to a nonlinear function mapper such as a neural network that has been trained using simulated or practical results.

REFERENCE LIST

- [1] N. Qaddoumi, "Microwave Detection and Characterization of Subsurface Defect Properties in Composites Using Open Ended Rectangular Waveguide," Ph.D. Dissertation, Colorado State University, 1998.
- [2] N. Gopalsami, S. Bakhtiari, S. Dieckman, P. Raptis and J. Lepper, "Millimeter-Wave Imaging for Nondestructive Evaluation of Materials," *Materials Evaluation*, vol. 52, no. 3, March 1994.
- [3] M.I. Skolnik, *Introduction to Radar Systems*, 3rd ed. New York: McGraw-Hill, 2001.
- [4] S. Bakhtiari, "Open-Ended sensors for Microwave Nondestructive Evaluation of Layered Composite Media," Ph.D. Dissertation, Colorado State University, 1992.
- [5] M. Abu Khousa, N. Qaddoumi and W. Saleh, "On the Near-Field Radiation Intensity in Multilayer Dielectric Structures Irradiated by an Open-Ended Rectangular Waveguide," Submitted to *IEEE Transactions on Microwave Theory and Techniques*, October 2004.
- [6] A. Bin Sediq and N. Qaddoumi, "Near-Field Microwave Image Formation of Defective Composites Utilizing Open-Ended Waveguides with Arbitrary Cross Section," *Composite Structure*, vol. 71, pp. 343-348, 2005.
- [7] W. Saleh, N. Qaddoumi and M. Abou-Khousa, "Preliminary Investigation Of Near-Field Nondestructive Testing Of Carbon-Loaded Composites Using Loaded Open-Ended Waveguides" *Composite Structures*, vol. 62, pp. 403-407, 2003.
- [8] N. Qaddoumi, R. Zoughi and G.W. Carriveau, "Microwave Detection and Depth Determination of Disbonds in Low-Permittivity and Low-Loss Thick Sandwich Composites," *Research in Nondestructive Evaluation*, vol. 8, no. 1, 1996.
- [9] R. Compton, "The Admittance of Aperture Antennas Radiating into Lossy Media," Ph.D. Dissertation, Ohio State University, 1964.
- [10] "All-weather Volcano Topography Imaging Sensor (AVTIS): Radar," University of St Andrews, 2009 [Online]. Available: <http://www.st->

andrews.ac.uk/~mmwave/mmwave/avtis_theory2.shtml. [Accessed: Mar. 12, 2009].

- [11] M. Abou-Khousa and R. Zoughi, "Microwave quantitative NDE technique for dielectric slab thickness estimation using the MUSIC algorithm," *Review of Progress in Quantitative Nondestr. Eval., AIP Conference Proceedings*, 2007, vol. 26A, pp. 440-447.
- [12] D. M. Pozar, *Microwave Engineering*, 3rd ed. New York: John Wiley & Sons, 2005.
- [13] K. Bois, A. Benally and R. Zoughi, "Microwave near-field reflection property analysis of concrete for material content determination," *IEEE Transaction. Instrum. Meas.*, vol. 49, pp. 49–55, Feb. 2000.
- [14] K. Yoshitomi and H. R. Sharobim, "Radiation from a rectangular waveguide with a lossy flange," *IEEE Transaction Antennas Propagat.*, vol. 42, pp. 1398–1403, Oct. 1994.
- [15] D. G. Bodnar and D. T. Paris, "New variational principle in electromagnetics," *IEEE Transaction Antennas Propagat.*, vol. AP-18, pp. 216–223, Mar, 1970.
- [16] P. R. Water, J. H. Kerckhoffs and D. V. Welden, "GMDH-based dependency modeling in the identification of dynamic systems," *European Simulation Multiconference on Simulation and Modelling Enablers For A Better Quality of Life Proceedings*, May 2000, pp. 211–218.

Appendix A

Matlab Codes

Functions:

```
% The variables above were declared Global so we can call them here
% Function g1 will be used as the primary function to call Mi. While
% Ci stays Independent for independent calling.
```

```
function Ci=C(i)          % A Function of Kx,Ky dependant on the i-th
layer only.
global K Kx
Ci=(K(:,i).^2-Kx.^2)./gam(i);
end
```

```
% Function g1 will be used as the primary function to call Mi.
% While Ci stays Independent for independent calling.
```

```
function gi=g(i)
global d N
if i>0 && i<(N)
    Mi=M(i);
    Ci=C(i);
    Cil=C(i+1);
    gi=exp(-2.*gam(i).*d(i)).*(Ci-Cil.*Mi)./(Ci+Cil.*Mi);
else
    gi=0;
end
end
```

```
function Mi=M(i)
global d N
if i>0 && i<(N-1)
    gami=gam(i+1);
    Mi=(1-
g(i+1).*exp(2.*gami.*d(i)))./(1+g(i+1).*exp(2.*gami.*d(i)));
    Ind=abs(exp(2.*gami))==inf;%This part of the code tries to
substitute the limit in case of infxzero
    Mi(Ind)=1;
else
    Mi=1;
end
end
```

```
function gami=gam(i)      % Defines the Variable Little Gamma (3-25)
global K Kx Ky
gami=sqrt(Kx.^2+Ky.^2-K(:,i).^2);
end
```

```
function T=iseven(U)
T=~(ceil(U/2)-U/2);
```

```

%% Code Starts here
clear all
clc
i=[];
FIG=2;
%% General N-Layer Composite Terminated with IHS numeric solution
global Th d Eps N w K f a b Kc Kx Ky
Ref=[]; % The Reflection Coefficient i.e. Gamma.
specs=2;
Plot=1;
if specs==1
    f=25.5e9; % Frequency.
    a=0.0107; % Width of the waveguide along X.
    b=0.0043; % Height of the waveguide along Y.
elseif specs==2
    TSP=5e-2; %Time shift portion of the Sweep time in
percentage
    FilTyp=1; %Set to 1 for IIR set to 2 for FIR set to else
    Non causal brickwall filter % Main FMCW signal
    radar=[5000 (5e-13) 8.2e9 12.4e9 5e-3];
    n=radar(1); Ts=radar(2); fo=radar(3); f1=radar(4);
    TD=radar(5); Ts=(5e-12); fs=1/Ts;
    F=-fs/2:fs/n:fs/2-fs/n;
    Ind1=find(F>=(fo*0.99) & F<=(f1*1.005));
    Ind2=find(F==-F(Ind1(end)));
    f=F(Ind1(1):Ind1(end)); % Frequency.
    Co=3e8; Tsw=Ts*n; t= 0:Ts:(n-1)*Ts; Bw=f1-fo;
    kf=Bw*2*pi; fm=t.^2/2; FMCW=sin(fo*2*pi*t+kf/Tsw*fm);
    a=0.02286; % Width of the waveguide along X.
    b=0.01016; % Height of the waveguide along Y.
    FMCW_f=fftshift(fft(FMCW));
end
% Constants and Axes
Lx=600; Ly=1600; Sx=30; Sy=60;
StepX=Sx*a/Lx; StepY=Sy*b/Ly;
M=0:1:Lx-1; N=0:1:Ly-1;
x1=M*StepX; y1=N*StepY;

x=x1'*ones(1,length(y1)); x=x';
y=ones(length(x1),1)*y1; y=y';

dx=2*pi/Sx/a;
dy=2*pi/Sy/b;
Kx1=-Lx/2*dx:dx:Lx/2*dx-dx;
Ky1=-Ly/2*dy:dy:Ly/2*dy-dy;
Kx=ones(length(Ky1),1)*Kx1;
Ky=Ky1'*ones(1,length(Kx1));
sinTE10=sin(pi/a*x(1:Ly/Sy+1,1:Lx/Sx+1));
sinTE10(Ly,Lx)=0;
figure(1)
surf(x,y,sinTE10)
shading interp
% Taking the Fourier Trnsanform using 2-D FFT
sinTE10FFT=fftshift(fft2(sinTE10))./(dkx*dky*Lx*Ly);
I=sinTE10FFT;
Kc=pi/a; % Wave number for dominant mode.
count=1;
for Delta=1:count
    Delta
    for Frq=1:length(f)
        Eps=[3 50];
    end
end

```

```

Th=[0.001*Delta];
d=cumsum(Th);           % Depth of interfaces in meters.
N=length(Eps);         % Number of layers
w=2.*pi.*f(Frq);       % Omega
Ko=w./3e8;             % Wave Number inside the waveguide
K=Ko.*sqrt(Eps);       % Wave Number inside the layers
mue=4e-7*pi;
eps=1e-9/36/pi;
Yo=sqrt(Ko.^2-Kc.^2)./(w.*mue);
%% Fourier Transform FT of The Reflection Coefficient
C1=C(1);
g1=g(1);
RefK_noI=(Yo-(C1.*(g1-1)./(1+g1)/(1j*w*mue)))/(Yo+(C1.*(g1-
1)./(1+g1)/(1j*w*mue)));
RefK=RefK_noI.*I;
%% Inverse FT
Temp1=(fftshift(RefK));
if Frq==1
    Xcount=size(Temp1,1);
    Ycount=size(Temp1,2);
    StepX=pi/Kx1(end);
    StepY=pi/Ky1(end);
    Xis=0:StepX:StepX*(Xcount-1);
    Yis=0:StepY:StepY*(Ycount-1);
    x=x(1,1:Lx/Sx+1);
    y=0:StepY:b;
    x1=x'*ones(1,length(y));
    x1=x1';
    y1=ones(length(x),1)*y;
    y1=y1';
    sin_xy=sin(pi/a*x1);
    CON=sum(sum(sin_xy.^2));
end
Temp2=ifft2(Temp1)*Xcount*Ycount*dkx*dky;
Ref=Temp2;
Ref=Ref(1:length(y),1:length(x));
Ref_Norm(Frq)=sum(sum(Ref.*sin_xy))/(CON);
end
%%
TF=[zeros(1,Ind2-1) conj(Ref_Norm(end:-1:1))];
TF(length(F))=0;
TF(Ind1(1):Ind1(end))=Ref_Norm.';
TF_save(Delta,:)=TF;
figure(4)
subplot(2,1,1)
plot(F/1e9,abs(TF),'-')
xlim([8.2 12.4])
ylabel('| \Gamma |')
xlabel('Frequency (GHz)')
grid on
subplot(2,1,2)
plot(F/1e9,angle(TF)*180/pi,'-')
xlim([8.2 12.4])
ylabel('Phase of \Gamma (Degrees)')
xlabel('Frequency (GHz)')
grid on
% figure(5)
% plot(t,(ifft(fftshift(TF))), 'k')
% title('Numerically Approximated Impulse response')
% xlabel('Time(S)')
% ylabel('value of reflection unit-less')

```

```

%%
RFMCW=ifft(fftshift(FMCW_f.*TF));
RFMCW_Save(Delta,:)=RFMCW;
% Mixing with reference Signal and Filtering
TSF=round(n*TSP); %Time shift factor of n
MIX_Raw=FMCW(TSF+1:end).*(RFMCW(1:end-TSF));
%MIX_Raw=sqrt(RFMCW(TSF+1:end).*(RFMCW(1:end-TSF))/2);
%Mixing the signal with itself
ARange=[0 cumsum(Th.*real(sqrt(Eps(1:end-1))))]+Co/2*Ts*TSF;
Mix_no_shift=FMCW.*RFMCW;
if FilTyp==1
    [G H]=butter(4,0.01,'low'); % finding the filters
coefficients
    MIX=filter(G,H,Mix_no_shift);
elseif FilTyp==2
    G=fir1(100,0.005);
    H=1;
    MIX=filter(G,H,Mix_no_shift);
else
    MIX_f=fft(Mix_no_shift);
    Dis_Sample=fs/n*Tsw/Bw*Co/2; %Displacement spacing
in the frequency domain
    Nfilter=ceil(4*ARange(end)/Dis_Sample); %Calculating
required number of samples to be reserved
    MIX_f(Nfilter+1:end-Nfilter+1)=0;
    MIX=ifft(MIX_f);
end
% Obtaining beat Frequencies
OS=10; %over sampling constant
MIX_Res=resample(MIX_Raw,1,OS);
MIX_Save(Delta,:)=MIX_Res;
end
%%
Window=hamming(length(MIX_Res))*ones(1,count);
%Window=1;
Beat=(fft(MIX_Save'.*Window,length(MIX_Res)*OS));
n2=length(Beat);
fs2=fs/OS;
F_b=0:fs2/n2:fs2-fs2/n2;
Time_Delay=F_b*Tsw/Bw;
figure(4)
ARange=[0 cumsum(Th.*real(sqrt(Eps(1:end-1))))]+Co/2*Ts*TSF;
plot(Time_Delay*1e9,abs(Beat(:,1)),'-
*',Time_Delay*1e9,abs(Beat(:,100)),'-or')
semilogy(Time_Delay*1e9,abs(Beat(:,1)),'-
*',Time_Delay*1e9,abs(Beat(:,100)),'-or')
xlim([0 ARange(end)*1.2/Co*2*1e9])
title('The beat frequency spectrum')
ylabel('Magnitude')
xlabel('Time (nS)')
legend('Thickness=0.1cm','Thickness=10cm')
%%
figure(7)
LOG=1;
set(gcf,'Color',[1,1,1])
% while 1
legend('Beat Frequency Spectrum','Exact Delay Introduced by The
Interface','Location','SouthEast')
CC=1;
while CC<=100
    for wait=1:2000

```

```

        1
    end
    ITime=[0 cumsum(0.001*floor(CC).*real(sqrt(Eps(1:end-
1))))]*2/Co+Ts*TSF;
    LINE=ones(length(ITime),1)*[0.0005,100];
    Impulse=ITime'*ones(1,2);
    if LOG==1

semilogy(Time_Delay*1e9,abs(Beat(:,floor(CC))),Impulse'*1e9,LINE','--
r')
    else
    plot(Time_Delay*1e9,abs(Beat(:,floor(CC))),Impulse'*1e9,LINE','--
r')
    end
    xlim([0 ARange(end)*1.2/Co*2*1e9])
    ylim([1e-2 45])
    title(['The Beat frequency spectrum when Thickness='
num2str(0.1*floor(CC)) ' cm'])
    ylabel('Magnitude')
    xlabel('Time (nS)')
    shg
    CC=CC+1;
end
% end
%%
figure(8)
set(gcf,'Color',[1,1,1])
% while 1
legend('Beat Frequency Spectrum','Exact Delay Introduced by The
Interface','Location','SouthEast')
CC=1;
while CC<=100
    for wait=1:1000
        1
        end
        ITime=[0 cumsum(0.001*floor(CC).*real(sqrt(Eps(1:end-
1))))]*2/Co+Ts*TSF;
        LINE=ones(length(ITime),1)*[-200,200];
        Impulse=ITime'*ones(1,2);

plot(Time_Delay*1e9,180/pi*angle(Beat(:,floor(CC))),Impulse'*1e9,LINE
','--r')
    xlim([0 ARange(end)*1.2/Co*2*1e9])
    ylim([-180 180])
    title(['The Beat frequency phase spectrum when Thickness='
num2str(0.001*floor(CC)) ' cm'])
    ylabel('Phase in Degrees')
    xlabel('Time (nS)')
    shg
    CC=CC+1;
end
% end
%%
figure(8)
WTW=1:100;
Var_beat=log(abs(Beat(:,[WTW]).'));
Var_beat(Var_beat<-3)=-3; % Setting Lowest dB value to -3 for clear
color scale
surf(Time_Delay*1e9,WTW*0.1,Var_beat)
xlim([0 ARange(end)*1.2/Co*2*1e9])
xlabel('Time Delay (nS)')

```

```

ylabel('First layer thickness (cm)')
title('Magnitude spectrum of the Beat frequency')
shading interp
colorbar
shg
figure(9)
WTW=1:100;
pcolor(Time_Delay*1e9,WTW*0.1,180/pi*(angle(Beat(:, [WTW]).')))
xlim([0 ARange(end)*1.2/Co*2*1e9])
xlabel('Time Delay (nS)')
ylabel('First layer thickness (cm)')
title('Phase spectrum of the Beat frequency (Degrees)')
shading interp
colorbar
shg
figure(10)
WTW=1:100;
pcolor(Time_Delay*1e9,WTW*0.1,180/pi*unwrap(angle(Beat(:, [WTW]).'))) %
plot(Range,abs(Fbeat),'r',ARange,zeros(1,length(ARange)),'ob')
xlim([0 ARange(end)*1.2/Co*2*1e9])
xlabel('Time Delay (nS)')
ylabel('First layer thickness (cm)')
title('(Unwrapped)Phase spectrum of the Beat frequency')
shading interp
shg
colorbar
%%
CD=1:2;
figure(11)
subplot(2,1,1)
plot(F/1e9,abs(TF_save(CD,:)))
xlim([8.2 12.4])
ylabel('| \Gamma |')
xlabel('Frequency (GHz)')
grid on
subplot(2,1,2)
plot(F/1e9,180/pi*angle(TF_save(CD,:)))
xlim([8.2 12.4])
ylabel('Phase of \Gamma (Degrees)');xlabel('Frequency (GHz)')
grid on;shg
CD=1:100;
figure(12)
subplot(2,1,1)
pcolor(F/1e9,CD*0.1,abs(TF_save(CD,:)));xlim([8.2 12.4]);
title('| \Gamma |');ylabel('Thickness (cm)');xlabel('Frequency (GHz)')
shading interp;colorbar;subplot(2,1,2)
pcolor(F/1e9,CD,180/pi*(angle(TF_save(CD,:)))
xlim([8.2 12.4]);title('Phase of \Gamma (Degrees)')
ylabel('Thickness (cm)');xlabel('Frequency (GHz)')
grid on;shading interp;colorbar;shg
figure(2);plot(F/1e9,abs(FMCW_f)/length(FMCW))
xlim([8.2 12.4]);title('Magnitude Spectrum of the FMCW signal')
ylabel('Magnitude');xlabel('Frequency (GHz)');figure(3)
plot(t*1e9,RFMCW_Save(1,:),'b');title('The retrun FMCW signal')
ylabel('Magnitude');xlabel('Time (nS)')

```

VITA

Ayman Jalal Jundi was born on Oct 02, 1985, in Hims, Syrian Arab Republic. He was educated in government and private schools and graduated from Al-Khaleej Al-Arabi School in 2003. He then got enrolled in the American University of Sharjah, U.A.E from which he graduated *summa cum laude* in 2008. His degree was Bachelor of Science in Electrical Engineering. Mr. Jundi received a graduate teaching assistantship to join the master's program in Electrical Engineering at the American University of Sharjah. He was awarded the Master of Science degree in Electrical Engineering in 2010.